Mid-latitude Extremes in Ensemble Simulations from 1500 to 2100

Master Thesis

Faculty of Science
University of Berne

presented by

Claudia Stocker

2011

Supervisor:
PD Dr. Christoph C. Raible

Co-Supervisor:
Prof. Dr. Thomas F. Stocker

Climate and Environmental Physics
Physics Institute of the University of Berne
Oeschger Centre for Climate Change Research, University of Bern

Contents

Abstract

In the framework of the current thesis, temperature and precipitation extreme values are examined on the basis of the Community Climate System model version 3 (CCSM3) from the National Centre for Atmospheric Research (NCAR). An ensemble of four transient simulations from 1500 to 2100 is used for the analysis of extreme events in the mid-latitudes. In the past years (1500-2000), the model experiences natural forcing and anthropogenic forcing on the basis of reconstructions, for the last 100 years the SRES scenario A2 is applied. Three 30-year periods (1661-1690, 1851-1880 and 2071-2100) with reference to 1961-1990 are examined on extreme values using the Generalized Extreme Value theory (GEV). Three parameters describing the extreme value distribution (location, scale and shape parameter), as well as the return values of temperature/precipitation extremes on different return levels are compared among the different periods of time and different regions across Europe (mainly the Mediterranean, Central and Northern Europe). Concerning temperature extremes, the lowest return values are found in the Maunder Minimum, but also pre-industrial extreme temperatures are below the level of the reference period. For the future, temperature return values show an overall increase. The return values of precipitation show a less distinct pattern. In a second step, temperature and precipitation anomalies on longer time scales - namely cold/warm spells and droughts - are analyzed. In the Maunder Minimum and pre-industrial period cold spells are more frequent and of longer duration as warm spells, in particular in Central Europe. For future projections, warm spells experience a large rise in number and duration, cold spells tend to almost vanish. Droughts and wetnesses are analyzed on the basis of the Standardized Precipitation Index (SPI) on different time scales (12-months, 24-months, 48-months and 72-months). The development over time of the 50 year return level depicts severe droughts in the early (Central Europe), middle (Mediterranean) and late (Northern Europe) Maunder Minimum. For future projections, droughts nearly disappear in Central and Northern Europe, but they increase in the Mediterranean region.

Chapter 1

Introduction

1.1 Background and Motivation

> *"Warming of the climate system is unequivocal, as is now evident from observations of increases in global average air and ocean temperatures, widespread melting of snow and ice, and rising global average sea level" IPCC [2007].*

According to the Intergovernmental Panel on Climate Change (IPCC) there is no doubt that the mean state of the current climate changes. Temperature increased 0.76°C over the last 100 years (1906-2005), precipitation increased generally over land north of 30°N between 1900 to 2005, the tropics and subtropics undergo a drying since 1970 and also westerly winds grew stronger in the mid-latitudes of both hemispheres [*IPCC*, 2007].

However not only changes in the mean climate of the Earth system were observed, also changes in extreme weather and climate events could play an important role [*IPCC SREX*, 2011]. In the past years, weather hazards have caused a large number of losses of human life as well as economic losses [*Easterling et al.*, 2000]. In August 2005, Hurricane Katrina caused more than 900 deaths and produced total damages of roughly $156 Billions [*Brunkard et al.*, 2008; *Burton and Hicks*, 2005]. The flooding event of 2011 in Brisbane affected 200,000 people (*BBC News*, source: http://www.bbc.co.uk/news/world-asia-pacific-12158608 [30.06.2011]). The heat wave of the summer 2003 caused 40,000 heat-related deaths across Europe [*García-Herrera et al.*, 2010].

Easterling et al. [2000] investigate changes in trends and variability in extreme temperature, precipitation and wind. As a first guess, these changes in extreme events could have been induced by natural variability of the climate. *Räisänen* [2000] reports an estimated contribution of 16% of the internal variability to the changes in mean temperature in a model experiment of CO_2 doubling. At the same time, *Hegerl et al.* [2007] and *Del Sole et al.* [2010] state, that the internal variability cannot account for the 0.8°C observed mean warming during the 20^{th} century. This is consistent with the findings of *Stouffer et al.* [1994], *Zorita et al.* [2008] and others. Additional factors might induce changes in mean and extreme climate: variability in natural forcings such as solar variability or volcanic eruptions influence the climate; anthropogenic forcing, which includes, among others, increases in greenhouse gases, such as carbon

dioxide (CO_2), methane (CH_4) and nitrous oxide (N_2O) and aerosol concentration.

In its 4^{th} Assessment Report (AR4) in 2007 the IPCC concluded that a large part of climate change is due to that anthropogenic influence. A weakening of this trend is not very likely. As an example, during the last 800,000 years, CO_2 varied within a range of 172 and 300 ppmv [*Lüthi et al.*, 2008]. The current CO_2 concentration is 393.69 ppm (*Trends in Atmospheric Carbon Dioxide*, source: http://www.esrl.noaa.gov/gmd/ccgg/trends/ [15.07.2011]). The growth rate of carbon dioxide has thus been larger during the last ten years (1995 - 2005), than it has ever been since the beginning of measurements [*IPCC*, 2007]. Based on human activity, industry, energy production (fossil fuel burning) and land-use changes are the primary source of increased atmospheric greenhouse gases.

The world population continuously grows and its demand for land and energy use will not be reduced. An increasing number of people settle in exposed areas and own high-value properties. Even though more resources are spent on protective measures, human society is increasingly vulnerable to climate extremes. There is a need of new adaptation strategies. Therefore researchers and governments investigate in further understanding of extreme events. Special concern is pertained to long-term development of extreme events in high-risk zones [*IPCC*, 2007].

To address the topic of possible future changes, one needs information about past and current conditions. *Hay et al.* [1997] state that the past is the key to the future. Even if there is no geologic analogy to the current climate warming [*Crowley*, 1990], it is important to understand how the past greenhouse, solar and volcanic forcing acted on the climate and the ecosystem [*Hay et al.*, 1997]. As a climate model is able to simulate past, current and future climate conditions, knowledge about the past helps to adjust and improve the model. Future conditions can be simulated more precisely.

The statistical analysis of different scenarios of climate models can give indications of the changes in climate. To estimate the amount of future changes most accurately, it is necessary to compare the analysis of a climate model with other models and observational data. In the framework of this thesis, four runs of the Community Climate System Model of third Generation (CCSM3) of the National Centre of Atmospheric Research (NCAR) in Boulder/USA were analyzed on extreme events. As temperature and precipitation are the most common variables describing extreme weather events [*Nikulin et al.*, 2011], the thesis bases on the statistical analysis of extreme temperature and precipitation indices.

1.2 State of Knowledge

The Expert Team on Climate Change Detection and Indices (ETCCDI) of the World Meteorological Organisation (WMO) defined a sample of 27 core indices describing climate change and extremes. The indices are based on daily temperature and precipitation values [*Peterson*, 2005]. Changes in climatic extremes can be characterized by the use of these different indices. Number of frost days, number of summer days or number of tropical nights are examples of such climate indices (*ETCCDI/CRD Climate Change Indices*, source:

http://cccma.seos.uvic.ca/ETCCDMI/list_27_indices.shtml [13.07.2011]).

Another way of describing the state of the climate system bases on the distribution of the observational data and/or model output. In this case, an extreme event is statistically considered as a value at the upper (or lower) end of the distribution. One commonly uses percentiles that extreme events exceed. If, for example, a temperature event exceeds the 95th percentile, it is part of the 5% of largest observed values; minimal extremes lie below a threshold of 5 percent. *Frich et al.* [2002] examined a global data set to clarify whether frequency and/or severity of climatic extremes changed during the second half of the 20th century. They chose different indicators as well as percentiles of extreme climatic events. Their work is a solid foundation for understanding the global change in extreme values in different variables for the past.

A shift in mean climate can cause a shift in the extreme values as well. If the mean increases, it implies a shift of extremes towards higher values [*Schär et al.*, 2004]. However, not only a changing mean is an important feature. According to *Schär et al.* [2004] a shift in climate mean may imply pronounced changes at the tail of the distribution and in the frequency of extremes. Figure 1.1 represents the results of a regional climate model (RCM) climate change scenario of current (CTRL 1961-1990) and future (SCEN 2071-2100) conditions. *Schär et al.* [2004] report a shift in distribution by 4.6°C towards warmer temperatures in the scenario simulation. More importantly, the scenario simulation exhibits a widening of the distribution as well. An increase in standard deviation is equal to an increase in variability. They therefore state that an increase in variability implies an increase in extremes relative to mean climatic conditions. This fact led to the statement "variability is more important than averages" [*Schär et al.*, 2004].

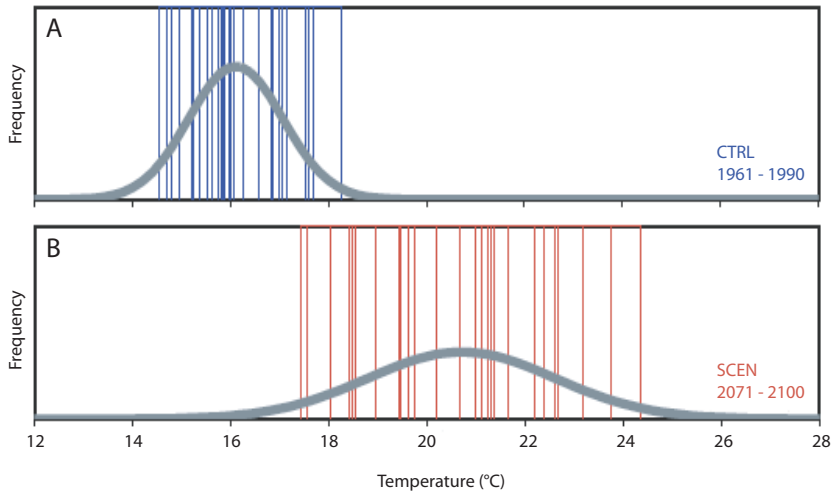

Figure 1.1: Probability density functions of summer temperatures at a grid point in northern Switzerland for current (CTRL 1961-1990) and future (SCEN 2071-2100) conditions [*Schär et al.*, 2004].

Temperature Changes

Of all climate variables examined, temperature shows the most significant changes. The 13 warmest years in 1880-2006 have occurred in or after 1990 [*Zorita et al.*, 2008]. Warming does not occur everywhere and in all seasons, but since 1971 it clearly dominates over land areas [*Jones and Moberg*, 2003]. There has been a significant decrease in the cold nights and a significant increase in warm nights per year [*IPCC*, 2007]. *Scherrer et al.* [2005] estimated a decrease in winter mean temperature of about 10% and an increase in summer mean temperature of 10 to 15%. In addition, a tendency for increasing variability in summer and decreasing variability in winter was observed [*Scherrer et al.*, 2005]. These findings are supported by *Beniston and Diaz* [2004] who found that changes in extremes of daily temperatures in Switzerland were due to changes in both the mean and the variance. Thus, as explained before, even if only a small shift in average temperature has occurred, it leads to more heat extremes and less frost extremes [*Frich et al.*, 2002]. For the Mediterranean area, *Brunet et al.* [2006] showed dramatic increases in warm days since 1973, particularly near the coast. They analyzed a sample of 22 Spanish records for the period of 1894-2003 and found larger reduction in cold days than an increase in hot days. Even though the results of *Brunet et al.* [2006] are concentrated along the coast, the largest changes in warm extremes are generally confined to land areas on the globe, where there is a reduction in soil moisture. *Alexander et al.* [2006] and *Caesar and Lisa* [2006] summarized the results of different regional studies since 1946. Over 74% of the global areas showed a significant decrease in the annual cold night occurrence. A significant increase in annual warm nights occurred in over 73% of the area. The strongest cold day reduction is found in regions that are hit by snow and sea ice retreat due to global warming and the associated albedo feedback [*Nikulin et al.*, 2011; *Bengtsson et al.*, 2004]. This phenomenon is termed polar amplification. Most rapid changes in temperature occurred over the Arctic [*Corell*, 2006] and Antarctic [*Vaughan et al.*, 2003]. Simulated polar warming in the Arctic is even 1.5 to 4.5 times larger than the mean global warming [*Holland and Bitz*, 2003].

Schär et al. [2004] concluded that a change in temperature variability enables the explanation of summer heatwaves (such as the European heatwave 2003), resulting in the strong response of heatwave and drought incidence in the future. Across Europe heatwaves become more severe in the Mediterranean region and in Western Europe [*Meehl and Tebaldi*, 2004]. Heatwaves are expected to experience a location-dependent increase in intensity, duration, as well as frequency, during the 21st century [*Meehl and Tebaldi*, 2004]. Especially, in southernmost Europe changes in heatwave frequency and duration will occur. Further north, the most severe impacts on society arise from long lasting heatwaves (several days), associated with warm nights and high relative humidity [*Fischer and Schär*, 2010].

In the framework of this thesis not only the present and future changes in temperature are of importance. There is a focus on the past behavior as well. *Luterbacher et al.* [2004] reconstructed extremes and trends in temperature since 1500. They state as well that the late 20^{th} and early 21^{th} century is very likely warmer than during the past five hundred years. For the annual mean temperature, *Luterbacher et al.* [2004] estimate a reduction of 0.25°C between 1500 and 1900. Winter temperature were even reduced by 0.5°C. The European winters were thus generally colder than those of the 20^{th} century (except for a short period around 1530

and 1730). The coldest periods are found at the late 16^{th}, the last decades of 17^{th} and at the end of the 19^{th} century. The Maunder Minimum, a period of reduced solar activity, is denoted as the coldest period during 1645 and 1715 [*Eddy*, 1976; *Beer et al.*, 1998]. During this period *Luterbacher et al.* [2004] found the coldest winter in record ($\Delta T = -3.6°\text{C}$) as well. The hottest summer on record they found in 1757 ($\Delta T = +1.6°\text{C}$). Summer temperatures were warmer during the period of mid 18^{th} until the second half of the 19^{th} century. This warm period was followed by a summer cooling trend until the beginning of the 20^{th} century (1902 is the coolest summer). Before the exceptionally strong warming after 1977, *Luterbacher et al.* [2004] describe a summer warming until 1947 with a subsequent cooling until 1977.

Precipitation Changes

As changes in heatwaves are related to soil moisture and evapotranspiration [*Fischer and Schär*, 2010], the question of changes in precipitation arises. The future precipitation distribution shows a less homogeneous picture as for temperature. Generally, the observed increase in atmospheric water vapor implies an increase in precipitation intensity, but a reduction in frequency and duration for an unchanged total evaporation rate from the Earth's surface over land and ocean [*IPCC*, 2007]. Changes in precipitation extremes do not show a distinct geographical pattern. In mid-latitudes and over most land areas heavy precipitation events will increase in the scenario simulations. For most extra tropical regions, instrumental observations and model projections of a greenhouse-enriched atmosphere indicate an increase in intense precipitation [*Groisman et al.*, 2005]. Therein the change in daily extreme precipitation seems to be larger than the annual mean precipitation rate [*Kharin and Zwiers*, 2005]. *Alexander et al.* [2006] gridded precipitation extremes over the globe as well. As mentioned before, *Alexander et al.* [2006] found a less consistent precipitation extreme distribution compared with temperature extremes. Globally averaged, they found an increase in very wet days over land for recent decades. At the same time a precipitation decrease is evident in the tropics and sub-tropics. In conjunction with higher temperatures, the precipitation decrease leads to more intense and longer droughts over wide areas [*IPCC*, 2007].

On the regional level, *Nikulin et al.* [2011] examined, among others, precipitation extremes over Europe. As expected, the spatial pattern shows a complex and spotty structure. For the winter season, the spatial distribution is more consistent than for the summer season. Individual simulations showed an intensification of precipitation extremes across most of Europe. Future changes in summertime extreme precipitation show only small-scale changes with a tendency to an increase in Northern and decrease in Southern Europe [*Nikulin et al.*, 2011]. Similar results are achieved by *Frei et al.* [2006]. North of about 45°N, precipitation extremes tend to increase during winter, while model differences leading to scenario uncertainties are found in summer.

Regarding past precipitation, *Pauling et al.* [2006] reconstructed the last five hundred years. For winter and spring months they estimated a rather wet 18^{th} century with an increased interdecadal variability. Precipitation extremes are found either in the second half of the 17^{th} century (spring months) or the first half of the 18^{th} century (winter months). Until

the 19^{th} century a slow decrease in precipitation amount is detected. *Pauling et al.* [2006] also investigated in summer and autumn months. Especially during summer, high decadal variability is found until 1760, on a level of large precipitation amounts. For both summer and autumn month, the most extreme precipitation events (dry and wet) are found between 1660 and 1670, which represents a period within the Maunder Minimum.

1.3 Aims and Objectives

The aim of this thesis is to investigate the potential changes of extreme events in three different regions across Europe during the past 500 and the coming 100 years for which the A2 climate scenario is used. To address this question, four transient simulations of the CCSM3 model are analyzed. All transient simulations are calculated using the same forcings, but differ in their initial conditions.

Three European regions are chosen according to their geographical position and climatological characteristics: an area in the Mediterranean, one in Central Europe and one in Northern Europe. The detection of shifts in so-called return levels of extreme events and in extreme climate indices for different time periods (1661-1690, 1851-1880, 1961-1990 and 2071-2100) is the main objective of this thesis. The analysis shall be based on the variables temperature and precipitation. The results of the CCSM3 model are later embedded into and compared to the results of observational data and previous research. Finally, the CCSM3 model and its strengths and weaknesses in modeling extreme values are evaluated.

This thesis is structured as follows: chapter 2 gives an overview on the model and measured data. Moreover the statistical tools are presented using artificially produced data as an example. The results of the analysis of the model simulations and a discussion are presented in chapter 3. In chapter 4 some conclusions are presented, and the model is evaluated by comparing results with reconstructions and literature. The final chapter 5 gives an outlook on possible future work on the topic of extreme event analysis.

Chapter 2

Model and Methods

The present study is based on the data of the simulations of the Community Climate System Model Version 3 (CCSM3). This chapter will first give a short overview on the climate model and the data used. Further the statistical methods applied to analyze the climate model are described in more details.

2.1 Model and Data

2.1.1 Community Climate System Model Version 3 (CCSM3)

The Community Climate System Model Version 3 (CCSM3), developed by the National Centre for Atmospheric Research (NCAR), is a coupled model that simulates the climate for the past, present and future. It consists of four components for the atmosphere, ocean, sea ice and land surface. The four components are linked through a coupler that exchanges fluxes and state information [*Collins et al.*, 2006].

The CCSM3 model is available in three different resolutions [*Kiehl et al.*, 2006]: low-resolution (T31x3), intermediate-resolution (T42x1) and high-resolution (T85x1). T31x3 has an atmospheric and terrestrial grid of $\sim 3.75^\circ \times 3.75^\circ$ and a ocean and sea ice grid of $\sim 3^\circ \times 3^\circ$. The intermediate-resolution model (T42x1) has a grid spacing of $\sim 2.8^\circ$ for the atmospheric and terrestrial components and $\sim 1^\circ$ for the ocean and sea ice components. Lastly, T85x1 has the finest grid: while the ocean and sea ice components have again a resolution of $\sim 1^\circ \times 1^\circ$, the model features a higher atmospheric and terrestrial resolution of about $1.4^\circ \times 1.4^\circ$.

The following paragraphs present the model components and their characteristics as they are applied in the calculations by *Hofer et al.* [2011].

Model components

The Community Atmosphere Model Version 3 (CAM3) describes the atmospheric component of the coupled model. CAM3 is initially applied for simulations of atmospheric chemical transport and chemical processes. It is based on primitive equations and includes a Eulerian spectral dynamical core [*Collins et al.*, 2006]. As the model applies a triangular spectral truncation at 31 wave numbers (T31), it has latitudinal and longitudinal resolution of approx-

imately 3.75°×3.75° (this corresponds to 96 longitudinal and 48 latitudinal grid boxes). The vertical resolution includes 26 unevenly spaced levels between the surface and the top at 2.9 hPa. It is denoted as a hybrid coordinate system: near the surface the pressure isolines follow the terrain (sigma-pressure levels), above 83 hPa the isolines transition into pure pressure levels. The calculation is performed with a semi-implicit leapfrog scheme and a time step of 30 minutes. The output used for this thesis corresponds to a half-daily mean.

The ocean component is based on the the Parallel Ocean Program (POP) [*Smith and Gent*, 2004]. It is calculated by primitive equations and has a dipolar grid [*Collins et al.*, 2006]. 100 longitudinal and 116 latitudinal grid boxes cover the Earth's surface, this corresponds to a latitudinal resolution of ∼3° and a longitudinal resolution varying between 0.6° and 2.8°. The numerical poles are located at South Pole in the Southern Hemisphere and over Greenland in the Northern Hemisphere. Setting the northern pole not over true North, but over a land mass such as Greenland, guarantees a singularity-free grid in the ocean. The vertical resolution describes 25 levels increasing from 8 m at the top to 500 m in the deep ocean (till a maximum depth of 5000 m).

The land surface model (Community Land Model Version 3 (CLM3)) shares the same horizontal resolution as the atmospheric model. It is though based on a nested subgrid hierarchy of scales representing land units, soil or snow columns, and plant functional types [*Collins et al.*, 2006]. Vertically 10 sub-surface soil layers (representing temperature and moisture of each layer) and up to five snow layers are used. Additionally, the River Transport Model (on an independent finer grid), simulating the horizontal transport of water, is coupled to the land surface model.

The Community Sea Ice Model version 5.0 (CSIM5), the sea ice component of the model, is calculated on the same horizontal resolution as POP. The model uses five ice thickness categories, which are further divided into four evenly spaced layers. In these sub-layers the vertical heat conduction through the ice is calculated [*Briegleb et al.*, 2004]. The computation is based on energy-conserving thermodynamics, employing the elastic-viscous-plastic ice rheology.

A detailed description of the CCSM3 model and its components is presented on the NCAR web page (http://www.ccsm.ucar.edu/models).

Experiments

Yoshimori et al. [2010] and *Hofer et al.* [2011] performed a series of model simulations which are used for this study. The experiments can be divided into two categories: (i) Control simulations (CTRL1500 and CTRL1990), where the external forcings are kept constant at a given level, (ii) transient ensemble simulations (TR01, TR02, TR03 and TR04) with time-varying forcings. Table 2.1 gives an overview of the simulations.

The CTRL1500 simulation is initialized from the control simulation of 1990AD, i.e., the initial conditions for the atmospheric state of the first year of the 1500 control run are those of the year 1990AD. The forcing level is consistent with the level of the year 1500AD and is kept constant for the entire length of the simulation (see Table 2.2).

The 1500AD control simulation is calculated until an approximate equilibrium is reached. For the subsequent transient simulations, the 1500AD control run is used as initial conditions. As the CTRL1500 is not quite in an equilibrium state, both simulations (CTRL1500 and transient simulations) are proceeded together. Until the control run reaches the equilibrium state, it follows a trend. The transient simulations can be detrended by using the trend of CTRL1500.

The four transient simulations are based on different years starting from CTRL1500 and applied to a time-dependent external forcing. The first transient simulation (TR01) starts from the year 21 of CTRL1500, the second simulation (TR02) from year 41, TR03 from year 32 and TR04 from year 43, respectively.

The natural and anthropogenic forcings influence the transient simulations from 1500-2000AD. After 2000AD until 2098AD the simulations are forced by the IPCC SRES A2 scenario. The forcing is composed of the solar variability, volcanic eruptions and a mixture of greenhouse gases (CO_2, CH_4 and N_2O) (Figure 2.1). Ice core data of *Blunier et al.* [1995], *Etheridge et al.* [1996], *Flückiger et al.* [1999] and *Flückiger et al.* [2002] provide the basis for the greenhouse forcing of the past centuries. Following *Yoshimori et al.* [2010], the solar forcing (solar constant S) is calculated using

$$S = 1365.0635\ \mathrm{Wm}^{-2} + 5.399 \cdot L_{\mathrm{net}}, \tag{2.1}$$

Table 2.1: Starting year and calculation length of the control runs and transient simulations.

Label	Description	Length (years)
CTRL1500	1500AD equilibrium simulation	653
CTRL1990	1990AD equilibrium simulation	480
TR01	1500-2098 Transient simulation	599
TR02	1500-2098 Transient simulation	599
TR03	1500-2098 Transient simulation	599
TR04	1500-2098 Transient simulation	599

Table 2.2: Forcing levels of the control simulation 1500

Forcing	CTRL1500	CTRL1990
CO_2	282.3 ppm	355 ppm
CH_4	704.3 ppb	1714 ppb
N_2O	268.7 ppb	311 ppb
CFC11	0	28 ppt
CFC12	0	50.3 ppt
Solar constant	1364.3 $\mathrm{W\,m^{-2}}$	1367 $\mathrm{W\,m^{-2}}$
Orbital year	1990AD	1990AD

where L_{net} denotes the net radiative forcing [*Crowley*, 2000] which is scaled to reconstructed data of *Lean et al.* [1995]. Finally, the volcanic forcing is determined using the total aerosol mass. *Crowley* [2000] reconstructed the volcano-based irradiance changes. These data were converted into total aerosol mass by using the linear regression coefficients out of the six strongest volcanic eruptions in the last 130 years [*Ammann et al.*, 2003]. The total aerosol mass is distributed and weighted in the lower stratosphere by a latitudinal cosine function satisfying the mass conservation (more aerosols in the lower latitudes). As for most of the eruptions an exact date is missing, volcanic aerosols are evenly added throughout the entire year of eruption [*Hofer et al.*, 2011; *Yoshimori et al.*, 2010]. To illustrate the volcanic forcing, the optical depth in the visual band is shown in Figure 2.1. It is a measure of the amount of light in the visible band that is either absorbed or scattered by the aerosols.

To model the future 100 years, the Intergovernmental Panel on Climate Change (IPCC) developed 40 emission scenarios describing the prospective world depending on demographic, social, economic, technological and environmental development. These 40 scenarios are divided into four families (A1, A2, B1 and B2). In the A2 storyline the IPCC describes a very heterogeneous world. Self-reliance and preservation of local identities provide the basis of the scenario. The population is continuously growing and the economy is primarily regionally oriented. Furthermore, economic growth and technological change are rather slow [*IPCC SRES*, 2000]. Regarding carbon dioxide emission, the A2 scenario still predicts a strong increase until 2100. However, according to *Le Quere et al.* [2009] the carbon emissions due to fossil fuel burning increased at a rate of 3.4% between 2000 and 2008 which is slightly above the rate estimated by the scenario A2.

The CCSM3 model used for this study includes the SRES A2 scenario to project the future greenhouse gas development. It starts to follow the IPCC SRES scenario A2 in the year 2001. While the greenhouse gas forcings increase in agreement with the scenario, the solar and the volcanic forcings are kept constant at a level of 1366.676 $\mathrm{W\,m^{-2}}$ and 0.0054128, respectively.

Climate sensitivity

According to the report of the Intergovernmental Panel on Climate Change (IPCC), climate sensitivity is a metric used to characterize the response of the global climate system to a

given forcing. The 'equilibrium climate sensitivity' is defined as "the global annual mean surface air temperature change experienced by the climate system after it has attained a new equilibrium in response to a doubling of atmospheric CO_2 concentration" [*IPCC*, 2007]. The report further states that the estimated likely range for climate sensitivity is 1.5°C to 4.5°C. This means that the equilibrium climate sensitivity is likely to lie in the range 2°C to 4.5°C with the most likely value of about 3°C [*IPCC*, 2007]. *Kiehl et al.* [2006] examine in their study the climate sensitivity for the CCSM3 model. They showed that climate sensitivity is resolution dependent, with an equilibrium response for the low-resolution model (T31x3) of 2.32°C. Compared to the values of the IPCC, the result of the CCSM3 model lies within, but at the lower end of the range.

2.1.2 ERA-40 Data set

The European Centre for Medium Range Weather Forecasting (ECMWF) constructed a 45-year re-analysis (ERA-40) data set of the atmosphere and surface conditions from September 1957 to August 2002, covering the whole globe [*Uppala et al.*, 2005]. A re-analysis data set is generated by the application of a data assimilation technique in a weather forecast model. Observations of the current state of the atmosphere are used as input data to run a numerical weather prediction model. This is done for a short time period, in case of the ERA-40 re-analysis six hours. Observational data arise from diverse sources as radio soundings, marine data, aircraft data and satellite data [*Uppala et al.*, 2004]. The combination of the model output and the observations serves as the best fit of the current climate. By advancing the model in time, the foregoing result acts as forecast in the next analysis cycle.

The aim of a re-analysis data set is to balance errors in the observing system and errors in the model computation. Its result is an accurate representation of the climate and can be used to improve climate and weather prediction models. Through the process of data assimilation, model outputs covering the whole world are available. Furthermore, other variables than measured are calculated and can be used [*Uppala et al.*, 2005]. The data used is resolved on a $2.5° \times 2.5°$ grid in longitude and latitude and on 23 pressure levels. Four model outputs per day are available. For further analysis, the outputs on 00 and 12 UTC are chosen.

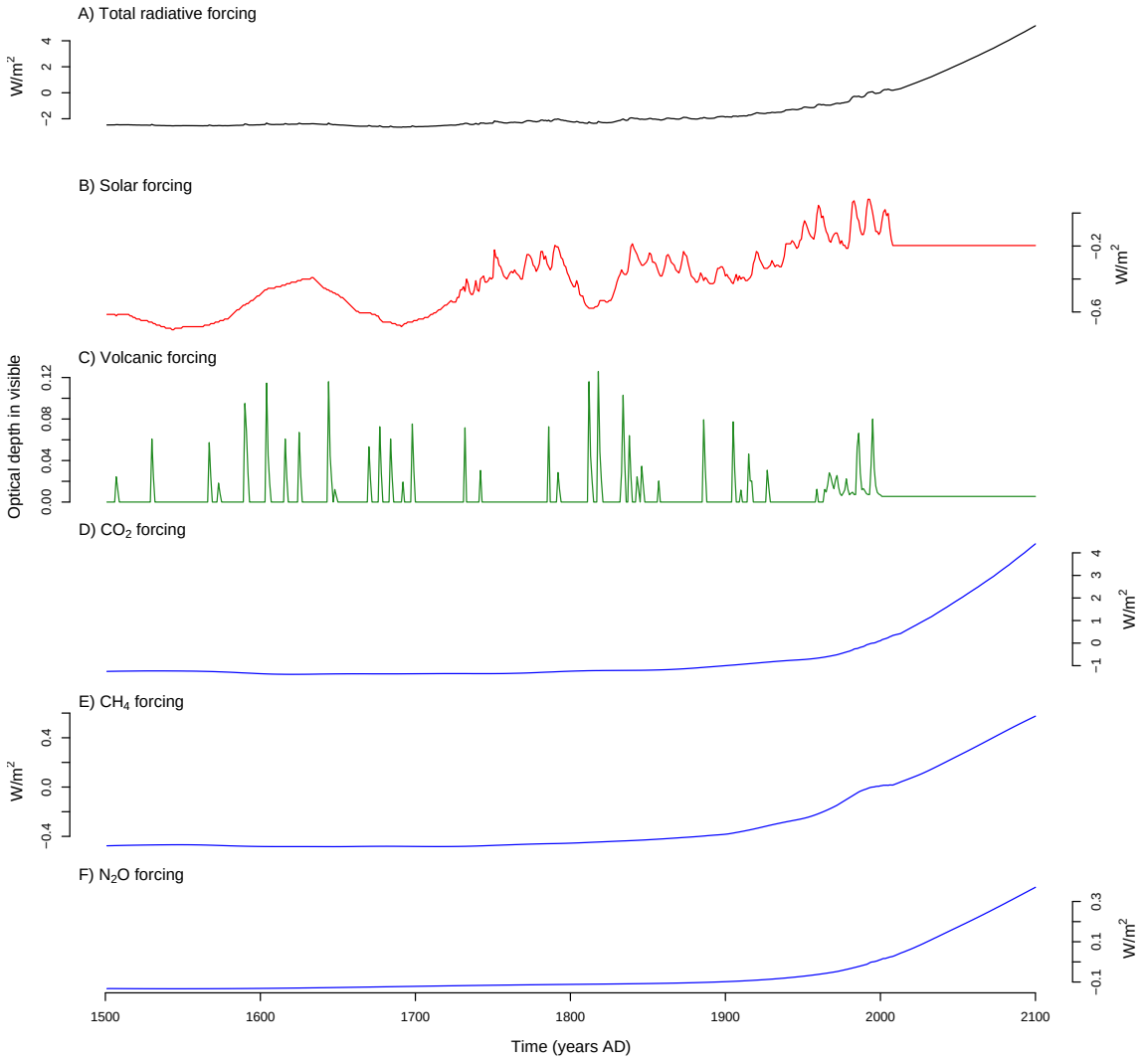

Figure 2.1: Natural and anthropogenic forcings applied in the transient simulations: A) Total radiative forcing (in $\mathrm{W\,m^{-2}}$), calculated as the sum of the solar and greenhouse gas forcing (according to Table 6.2 in *IPCC* [2001]), B) solar forcing (in $\mathrm{W\,m^{-2}}$), D) volcanic forcing (optical depth in visible), D) - G) greenhouse gas forcing (carbon dioxide, methane and nitrous oxide in $\mathrm{W\,m^{-2}}$ as well).

2.2 Extreme Value Statistics

In this thesis, the data sets described earlier are analyzed with respect to extreme values. By definition, extreme values are scarce values which are much greater (smaller) than the mean of the observed data [*Coles*, 2001]. The so-called extreme value analysis was conducted according to the theory summarized by *Coles* [2001]. In his book *An Introduction to Statistical Modeling of Extreme Values* Stuart Coles described the scientific basis of extreme value modeling which is broadly applied in climate sciences and shall be the basis for this work as well.

The extreme value theory and models are presented by the aid of artificial time series. For that reason, series of white and red noise (in addition of different trends) were built. The white noise data set is a simple series of normally distributed random variables with zero mean and a standard deviation of one. Red noise, also called Markov process of first order, is a stationary sequence of random variables, of which the future evolution depends on the current value [*Coles*, 2001]. It is composed as follows:

$$r(i+1) = a \cdot r(i) + w(i) + t(i), \tag{2.2}$$

$r(i)$ denotes the value of red noise at time step i, $w(i)$ is the white noise value at time step i and a is the auto correlation coefficient with lag one. To the pure red noise sequence different trends $t(i)$ can be added. In particular, a positive linear and a positive quadratic trend were added, as these kind of trends are most prominent in the transient simulations of the CCSM3 model:

$$t_{lin}(i) = b \cdot i + c, \tag{2.3}$$

$$t_{qua}(i) = b \cdot i^2 + c \cdot i + d. \tag{2.4}$$

The linear trend is calculated using Eq. 2.3, the quadratic trend by Eq. 2.4, respectively. As an example, Figure 2.2 shows the most important properties of the noise time series.

White ($a = 0$) and red noise ($a = 0.5$) time series differ just slightly. During the whole calculation period they have the same structure and vary around the same mean. Red noise shows larger extremes though. This makes sense, if it is considered that red noise consists of white noise in addition to a recursive value. The addition of a trend causes a shift in the mean of the distribution. This results on the one hand in an increasing intensity of extreme values (predominately towards positive values) and on the other hand in a change of frequency (Figure 2.2 B). In principle this is valid for both, the linear and quadratic trend, but it is stronger for the quadratic trend. This artificial example shows a similar pattern as the temperature series analyzed and modeled by *Schär et al.* [2004] (compare Figure 1.1) and thus is suitable to test the extreme value calculation.

Basically, extreme values can be analyzed using two different approaches. Either by the application of the classical extreme value theory or of threshold models. These two approaches are described in the following subsections. The underlying theory is summarized according to *Coles* [2001].

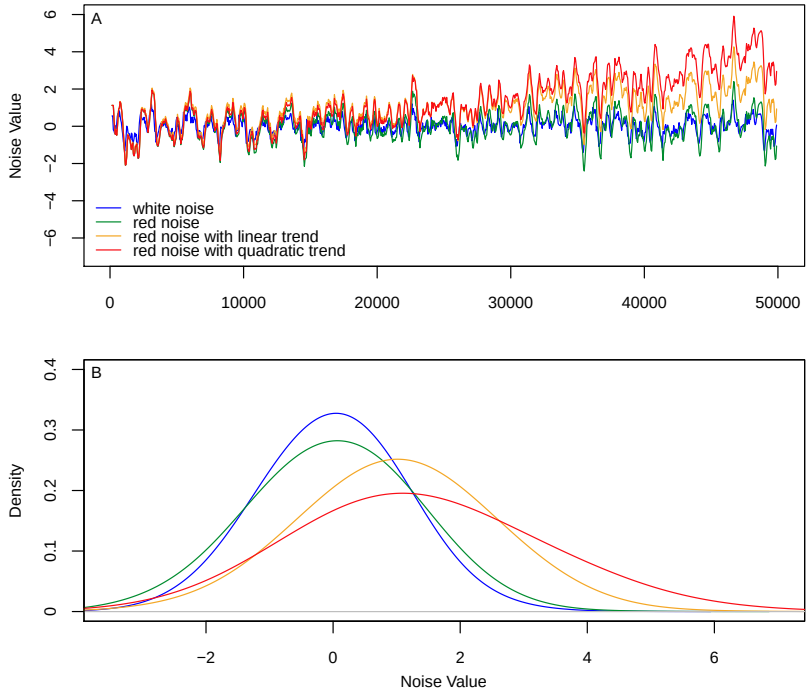

Figure 2.2: A) Noise time series: noise values are plotted against time. B) Probability density functions of noise time series. While white and red noise share the same mean, the mean for the trended time series is clearly shifted toward higher values.

2.2.1 Classical Extreme Value Theory

Classical extreme value theory bases on the generalized extreme value distribution. It focuses on the behavior of the maximum value of a process over n time steps, so-called block maxima:

$$M_n = max\{X_1, ..., X_n\}. \tag{2.5}$$

If there are sequences of constants $\{a_n > 0\}$ and $\{b_n\}$, the probability density function ($Pr\{\}$) can adopt the following form:

$$Pr\{\frac{M_n - b_n}{a_n} \leq z\} \rightarrow G(z), \tag{2.6}$$

where G is the distribution function of an extreme value model:

$$G(z) = \exp\left\{ -\left[1 + \xi\left(\frac{z-\mu}{\sigma}\right)\right]^{-\frac{1}{\xi}}\right\}. \tag{2.7}$$

Three unknown parameters describe the model distribution: the location parameter μ gives the center of the distribution, the scale parameter σ specifies the size of deviations around the location parameter and the shape parameter ξ governs how rapidly the upper tail decays [*Katz*, 2010]. For a normally distributed data set, the location and scale parameters

correspond to mean and standard deviation, respectively. Depending on the values of the parameters, there are three families of density functions which differ in tail behavior. The Gumbel family corresponds to $\xi = 0$, describing a exponential upper tail. $\xi > 0$ has a heavy upper tail and it belongs to the Fréchet family. The Weibull family ($\xi < 0$) describes a distribution with a finite upper end point. Hence the shape parameter ξ has largest influence on the upper tail distribution. Figure 2.3 is calculated with random, normal distributed data. Even if the three families share the same location ($\mu = 0$) and scale ($\sigma = 1$), their appearance is dissimilar. The Gumbel and Fréchet families, both show a heavier upper tail and a lighter lower tail. For the Fréchet family though, this pattern is even stronger. The Weibull family, on the other hand, shows a heavy lower tail and a smaller upper tail.

The challenge in the classical extreme value analysis, is to find the extreme value model that fits best to the data. To fit the model, μ, σ and ξ can be estimated by using the maximum likelihood technique. The principle of maximum likelihood estimation (MLE) is to adopt the model with greatest likelihood to cover the observational data (or in the framework of this thesis to cover the model data of CCSM3). Maximizing Eqs. 2.8 and 2.9 leads to the maximum likelihood estimation of the parameter vector (μ, σ, ξ):

$$l(\mu,\sigma,\xi) = -m\log\sigma - (1+\frac{1}{\xi})\sum_{i=1}^{m}\log\left[1+\xi\left(\frac{z_i-\mu}{\sigma}\right)\right] - \sum_{i=1}^{m}\left[1+\xi\left(\frac{z_i-\mu}{\sigma}\right)\right]^{-\frac{1}{\xi}}, \quad (2.8)$$

$$l(\mu,\sigma,\xi) = -m\log\sigma - \sum_{i=1}^{m}\left(\frac{z_i-\mu}{\sigma}\right) - \sum_{i=1}^{m}\exp\left(-\frac{z_i\mu}{\sigma}\right), \quad (2.9)$$

if $\xi \neq 0$ (Fréchet and Weibull family) Eq. 2.8 is applied, in the case of $\xi = 0$ (Gumbel family) the parameters are estimated using Eq. 2.9. The three families are divided concerning the shape parameter ξ.

MLE is a very general and powerful estimation technique. Even though it is numerically more complex than for example L-moments, MLE is preferred as it is more efficient and accurate for samples that are not exactly identically distributed. As long as the sample size is big enough, MLE shows smaller biases in parameter estimation [*Kharin and Zwiers*, 2005].

The classical extreme value theory assumes identically distributed and independent time series. Both noise time series contain 55,000 values, with a chosen block size of 275 values, this results in 200 maxima. Red noise is not exactly independent (compare Eq. 2.2), but as the auto correlation coefficient a is set to 0.5, the time series can be assumed as independent for this example. As the time series fluctuates around a zero mean, there is no trend or seasonality violating the assumptions. The time series is shown in Figure 2.2 (A and B: blue for white noise and green for red noise). A generalized extreme value (GEV) distribution function $G(z)$ is fitted to both, white and red noise. The diagnostic plots for red noise fitting are shown in Fig 2.4. Table 2.4 contains all estimated parameters for all noise time series and the two analysis methods GEV and GPD (see next chapter).

The results of the GEV parameter estimation indicate an extreme value function with a mean (μ) of 3.07 and standard deviation (σ) of 0.39. The shape parameter ξ suggests a Weibull family distribution. As the sequence of block maxima is large enough ($n = 200$), the standard

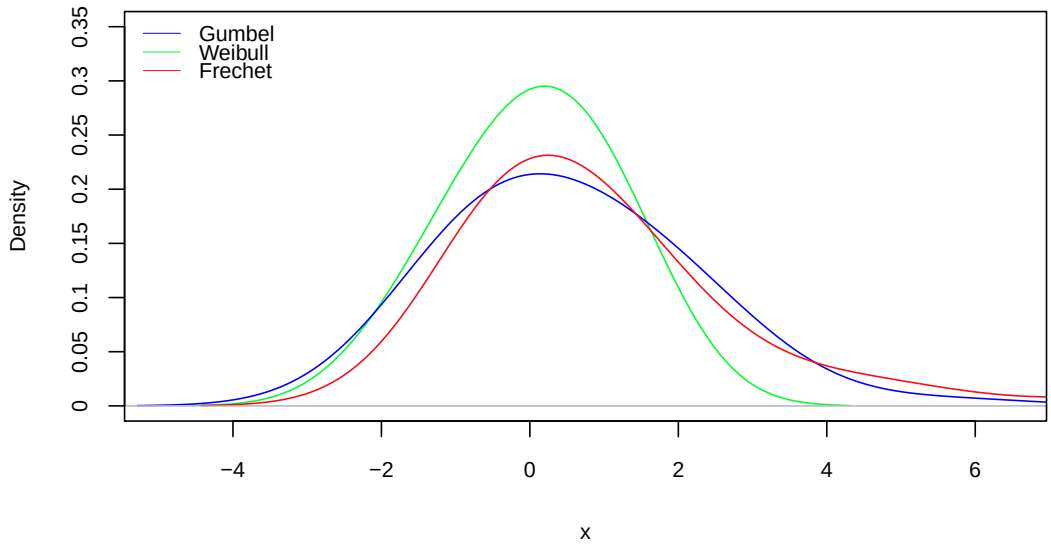

Figure 2.3: GEV families in comparison. The probability density functions are calculated on the basis of normal distributed random data and simulated with the same location and scale parameter.

errors are reasonably small.

Four plots describe graphically the characteristics of the red noise fitting (Figure 2.4). The probability plot (A) and quantile plot (B) are statistical tools to visually compare two data sets: model estimations of the GEV distribution model and the red noise data set. In the probability plot the cumulative distribution functions (CDF) of the two data sets are plotted against each other. The cumulative distribution function (or just distribution function) describes the probability that a random variable is equal to a specific value. If points of the CDF are taken at regular intervals, one speaks of quantiles. The quantiles of the two data sets are plotted in the quantile plot. If the calculated points lie on, or are arranged close to, the diagonal, the extreme value model fits the observational data. In the case of the red noise data set, there is no doubt about the validity of the fitted model. Return levels (on the y-axis) of different return periods (on the x-axis) are plotted in the return level plot (C). Lastly, plot (D) shows the density distribution. For the analysis the quantile and return level plots are the most informative.

In the case of red noise, the GEV function fits the data set fairly well. This bases on the one hand on the reasonable choice of blocks and block sizes and on the other hand on the trendless distribution. Block size is the critical parameter for model imprecision, though. If the block definition is too small, it is possible that values, which are not exactly extremes, are considered to be extremes. On the other side, too large blocks could imply the loss of valuable

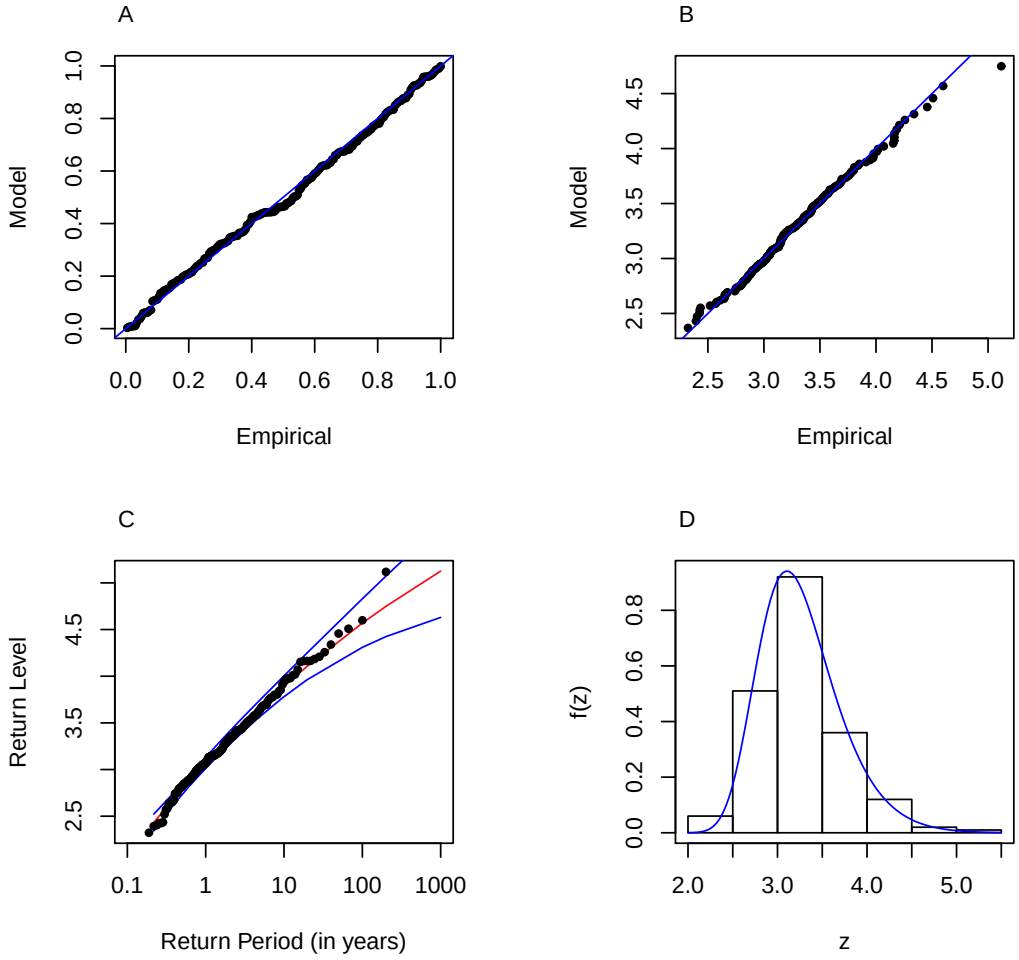

Figure 2.4: Diagnostic plots for the GEV fit to the red noise time series. A) Probability plot: cumulative distribution function of the noise series versus fitting function, B) Quantile plot: noise quantiles versus fitting function quantiles, C) Return level plot: probability of the return of an extreme value, and D) Density plot: distribution of the noise block maxima.

information about the upper tail of the underlying distribution. The first possibility to avoid this problem is to extend the block maxima approach to a r-largest order statistic model. The r-largest order statistic model considers several maxima per block (r as the number of values per block as maxima). Using this approach, one mitigates the problem of information loss [*James*, 2011].

The second possibility to investigate the upper tail distribution are threshold models, which will be presented in the next section.

Table 2.3: Estimated parameters for GEV and GPD fitting on white and red noise time series, as well as for a linear and quadratic trend on red noise. The parameter values are estimated over a maximum likelihood estimation.

		GEV		GPD	
		mle	se	mle	se
White Noise	μ	2.69	0.03		
	σ	0.35	0.02	0.37	0.03
	ξ	-0.06	0.05	-0.09	0.06
Red Noise	μ	3.09	0.03		
	σ	0.42	0.02	0.39	0.03
	ξ	-0.10	0.04	-0.04	0.06
Linear Trend	μ	3.61	0.04		
	σ	0.55	0.03	0.38	0.03
	ξ	-0.17	0.03	-0.05	0.06
Quadratic Trend	μ	4.37	0.08		
	σ	1.05	0.06	0.52	0.04
	ξ	-0.22	0.06	-0.15	0.05

2.2.2 Threshold Models

Another possibility to define extreme values is to choose a threshold u. All values lying above (or beyond) that threshold are considered to be extreme values. Corresponding to the block maxima approach, threshold excesses have a distribution function $H(y)$:

$$H(y) = 1 - \left(1 + \frac{\xi y}{\tilde{\sigma}}\right)^{-\frac{1}{\xi}}, \tag{2.10}$$

for $\{y : y > 0 \text{ and } (1 + \frac{\xi y}{\tilde{\sigma}}) > 0\}$ as well as $\tilde{\sigma} = \sigma + \xi(u - \mu)$. Eq. 2.10 defines a family of distribution functions called generalized Pareto distribution (GPD) functions. A function of the generalized Pareto family is fitted to the threshold exceedances. The parameters are again estimated by applying maximum likelihood approximation. In contrast to the generalized extreme value function, the generalized Pareto distribution function is described only through the scale parameter (σ) and shape parameter (ξ). For the threshold model approach, it is assumed that the exceedances are identically distributed (no seasonality or trend), independent and that the threshold is sufficiently large.

The approach of defining a threshold differs from the block maxima approach through the definition of extreme values. The choice of a threshold implies a source of errors as well. A too low or too large threshold violates the model and leads to high variances. The aim is to find a threshold that minimizes the variances within the model.

Ideal thresholds u are found by plotting the mean excess of the threshold u:

$$E(X - u|X > u) = \frac{\sigma_{u0} + \xi u}{1 - \xi}. \tag{2.11}$$

According to Eq. 2.11, estimates change linearly with u. For a valid approximation of the generalized Pareto distribution to the excess distribution, the mean residual life plot should nearly be linear in u. This technique is explained on the example of white noise. Above a threshold of $u = 2.6$ there is approximate linearity (Figure 2.5). Setting u at 2.6 results in 195 exceedances, which is approximately the same number of extreme values as for red noise in the GEV analysis.

To refine the search of the proper threshold, two parameters (modified scale $\hat{\sigma}^*$ and shape $\hat{\xi}$) are estimated and plotted against u. Structural interruptions are a indication of a threshold within the data. Threshold u is chosen as the lowest value for which the estimates remain near-constant. In Figure 2.6 a major interruption is seen at $u = 2.35$ and a smaller perturbation at approximately $u = 2.6$. For the purpose of comparability with GEV, the threshold is set at $u = 2.6$.

Table 2.4 lists the estimated parameter of the generalized Pareto model fitting to all time series and different thresholds. The threshold for red noise fitting is set at $u = 3$, for red noise with a linear trend at $u = 3.7$ and for red noise with a quadratic trend at $u = 5.4$. For white and red noise, these results are in a comparable range to the GEV analysis. Both approaches lead to similar scale and shape parameter values, as well as reasonable small standard errors.

The diagnostic plots (Figure 2.7) indicate the goodness of fit of the generalized Pareto distribution model to the white noise data. These plots indicate similar model results for red and white noise, as well. According to the probability plot, as well as quantile plot, the threshold model fits doubtlessly on the white noise data set.

In the case of red and white noise analysis, there is no difference in the application of the classical extreme value theory or the threshold model. The weakness of the block maxima approach lies in the loss of information if there is more than one extreme value in one block than in another. Considering the threshold model, if u is improperly chosen the asymptotic argument (minimizing the variance within the model) behind the GPD fitting weakens [*James*, 2011]. The choice of the used modelling approach is therefore dependent on the nature of observations. In the framework of the current thesis, the block maxima approach will find broader application. The GPD fitting will only be used in case of a pre-given exact threshold that has to be analyzed.

2.2.3 Return Levels

By the process of function fitting, one tries to characterize the behavior of the extreme value distribution of a data set. For practical applications, values of estimated parameters are not very informative. Hence, the concept of the n-year return levels is the main practical application of extreme value model fitting. Through the comparison of return levels, it is possible to determine changes in extreme values. The return level is denoted by z_p with return period $1/p$, while p is the probability of exceedance. More precisely, the level z_p is expected to be exceeded on average once every $1/p$ years. Return levels z_p of GEV fitted

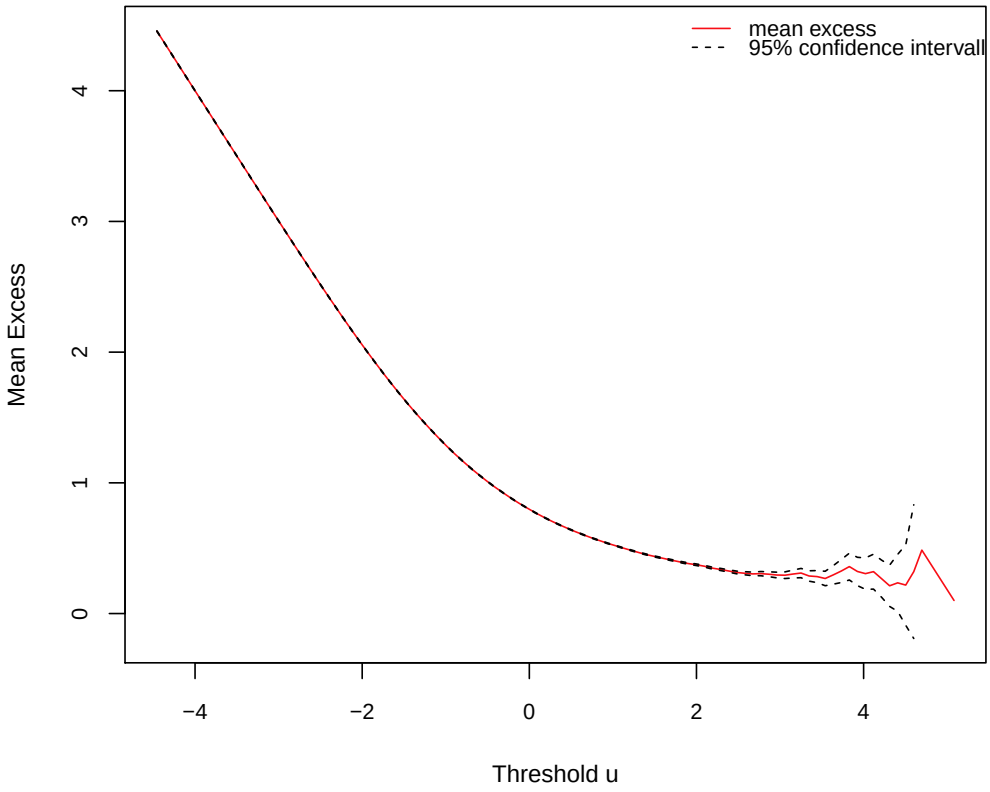

Figure 2.5: Distribution of the mean excess of threshold u.

functions are calculated by using Eq. 2.12.

$$z_p = \begin{cases} \mu - \frac{\sigma}{\xi}[1 - y_p]^{-\xi}, & \text{for } \xi \neq 0, \\ \mu - \sigma \log y_p, & \text{for } \xi = 0, \end{cases} \tag{2.12}$$

for y_p defined as $-\log(1-p)$. Eq. 2.13 is used to estimate the return levels of GPD fitted data (y_p).

$$z_p = \begin{cases} \frac{\hat{\sigma}_u}{\hat{\xi}}\left[\left(\hat{\phi}_u N n_y\right)^{\hat{\xi}} - 1\right] + u, & \text{for } \hat{\xi} \neq 0, \\ \hat{\sigma} \log\left(\hat{\phi} N n_y\right) + u, & \text{for } \xi = 0, \end{cases} \tag{2.13}$$

n_y is the number of observations in each block of data (e.g. 365 for daily annual observations) [*James*, 2011].

An example of a return level plot is already given in the diagnostic plots of GEV and GPD fitting (see Figure 2.4 and Figure 2.7). Though, better accuracy in visualizing return levels can be achieved by reducing the number of independent parameters, the so-called profile

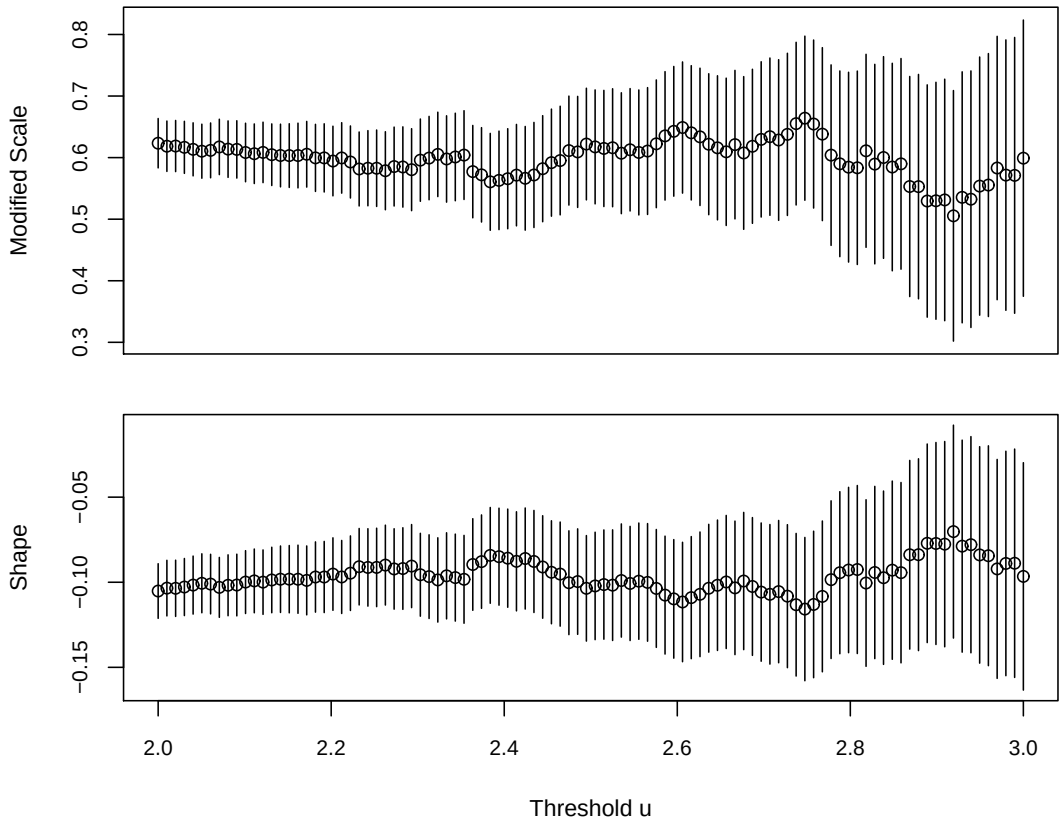

Figure 2.6: Plot of estimated parameters against threshold for white noise.

likelihood. The return level can be determined by maximizing the profile likelihood. Figure 2.8 is an example for the 10 and 100 years return periods of GEV fitted red noise. In Table 2.4 return levels for GEV and GPD fitted white noise, red noise without trend, linear trend and quadratic trend are compared. Both analysis methods lead to an increase in return levels when comparing white noise to red noise with a quadratic trend. Comparing the single time series, large deviations can be found. While the GPD fitted white noise return levels are slightly smaller than the GEV fitted return levels, the return levels for the three red noise time series of the GPD method are substantially larger than those of the GEV method. The generalized extreme value method seems to manage trends better than the generalized Pareto distribution method.

To estimate the behavior of temperature and precipitation extremes, the concept of return levels on specific return periods will be broadly applied in the current thesis. On the basis of return levels different regions and different time slices can be compared.

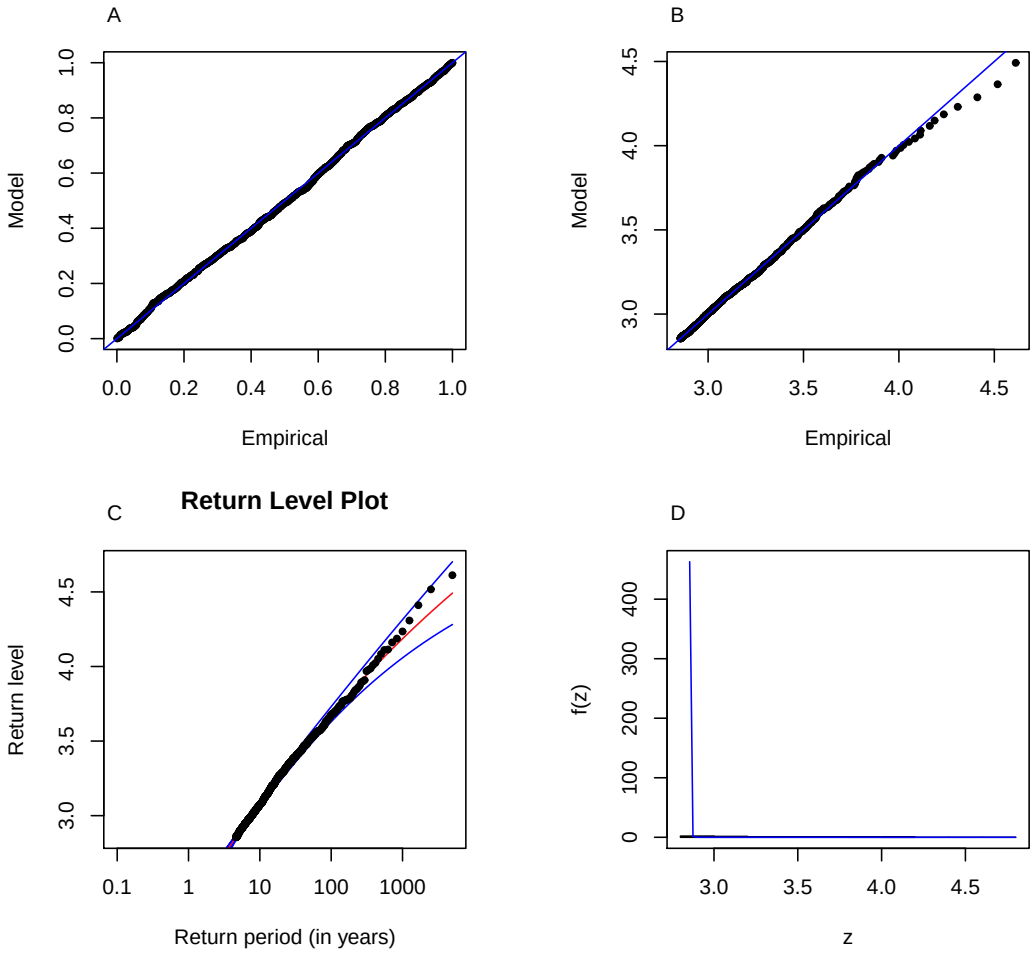

Figure 2.7: Diagnostic plots for the GPD fit to the white noise time series: A) Probability plot, B) Quantile plot, C) Return level plot and D) Density plot.

2.2.4 Handling of Trends

According to *Katz* [2010] the statistical theory of extreme values has been primarily applied to climate under the assumption of stationarity, even though climate is not stationary on longer time scales. Climate time series violate the assumption of stationarity through trends and seasonality. Especially if transient time series over hundreds of years are analyzed,which is the case in the current thesis, the handling of trends can not be ignored [*Katz*, 2010].

Katz [2010] presents two ways of dealing with non-stationarity. Either a trend is added to the extreme value distribution [*Nikulin et al.*, 2011] or the data is transformed by using Poisson regression and then analyzed by applying the Generalized Pareto distribution model [*Katz*, 2010]. Still, these two possibilities are not unbiased. One complication arises if exceedances occur in clusters (e.g. for persistent climate variables), they can not be analyzed sufficiently.

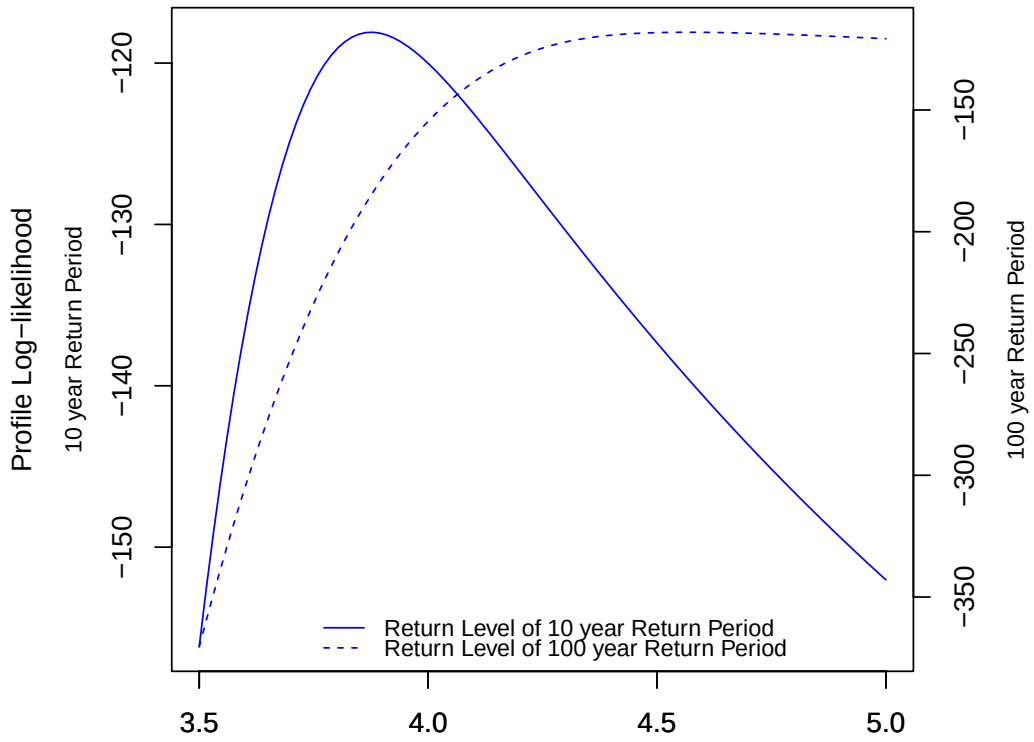

Figure 2.8: Return levels for a 10-year (filled line) and a 100-year (dashed line) period of the red noise data set.

Considering extreme clustering for time series with a trend, a specific threshold cannot consider extremes over the entire time series. This implies that the concept of return periods and return levels can no longer be applied for non-stationary climate as it would lead to incorrect results [*Katz*, 2010]. Furthermore, a detrending of, for example, precipitation could lead to negative values which is not appropriate. For these reasons, none of the approaches was chosen.

To avoid trends and seasonality within the data, the time series are simplified. They are not examined as a whole, instead the time series are cut into slices of 30 years and each season is analyzed separately. This method has already been chosen in several studies before [*Frei et al.*, 2006; *Kharin and Zwiers*, 2005; *Nikulin et al.*, 2011]. The selection of a 30-year time slice enables an analysis under the assumption of stationarity, as the trend is supposed to

Table 2.4: Estimated parameters for GEV and GPD fitting on white and red noise time series. As well for a linear and quadratic trend on red noise. The parameter values are estimated over a maximum likelihood estimation.

	GEV		GPD	
	10yr	100yr	10yr	100yr
White Noise	3.5	4.1	3.1	3.8
Red Noise	3.9	4.7	6.5	7.0
Linear Trend	4.6	5.3	7.9	8.3
Quadratic Trend	6.2	7.4	8.7	8.7

be negligible. By examining every single season separately, no seasonality is included in the time series anymore. Figure 2.9 shows a temperature and precipitation time series from 1961 to 1990 for the Mediterranean. The blue line denotes the time series including a trend, the red line was calculated by subtracting a quadratic trend. Furthermore, the time slices are plotted at two different seasons (DJF = December, January and February, JJA = June, July and August). It can be seen that the two lines of the trended and detrended time series are mostly congruent. Only small shifts can be detected. This result supports the approach of neglecting trend and seasonality.

Still, as there are small trends within the data, the classical extreme value theory was tested on its robustness. Red noise with a slight linear and a slight quadratic trend was analyzed on extreme values. Table 2.4 presents the result of the analysis. The results of the estimated GEV parameters are similar to red noise analysis presented above. Still, as it would be expected for variables with a small trend, the resulting GEV parameters are slightly higher compared to a simple red noise time series. The according standard errors are considerably smaller for both linear and quadratic trended red noise. This leads to the assumption that the classical extreme value theory is robust against small trends.

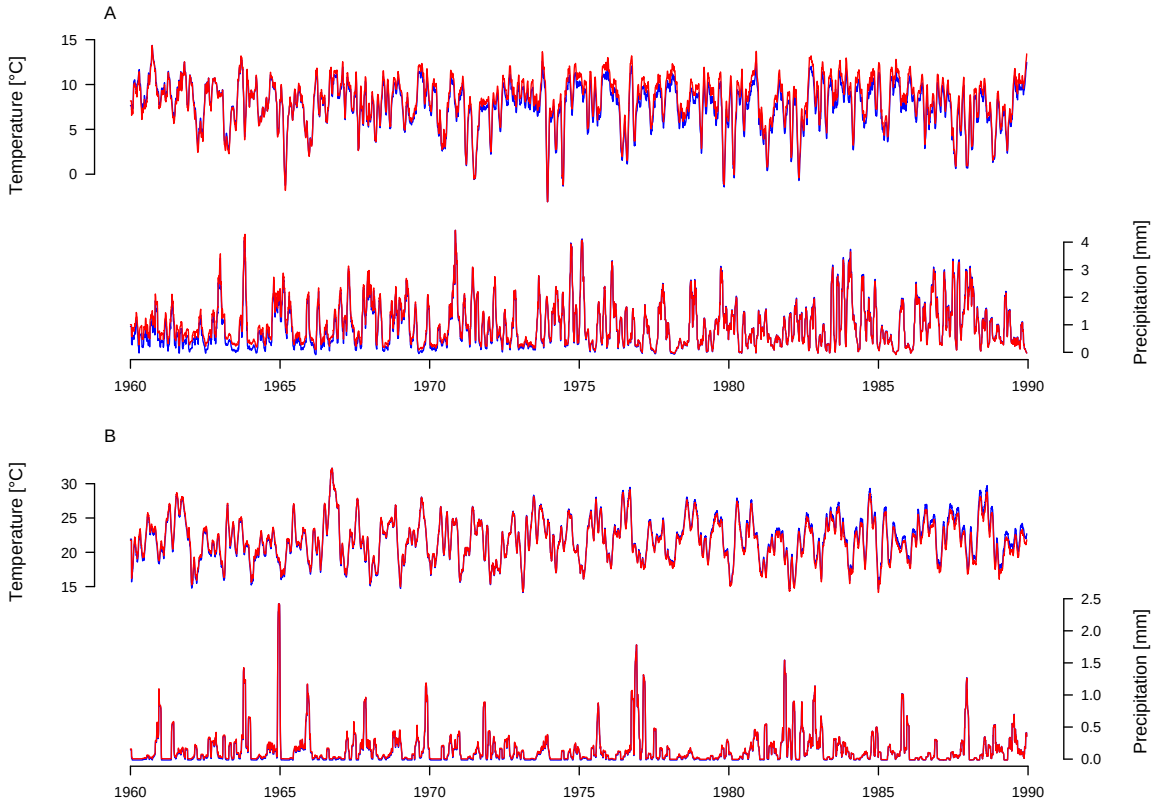

Figure 2.9: Temperature and precipitation time series of 1961-1990AD for the Mediterranean: original time series in blue, detrended values in red. The upper panel shows the values for DJF, the lower panel for JJA.

2.3 Indices

2.3.1 Warm and Cold Spells

Cold and warm spells (also denoted as heat waves) are analyzed according to *Meehl and Tebaldi* [2004], *Buehler et al.* [2011] and *Fischer and Schär* [2010].
A heat wave is defined as a spell of at least six consecutive days where the maximum temperature exceeds the local 90^{th} percentile of the control period 1961 - 1990 [*Fischer and Schär*, 2010]. Similarly, a cold spell is defined as a spell of at least six consecutive days where the minimum temperature lies beyond the local 10^{th} percentile of the control period 1961 - 1990. Warm and cold spell indices (WSDI and CSDI) are calculated according to the definitions of Expert Team on Climate Change Detection and Indices (ETCCDI):

$$WSDI : TX_{ij} > TX_{ref90}, \tag{2.14}$$

$$CSDI : TN_{ij} < TN_{ref10}, \tag{2.15}$$

TX (TN) denotes the maximum (minimum) temperature of a day i in a year j. The above statements have to be valid for at least six consecutive days.

In the context of the present thesis, warm (cold) spells are characterized through the number of occurrences within a period of time and the maximum duration.

2.3.2 Standardized Precipitation Index

To extend the analysis of droughts and wetnesses, another index is calculated. The Standardized Precipitation Index (SPI) is a probability index that gives a representation of extraordinary wetness or dryness [*Guttman*, 1999]. If the SPI is normally distributed, it is able to monitor wet as well as dry periods [*McKee et al.*, 1993].

The SPI is used to measure droughts and wetnesses on different time scales, usually ranging from 3 to 48 months [*Edwards et al.*, 1997]. The final index is simply calculated by the distance of a score (x) to the average in standard deviation units [*Giddings et al.*, 2005]:

$$SPI = \frac{x - \mu}{\sigma}, \tag{2.16}$$

μ denoting the mean and σ denoting the standard deviation of the time series.
Before the SPI is standardized (Eq. 2.16), the precipitation time series has to be pre-adjusted. The precipitation data or model output is transformed to a Gaussian distribution by the application of the gamma function [*Edwards et al.*, 1997; *Giddings et al.*, 2005]. Drought and wetness is arbitrarily divided into the categories presented in Table 2.5.

Drought can be measured at different time scales, depending on the number of months taken into account. Usually, drought appears first in the short time scales and if dry conditions persist, drought will develop on longer time scales [*McKee et al.*, 1995]. A 3-months SPI is accurate for a seasonal estimation of precipitation, it reflects the short-range moisture conditions. Medium-range moisture conditions are described by the 6- and 9-months SPI. The 12- and 48-months SPI reflects long-term moisture conditions. Even if *Guttman* [1999] states in his paper that a SPI on time scales longer than 24 months may be unreliable, it is anyway calculated in the framework of this thesis. This can be justified by the longer time series taken into account. Calculating SPIs on time scales of 48 or even 72 months, the SPI time series is less noisy and therefore easier to interpret.

Table 2.5: Standardized Precipitation Index: drought and wetness categories after *Guttman* [1999]

SPI	Intensity
$\leq$ - 2.0	extremely dry
- 2.0 to - 1.5	moderately dry
- 1.5 to - 1.0	dry
- 1.0 to 1.0	neutral
1.0 to 1.5	wet
1.5 to 2.0	moderately wet
$\geq$ 2.0	extremely wet

The Standardized Precipitation Index is preferred to the more widely used Palmer Drought Severity Index (PDSI). While the SPI depends only the amount of precipitation, the PDSI requires more information, for example about soil type and potential evaporation. With the PSDI, the spectral characteristics can therefore vary from site to site, while it stays constant for the SPI [*Guttman*, 1998]. As the SPI is standardized, its values represent the same probabilities of occurrence independent of time period, location and climate.

2.4 Geography and Time Slices

In the present thesis extreme values are analyzed over the mid-latitudes, especially over Europe. Three areas are chosen to compare different latitudes: a Mediterranean area, a Central and a Northern European area. For each area a representative location is selected to analyze time series. Figure 2.10 illustrates these three areas and their representative locations.

As mentioned earlier, the entire period from 1500 to 2100AD is not analyzed as a whole, but is cut into time slices of 30 years and analyzed separately, instead. The thesis concentrates on four specific time slices. Once a time slice during the Maunder Minimum 1661-1690AD is chosen to detect the extreme value behavior. The Maunder Minimum is a period of reduced solar activity and a nearly disappearing number of sunspots [*Eddy*, 1976; *Beer et al.*, 1998]. This period reaches from 1645 to 1715AD and concurs with the coldest years of the Little Ice Age (LIA) (*NASA Earth Observatory*, source: http://earthobservatory.nasa.gov/IOTD/view.php ?id=7122 [16.09.2011]). The other three time slices are chosen according to other studies done on a similar topic, in order to be able to compare the results. 1851-1880AD represents the pre-industrial period, a time of low human impact. 1961-1990AD is considered as present-day reference period and 2071-2100AD as the period of projected future changes.

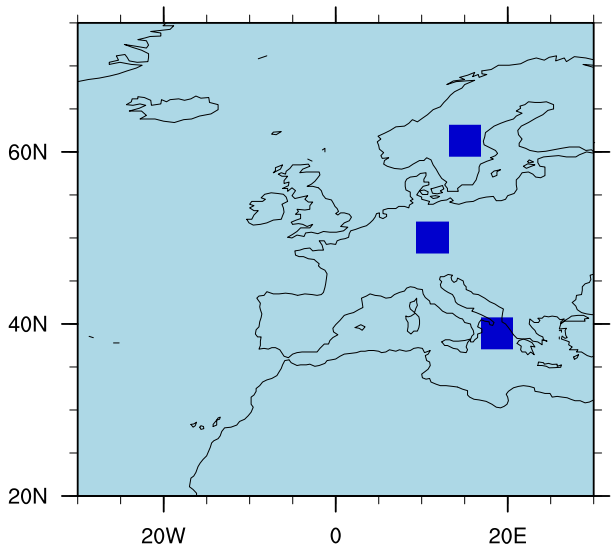

Figure 2.10: Map of greater Europe: the blue dots locate the representative grid points for the time series analysis of the areas.

Chapter 3

Results and Discussion

3.1 Temperature

3.1.1 Extreme Climate

Climate indices

A first overview of temperature extremes is obtained by climate indices, estimated at each grid point. The ETCCDI defined 27 core indices to describe the extreme climate. The number of ice days is chosen to depict winter temperatures. The extremes in summer temperatures are examined by the number of summer days. An ice day is defined as a day with a maximum temperature not higher than 0°C. On a summer day, on the other hand, the maximum temperature lies over 25°C. The number of ice/summer days shall indicate the spatial extreme temperature distribution during different periods of time.

The number of ice days, as well as the number of summer days, is given as a 30-year mean for four time slices: 1661-1690AD, 1851-1880AD, 1961-1990AD and 2071-2100AD. To illustrate the changes, differences to the reference period 1961-1990 are shown in Figure 3.1 and Figure 3.2. The mean pattern of the reference period shows that the largest number of ice days per year are calculated for Northern Europe, an enhanced number can be found in Eastern Europe. The distribution in the Maunder Minimum, as well as the pre-industrial period are similar. In comparison to the reference period, the Maunder Minimum turns out to be the coldest period. The model calculates in a band from Central Europe to the north Sea more ice days. Also the pre-industrial period shows more ice days, all though the number is smaller than in the Maunder Minimum. As expected, the future experiences a pronounced warming, which can be seen in the large scale decrease of ice days in Northern Europe.

A similar result is obtained by the analysis of summer days. Most summer days are calculated for Northern Africa and the Mediterranean in the reference period. Further north, the number of summer days decreases to zero. The spatial pattern is similar for all time slices, except the future. The distribution of summer days experiences a shift towards the north as time proceeds. The Maunder Minimum is again the coldest period, followed by the pre-industrial time slice and the reference period. The future time slice shows by far the largest number of summer days in Central Europe. Considering the differences to the reference period (Figure 3.2), the most pronounced changes occur in Central Europe and the Mediterranean

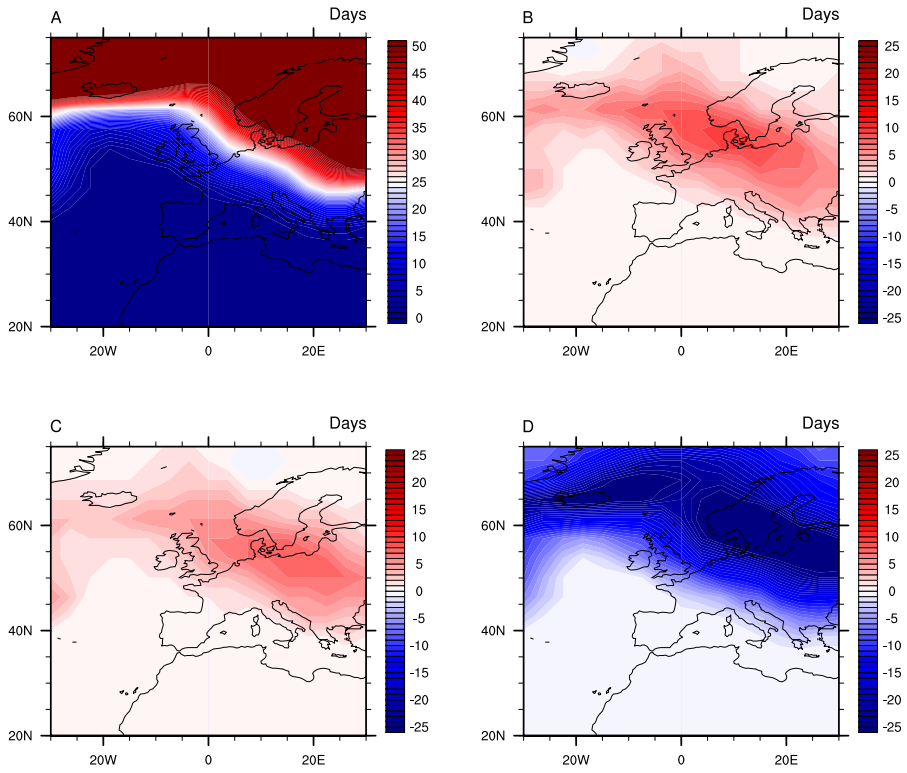

Figure 3.1: The mean number of ice days per year in the reference period and the comparison of three time slices to the reference period (the reference period is subtracted). A) Distribution of ice days during the reference period (1961-1990), B) changes during the Maunder Minimum (1661-1690), C) changes in the pre-industrial period (1851-1880), D) changes in the future (2071-2100).

region. For the Maunder Minimum, as well as the pre-industrial period, the model results in a decrease of summer days in the before mentioned areas.

So far, the spatial distribution of two indices for temperature extremes seems to be reasonable. The following paragraph concentrates on generalized extreme value distribution of temperature extremes for a grid point within the Mediterranean, Central Europe and Northern Europe.

Generalized extreme value distribution

The extreme value analysis is conducted on block maxima. For each time slice (30 years during the Maunder Minimum, a pre-industrial period, the present and future) the maximum temperature per month counts as a block maxima using three regions across Europe (Mediterranean, Central Europe and Northern Europe). Figure 3.3, for instance, shows the temperature distribution for the Mediterranean. Central and Northern Europe are not explicitly shown.

A first noticeable similarity among all three regions is the shift towards higher values in the

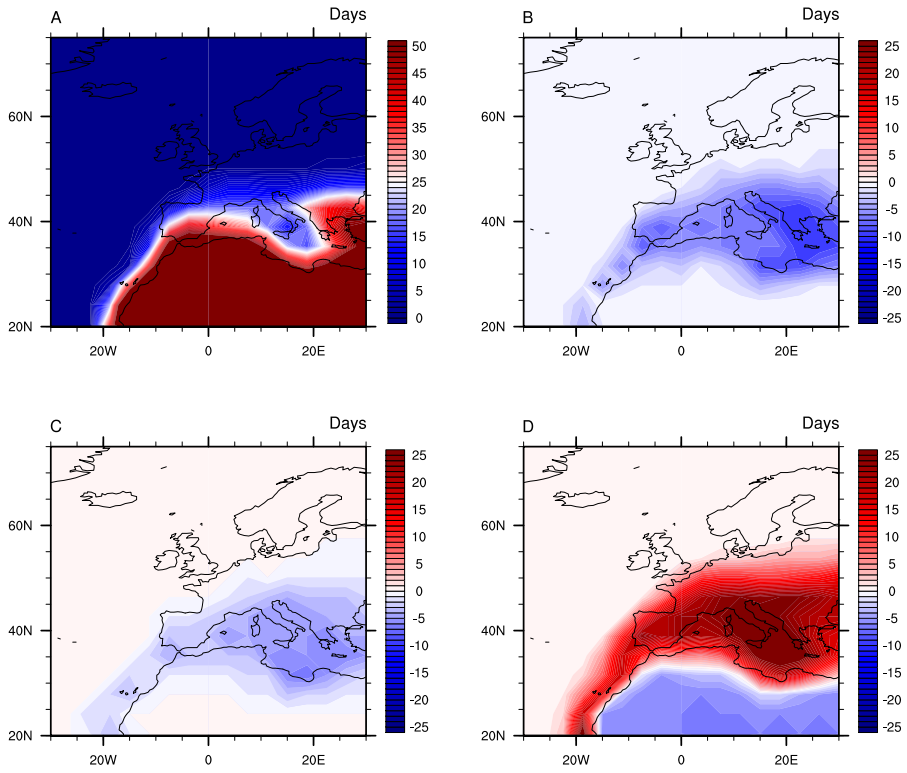

Figure 3.2: The mean number of summer days per year in the reference period and the comparison of three time slices to the reference period (the reference period is subtracted). A) Distribution of summer days during the reference period (1961-1990), B) changes during the Maunder Minimum (1661-1690), C) changes in the pre-industrial period (1851-1880), D) changes in the future (2071-2100).

future. This fact is valid for winter and summer. Among the present and the past periods, no large changes are visible. For the Mediterranean, as well as Central Europe, the Maunder Minimum is denoted as the coldest period, even if the changes compared to the reference period is not very large. For Northern Europe though, the pre-industrial shows a shift in mean towards a cooler climate. But not only changes in mean are play an important role, also changes in shape and scale between regions and seasons have to be considered. As the temperature distribution for the future is flatter over all regions and in winter and summer, the scale appears to change with the mean. The temperature distribution of the Mediterranean (Figure 3.3) reveals a stronger fat-tail behavior for summer months rather than for winter months. This is of interest for the upper tail of the distribution. With enhanced radiation in summer, the mean temperature is higher and therefore more warm extremes occur. This behavior is illustrated in Table 3.1, presenting the extreme value parameters location μ, scale σ and shape ξ for different regions and periods of time, respectively.

The comparison of Table 3.1 reveals the expected shift in location. From the Maunder Minimum to the pre-industrial and reference period, the location parameter rises by about 0.3°C from one period the other for winter temperatures in the winter temperature. From the reference period to the future, the location parameter literally jumps by 2.3°C. This corresponds

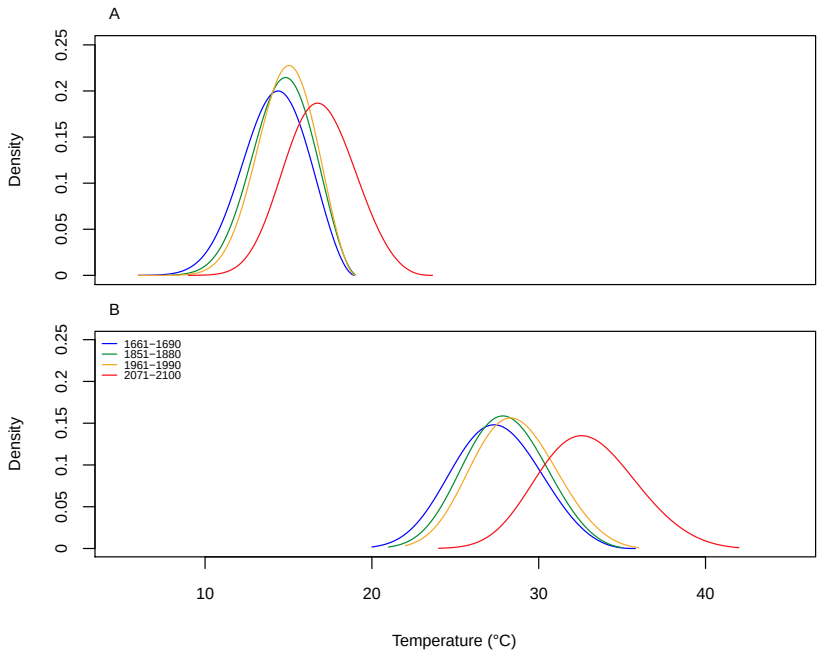

Figure 3.3: Temperature probability density functions for the Mediterranean in different periods of time: A) during winter (DJF) and B) summer (JJA).

to an increase of 23%. Similar is true for Central and Northern Europe. The Maunder Minimum stays the coldest period, followed by the pre-industrial period. The winterly maximum temperature rises by 0.13°C to 0.77°C between the periods. The largest rise occurs between the reference period and the future, by an increase of 3.09°C for Northern Europe and 3.52°C for Central Europe, respectively. For all regions, the scale parameter (σ) undergoes changes between the periods of time. However, the change is less consistent as it is for the location parameter. In the Mediterranean, the maximum variability is found in the future, while the highest variability for Central Europe can be seen in pre-industrial and for Northern Europe in the Maunder Minimum. For the future though, the variability during summer tends to rise (Central and Northern Europe) and shows an increase during winter (Mediterranean and Northern Europe). Considering the shape parameter, all time series of each period and region belong to the Weibull family ($\xi < 0$). This denotes a fatter lower and a lighter upper tail.

The statements made for winter maximum temperature account for the summer maximum temperatures as well. A slow increase in the location parameter (0.59-0.68°C for Mediterranean, 0.35-0.4°C for Central Europe and 0.17-0.26°C for Northern Europe) from the Maunder Minimum to the pre-industrial and reference period is calculated. Again, the largest increase in temperature maximum extremes is estimated from the reference period to the future: Mediterranean by 15%, Central Europe by 20% and Northern Europe by 17%.

For each GEV parameter, standard errors are estimated (see Table 3.2). The standard errors

are slightly higher for summer, but stay in the same range within season and parameter.

Return levels

Based on the block maxima approach, return levels for different return periods are calculated. The results for the Mediterranean are shown in Figure 3.4.

As it already can be supposed based on the temperature probability density functions, warm temperature extremes exhibit a strong rise in the future, for summer and winter. The return levels on a 1000 year return period, for instance, increase more than 4°C compared to the reference period. Figure 3.4 shows similar return levels for the Maunder Minimum, pre-industrial and the reference period. The lowest return levels are calculated for the Maunder Minimum, though. This statement accounts for Northern Europe as well. Only the return levels of Central Europe have its minimum in the pre-industrial period, predominately during winter (not shown). This is remarkable, as the Maunder Minimum is known as a cold period in a solar minimum. Indeed, the return levels of the Maunder Minimum are on a lower level than those of the reference period 1960 till 1990, but still higher than during the pre-industrial period.

In a second step the spatial distribution of the maximal temperature return levels is taken into account. Figures 3.5 and 3.6 depict the return levels over Europe on a 50-year return period. A decline of the return level is visible from south to north. For the summer season the pattern is shifted to the north. The maximum value of around 40°C is calculated over Northern Africa. In summer this value can also be found over parts of the Southern Mediter-

Table 3.1: Extreme value distribution parameters for winter and summer temperatures. One parameter per 30-year time slice and area: Mediterranean, Central Europe and Northern Europe, in °C.

		winter			summer		
		μ	σ	ξ	μ	σ	ξ
1660	Mediterranean	9.33	2.54	-0.41	30.27	2.74	-0.23
	Central Europe	4.14	2.66	-0.39	18.53	3.08	-0.17
	Northern Europe	-3.30	4.74	-0.57	11.54	2.37	-0.08
1850	Mediterranean	9.60	2.35	-0.39	30.86	2.85	-0.32
	Central Europe	4.27	2.81	-0.38	18.93	3.10	-0.19
	Northern Europe	-2.75	4.54	-0.64	11.71	2.29	-0.08
1960	Mediterranean	9.96	2.32	-0.33	31.54	2.84	-0.32
	Central Europe	5.04	2.24	-0.31	19.28	3.14	-0.18
	Northern Europe	-2.40	4.21	-0.46	11.97	2.16	0.03
2070	Mediterranean	12.26	2.66	-0.35	36.25	2.65	-0.26
	Central Europe	8.56	2.28	-0.46	23.11	3.90	-0.31
	Northern Europe	0.69	3.41	-0.53	14.06	2.32	-0.02

Table 3.2: Standard errors of the extreme value analysis for temperature

	μ	σ	ξ
Winter	[0.13, 0.26]	[0.09, 0.19]	[0.02, 0.03]
Summer	[0.13, 0.23]	[0.10, 0.17]	[0.02, 0.05]

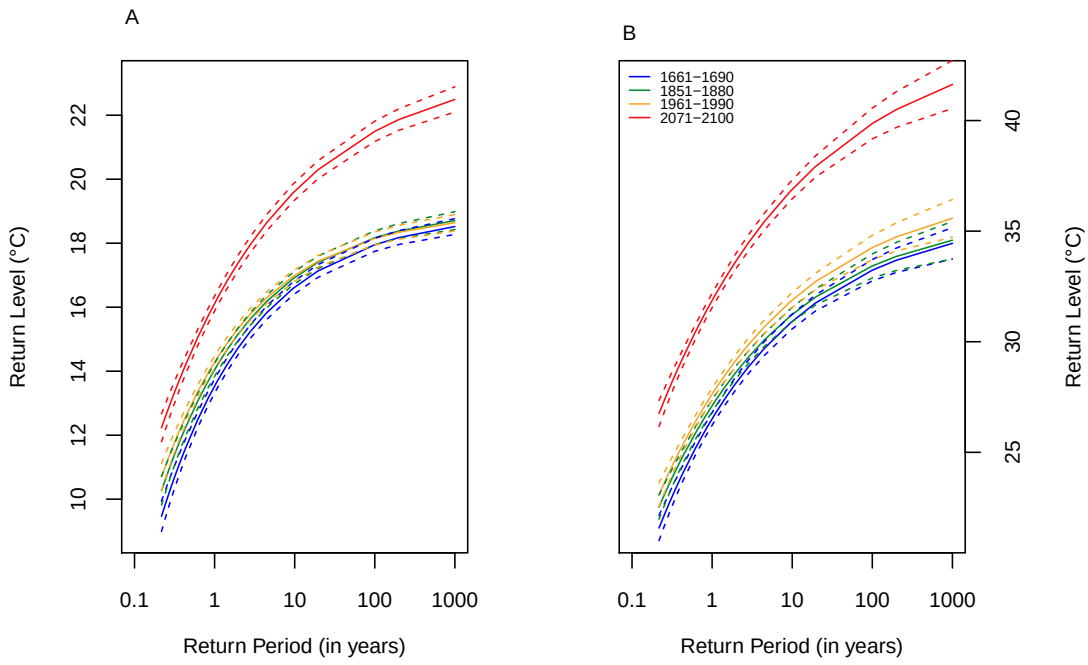

Figure 3.4: Return levels of extreme temperatures for the Mediterranean on different return periods for A) winter and B) summer.

ranean.To be able to see the changes in single periods, differences to the reference period (1961-1990) are calculated (specific period minus reference period).

Most obvious is the general blue shading for the past periods and the red shading for the future period. This means a decrease in return levels for the Maunder Minimum and the pre-industrial period, but an increase in return levels for the future. A more detailed look reveals a stronger change for summer months as for winter months. While there are also some areas that experience a warming in the past years during winter, the spatial cooling during the summer months is more consistent. As it would be expected, the return level differences are even lower for the Maunder Minimum as they are for pre-industrial. This accounts for both, summer and winter. For winter and large parts of Europe, lower return

levels are calculated for the Maunder Minimum and pre-industrial. Largest changes occur in some parts of the Iberian Peninsula and Scandinavia. For both past periods though, some areas also show enhanced return levels. These areas include the Northern most Atlantic and the Benelux states for pre-industrial. For the future only higher return levels are calculated. Highest return level changes can again be found over the Iberian Peninsula, but also over large parts of Central and Eastern Europe. The lowest changes occur over the Atlantic or along the coast. A similar spatial pattern can be found during summer months. The lowest return levels are calculated for the Maunder Minimum over Eastern Europe. However, also for the Mediterranean, Central and Northern Europe one found low return levels during the Maunder Minimum and the pre-industrial period. For the future, the largest rise in return levels can be found over Central Europe and parts of the Mediterranean.

Explicit return levels for the characteristic areas (Mediterranean, Central and Northern Europe) and time periods (Maunder Minimum, pre-industrial, present and future) are listed in Table 3.3 and Table 3.4. The return levels for maximum temperature decrease from south to north in winter and summer. The return levels are largest for the future for all periods. For the winter in the Mediterranean, as well as in Central Europe, the Maunder Minimum is still

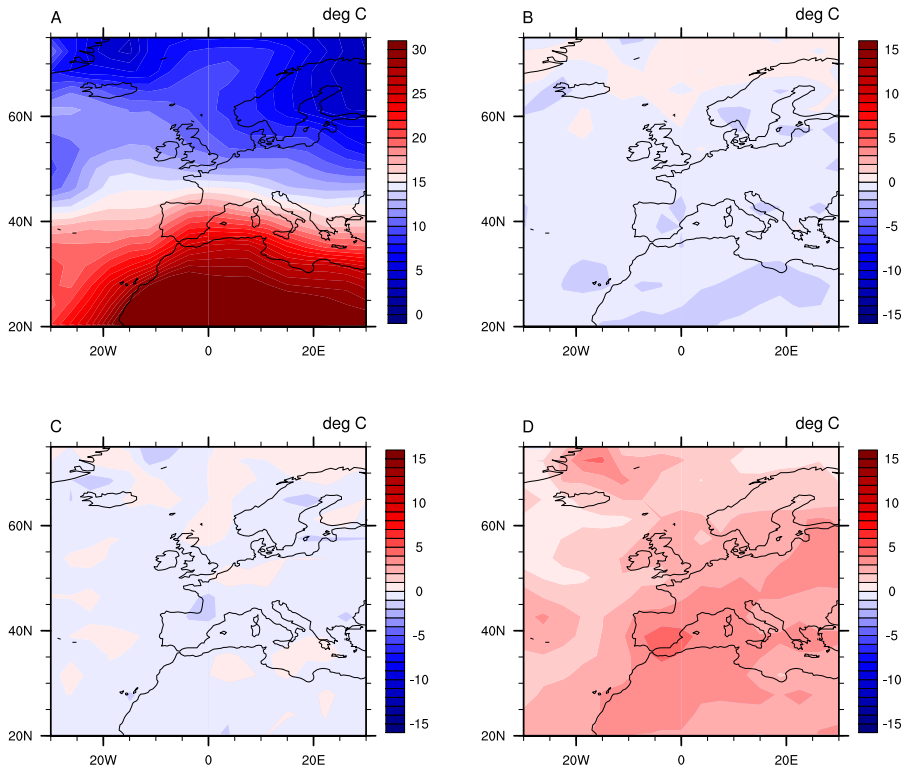

Figure 3.5: European return level map for a 50-year return period of winter maximum temperature: A) return levels during the reference period (1961-1990), B) differences of the Maunder Minimum (1661-1690) to the reference period, C) differences of the pre-industrial period (1851-1880) to the reference period and D) differences of the future (2071-2100) to the reference period. The differences are calculated by subtracting the reference period of the specific period.

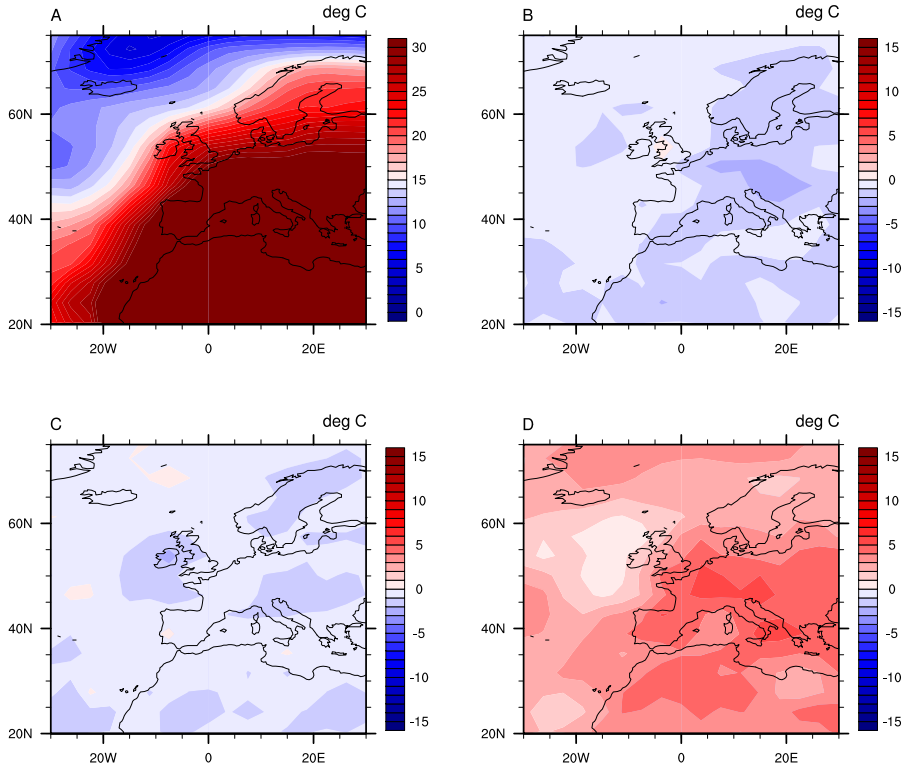

Figure 3.6: European return level map for a 50-year return period of summer maximum temperature: A) return levels during the reference period (1961-1990), B) differences of the Maunder Minimum (1661-1690) to the reference period, C) differences of the pre-industrial period (1851-1880) to the reference period and D) differences of the future (2071-2100) to the reference period. The differences are calculated by subtracting the reference period of the specific period.

the period with the lowest warm temperature extremes. The 50 year return level during the Maunder Minimum is by 0.87°C (Mediterranean) and by 0.75°C (Central Europe) lower than the reference period. This corresponds to a decrease of 5.6% for Mediterranean and 7% for Central Europe. However, more impressive are the strong decreases in winterly return levels for the past over Northern Europe. The model calculates a 50 year temperature return level of 4.53°C during the winter of the Maunder Minimum. Even lower is the 50 year return level for the pre-industrial period, 4.12°C. As the return level for the reference period is 5.81°C, the changes are remarkable: -22% for the Maunder Minimum and -26% for pre-industrial. Compared to the changes over Northern Europe for the past, the changes in the future for all areas seem almost small. The return levels increase by 19% for Mediterranean, 21% for Central Europe and 16% for Northern Europe.

The changes within the 50 year return levels during summer are discussed in the following (compare Table 3.4). The model calculates return levels of 43.66°C for a return period of 50 years over the Mediterranean during summer in the future. This signifies an increase of 5°C (13%) in comparison to the reference period. However, the return levels of the Maunder Minimum and the pre-industrial period during summer are 2.9% and 1.8% lower if compared

to the reference period. For Central Europe the decreases in the summer 50 year return levels, compared to the reference period, during the Maunder Minimum and pre-industrial are larger (4.0% and 4.1%), but smaller for the future (11%). The changes from the earlier periods to the reference period are below 1% for Northern Europe. This area reacts, though, most sensitive in view of the future. The 50 year return level for summer maximum temperatures increase by 17%.

3.1.2 Heatwaves and Cold Spells

A warm/cold spell is defined as period of at least six consecutive days with the maximum/minimum temperature lying above/beyond the 90^{th} percentile, 10^{th} percentile respectively. A warm/cold spells can either be characterized by the number of occurrences per period of time (not shown) or by the maximum duration length (Figure 3.7). The time series of the number of occurrences and maximum duration length proceed in a similar manner, therefore only the time series of the maximum duration length are shown. As the maximum duration length is furthermore a suitable measure for an extreme value analysis, it is chosen as spell characteristics for the subsequent extreme value analysis over the entire period from 1500AD to 2100AD as well. Warm spells are calculated only for summer months (JJA), cold spells only for winter months (DJF).

Figure 3.7 displays the ensemble mean of the number of cold/warm spells. During the Maunder Minimum more winter cold spells are calculated than there are summer warm spells. A similar result can be found regarding the pre-industrial period, most pronounced over Central Europe. While the present shows a transition from a balance between cold and warm spells to a warm spell dominated phase, the future is clearly dominated by summer warm spells. Cold

Table 3.3: Winter temperatures: return levels for characteristic areas (Mediterranean, Central and Northern Europe) and four different return periods in °C.

		10 years	25 years	50 years	100 years
1660	Mediterranean	13.96	14.49	14.73	14.91
	Central Europe	9.10	9.67	9.95	10.17
	Northern Europe	3.84	4.34	4.53	4.71
1850	Mediterranean	14.01	14.48	14.77	14.93
	Central Europe	9.64	10.26	10.57	10.88
	Northern Europe	3.52	3.84	4.00	4.12
1960	Mediterranean	14.67	15.27	15.60	15.86
	Central Europe	9.73	10.37	10.70	11.02
	Northern Europe	4.82	5.46	5.81	6.03
2070	Mediterranean	17.53	18.20	18.57	18.86
	Central Europe	12.47	12.80	12.99	13.13
	Northern Europe	6.11	6.53	6.74	6.85

Table 3.4: Summer temperatures: return levels for characteristic areas (Mediterranean, Central and Northern Europe) and four different return periods in °C.

		10 years	25 years	50 years	100 years
1660	Mediterranean	36.22	37.03	37.48	37.94
	Central Europe	26.28	27.67	28.50	29.34
	Northern Europe	18.60	20.19	21.29	21.99
1850	Mediterranean	36.69	37.51	37.92	38.32
	Central Europe	26.58	27.95	28.47	28.47
	Northern Europe	18.43	19.99	21.09	21.19
1960	Mediterranean	37.39	38.22	38.63	38.96
	Central Europe	27.28	28.73	29.69	30.42
	Northern Europe	19.61	21.82	21.30	22.30
2070	Mediterranean	42.23	43.16	43.66	44.16
	Central Europe	31.32	32.44	32.99	33.55
	Northern Europe	21.62	23.53	25.08	26.52

spells are nearly not detected for all regions in 2100AD. As expected, the Maunder Minimum is the coldest period of time. Compared to other periods, the number and the maximum duration during the Maunder Minimum are higher for winter cold spells and lower for summer warm spells. Over Central Europe the largest number and the longest duration of cold spells are calculated, predominately during the Maunder Minimum and the pre-industrial period. Most sensitive on heat waves, on the other hand, seem to be the Mediterranean.

An extreme value analysis for 30 year time slices was conducted for warm and cold spells on maximum duration length. The main results of the analysis, the development of the extreme value distribution parameters, are shown in Figure 3.8 and Figure 3.9. As expected, the location parameter follows the changes in the duration length. For warm spells, most obvious changes can be detected towards the end of the time series, where a sharp rise in the maximum duration length can be seen. In the period before 1990AD, the location parameter stays more or less constant on a value between 2 and 4 days of warm spell duration. The scale parameter follows the pattern of the location parameter. In periods of longer warm spells, the warm spell duration distribution is wider, denoting a rise in the variability of warm spells occurrence as well. The shape parameter stays constant at a value close to zero for the entire time series. The extreme value distribution of the maximum warm spell duration can be assumed as Gumbel distributed. These observations of changes in extreme value distribution parameters hold true for the Mediterranean, as well as for Central and Northern Europe. The alterations are most clearly seen in the Mediterranean.

In the case of cold spells, the extreme value distribution parameters behave slightly different (Figure 3.9). The location parameter still follows the mean of the maximum cold spell duration distribution. The maximum cold spell duration stays more or less constant on a high level before 1990AD, compared to the reference period, the variations are larger though. There is

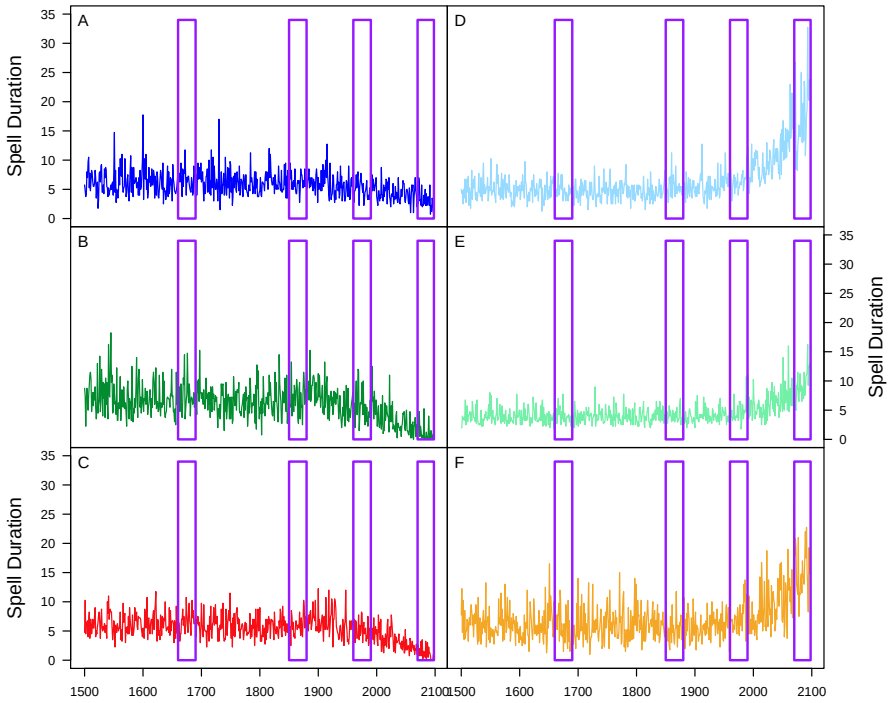

Figure 3.7: Time series of maximum cold and warm spell duration in days: A) winter cold spell duration in the Mediterranean, B) winter cold spell duration in Central Europe, C) winter cold spell duration in Northern Europe, D) summer warm spell duration in the Mediterranean, E) summer warm spell duration in Central Europe and F) summer warm spell duration in Northern Europe. The purple boxes denote the Maunder Minimum (1661-1690), the pre-industrial period (1851-1880), the present (1961-1990) and the future (2071-2100).

a slight decline in duration length visible between 1700 and 1850AD and a rise in the period around 1900AD for all regions. Finally, the maximum cold spell duration length continuously falls close to zero towards 2100AD. The changes in cold spell duration are most pronounced for Central Europe. As found for warm spells as well, the scale parameter follows the pattern of the development of the mean. The shape parameter lies close to zero for all regions over the entire period of time. Only one exception can be detected: as the location parameter of Central Europe falls to zero at the end of the time series, the shape parameter rises sharply to a value close to 8. As a sudden large change in shape seems suspect and as it is known that the GEV model does not respond well on values close to zero, it is possible that the GEV model is not suited for this situation.

Extremes in warm and cold spell durations are further examined using return levels on the 50 year return period. In Table 3.5 the return levels for the Mediterranean, Central and Northern Europe during the Maunder Minimum, pre-industrial, present and future are listed. Comparing only these four periods of time, the Maunder Minimum results in having the longest cold spells in the Mediterranean (16.5 days) and Northern Europe (14.6 days). In

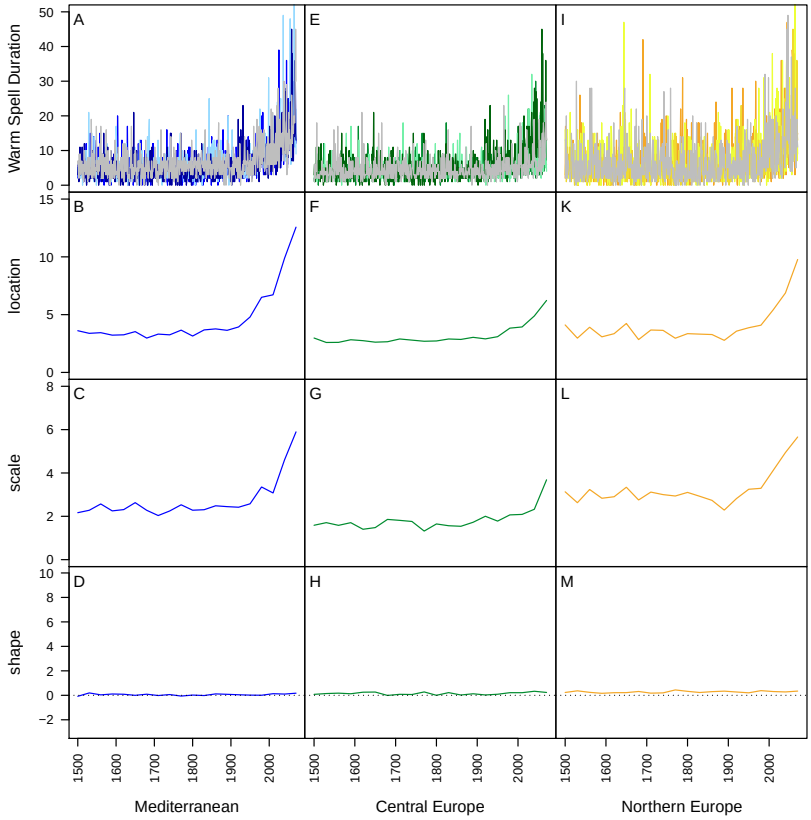

Figure 3.8: Extreme value analysis on warm spells. First line shows the maximum duration time series, for every transient run in a different color. Row two to four depict the development of the extreme value distribution parameters location, scale and shape in 30-year windows: A) to D) for the Mediterranean, E) to H) for Central Europe and I) to M) for Northern Europe.

Central Europe though, even longer cold spells are found for the pre-industrial period (24.7 days compared to 21.4 days during the Maunder Minimum). Based on the problems of the GEV model, no statements can be drawn for the future for Central and Northern Europe. In the Mediterranean, the model is still able to calculate a 50 year return level, which is close to zero, though (1.4 days).

If the four periods are analyzed concerning warm spell duration, the pre-industrial period turns out to be the coldest period for Central (9.7 days) and Northern Europe (19.2 days). For the Mediterranean, the Maunder Minimum still accounts for the period with the lowest 50 year return level (11.9 days) and is thus the coldest period. In the future, the return levels experience a sharp rise towards long warm spells, especially for Northern Europe, which results in a 50 year return level of a 56 day long heat wave. Also in the Mediterranean and Central Europe, the occurrence of long heat waves (45.1 days and 29.7 days) will not be occasionally.

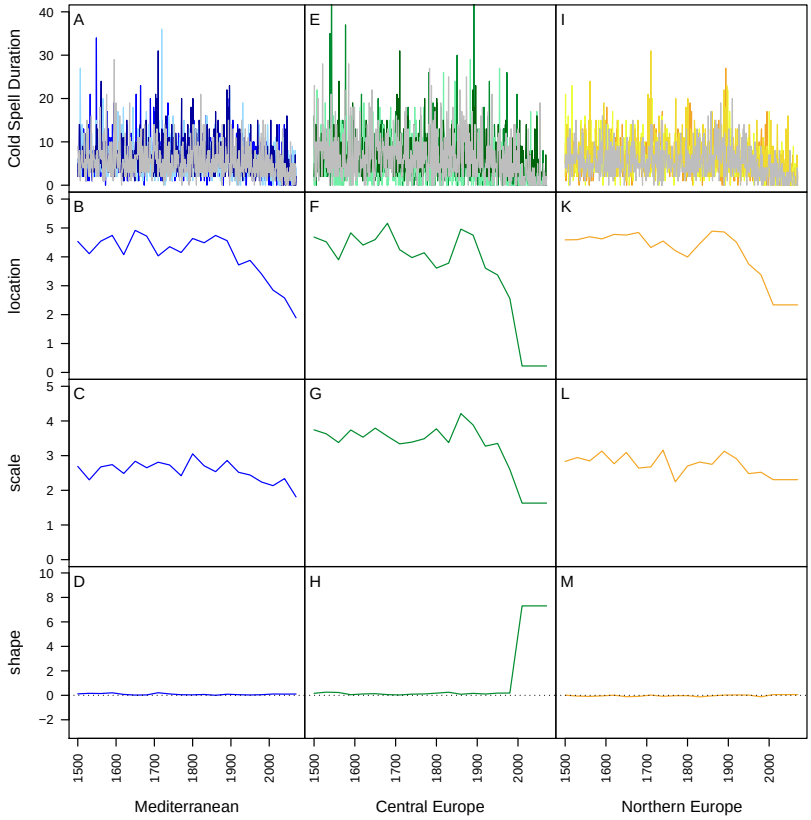

Figure 3.9: Extreme value analysis on cold spells. First line shows the maximum duration time series, for every transient run in a different color. Row two to four depict the development of the extreme value distribution parameters location, scale and shape in 30-year windows: A) to D) for the Mediterranean, E) to H) for Central Europe and I) to M) for Northern Europe.

Figure 3.10 shows the development of the 50 year return level from 1500 to 2100AD. It resembles the statements done for Table 3.5. During the Maunder Minimum and the pre-industrial period, the Mediterranean and Northern Europe show longer cold spells. While there is a decline in cold spell duration in Central Europe during the Maunder Minimum, there can be seen a increase before 1900AD as well. The warm spell duration return level stays constant before 1900AD for the Mediterranean and Central Europe, after it starts rising and reaches its maximum at 2100AD. For Northern Europe, the maximum 50 year return level is reached also at 2100AD, but there is a second pronounced increase between 1750AD and 1800AD.

3.1.3 Underlying Dynamics

Cold and warm spells are a consequence of atmospheric blocking [*Häkkinen et al.*, 2011]. According to *Rex* [1950], atmospheric blocking is characterized by a breakdown of the westerly

Table 3.5: 50-year return levels for warm and cold spells and different periods of time. The return levels are represented in maximum duration length (days).

		1661-1690	1851-1880	1961-1990	2071-2100
Cold Spells	Mediterranean	16.5 ±1.4	15.2 ±1.4	12.6 ±1.1	10.6 ±1.4
	Central Europe	21.4 ±2.1	24.7 ±3.7	20.4 ±3.0	0
	Northern Europe	14.6 ±1.0	14.2 ±1.1	13.2 ±1.2	0
Warm Spells	Mediterranean	11.9 ±1.0	15.0 ±1.6	14.0 ±1.0	45.1 ±5.6
	Central Europe	11.2 ±1.2	9.7 ±0.8	13.5 ±1.8	29.7 ±5.3
	Northern Europe	21.5 ±3.5	19.2 ±3.0	27.4 ±5.5	56.1 ±10.6

flow. This implies a persistent pressure pattern that lasts for several days [*Buehler et al.*, 2011], which traps air masses. There are several types of blockings. Commonly, high-pressure causes blocking situations, as high pressure covers a large area and moves slower. Also low pressure can be in connection with blockings. Further information about blocking types can be found on http://www.theweatherprediction.com/blocking/. As blocking situations are predominately seen in on higher levels, the dynamical analysis is performed on the 500 hPa level. Depending on the area where a cold or warm spell occurs, the underlying dynamics differ. In order to examine the dynamics which are responsible for extraordinary long cold or warm periods, the pressure pattern during the five most severe spells are analyzed. The pressure pattern is examined as geopotential height on 500 hPa. To detect the anomaly in the geopotential height on 500 hPa during cold or warm spells, the seasonal mean of the according 30-year period is subtracted.

Figure 3.11 and Figure 3.12 give the characteristic of geopotential height anomaly during cold spells and warm spells, respectively. To perform the calculation, the five longest cold/warm spells per simulation are selected, thus twenty most severe cold spells are analyzed. For each cold/warm spell a geopotential height anomaly field on 500 hPa is calculated by averaging the geopotential height pattern during the spell and subtracting the mean geopotential height pattern during the associated 30 year period. The geopotential height anomaly of Figure 3.11 and Figure 3.12 is the mean of the geopotential height anomaly fields for each cold/warm spell. To avoid the problem of seasonality, cold spells are only analyzed in winter and warm spells only in summer.

Cold spells over the Mediterranean (Figure 3.11 A) occur, if the pressure over large parts of Western and Northern Europe is anomalously high. Over the eastern Mediterranean Sea towards Asia the pressure is extraordinary low during these periods. Cold continental air is transported toward the Mediterranean during a cold spell. During cold spells in Central Europe the high pressure is shifted to the Atlantic Ocean and Greenland. Low pressure is located over Eastern and Central Europe. Cold air of continental northeastern Europe can therefore flow to Central Europe. A similar picture can be found for Northern Europe. Though, the high pressure ridge is moved more over Greenland and the low pressure more northward. The cold air flow originates therefore from polar regions. If the high pressure areas are stable for several days, the cold air advection is continued and the regions (the Mediterranean, Central

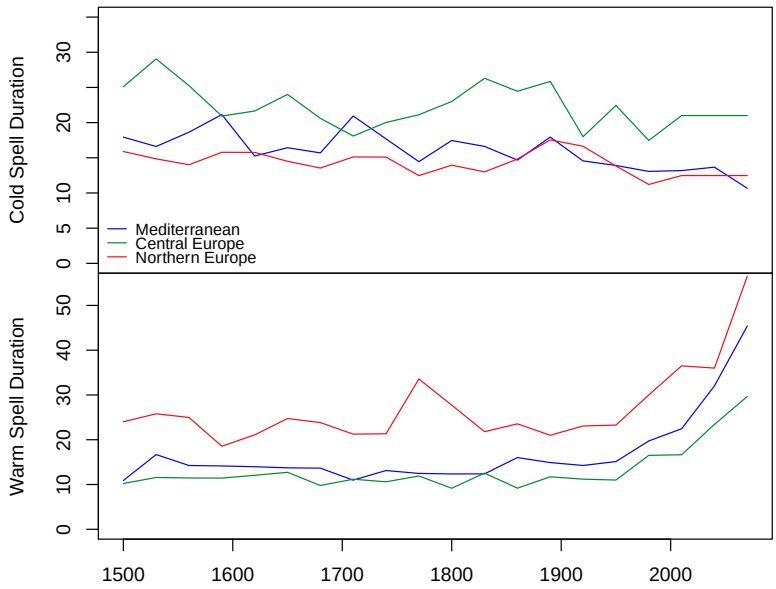

Figure 3.10: Time series of return levels on the 50 year return period for all regions for warm and cold spells using a 30-year window.

and Northern Europe) experience cold spells on longer duration.

Other studies based on the analysis of the anomaly field on 500 hPa [*Sausen et al.*, 1995; *Sillmann and Croci-Maspoli*, 2009; *Buehler et al.*, 2011 and [*Häkkinen et al.*, 2011]] found a blocking maximum over the Atlantic and southeast of Greenland, always dominated by high pressure. Low pressure to a larger or smaller extent is also found over continental Europe, which support the calculations of the CCSM3 model.

Warm spells are mainly induced through stable high pressure systems. As for cold spells, the warm air is advected from continental areas and not from the Atlantic ocean. Low pressure systems play a negligible role for heat waves. For warm spells, the dominating high pressure is located over Eastern Europe and the Balkans. Warm air flows from north Africa and east Mediterranean towards the Mediterranean area. For Central Europe the according high pressure is located more in the north, over parts of the Scandinavian countries and the British Isles. Warm air is advected from the Southeastern European continent and Asia to Central Europe. Heat waves in Northern Europe are induced by warm air from Southeastern Europe and Asia as well. The high pressure is shifted towards north Scandinavia and the Barents Sea. Blocking high pressure seems to be the main driver of heat waves all over Europe. High pressure on higher levels in the atmosphere produces subsidence which leads to warm-air advection, clear skies and hot conditions [*Meehl and Tebaldi*, 2004].

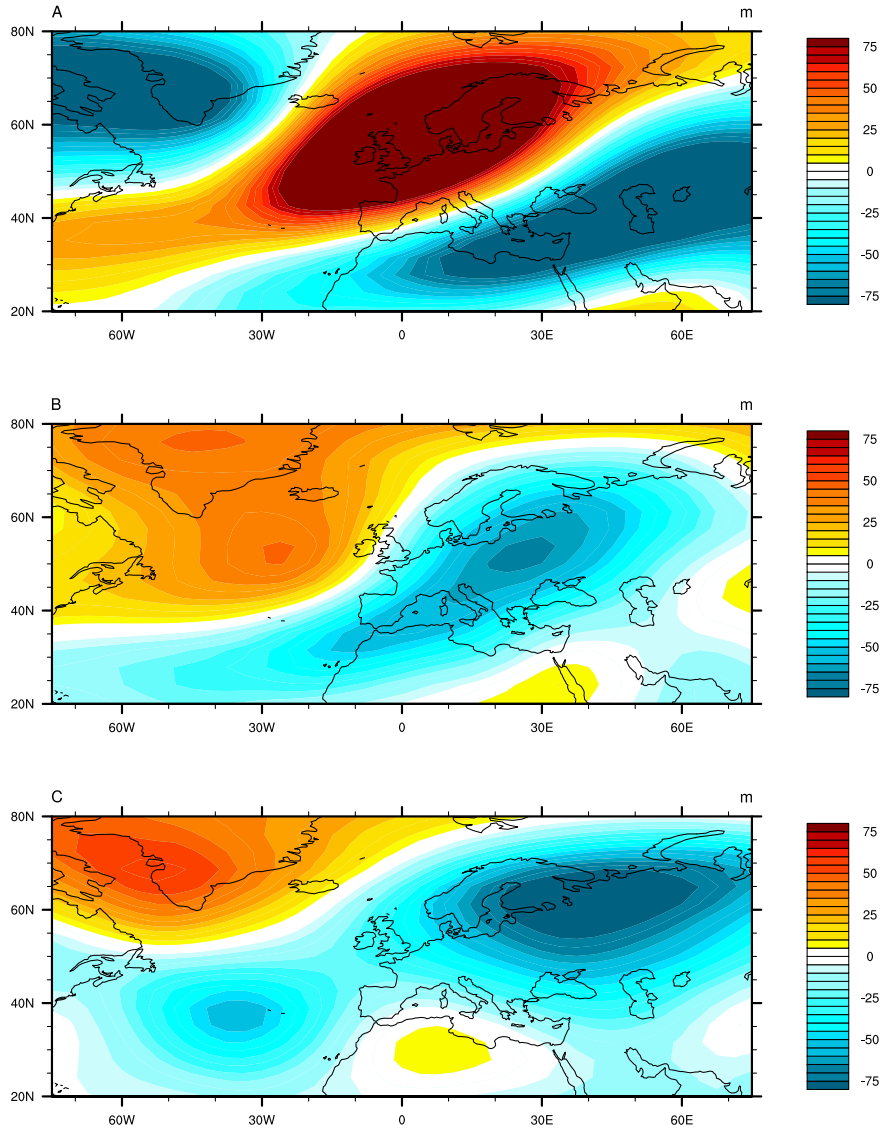

Figure 3.11: Atmospheric dynamics during cold spells. Geopotential height anomaly on 500 hPa for cold spells in A) the Mediterranean, B) Central Europe and C) Northern Europe.

Pelly and Hoskins [2003] investigated blocking situations. Even though they analyzed the 250 hPa pressure level, they found a comparable pattern in geopotential height during summer months. Similar results are calculated by *Meehl and Tebaldi* [2004]. For the summer heat wave of 2003 over Central Europe, they calculated an anomaly in geopotential height on the 500 hPa level of over 120 geopotential meters. As the 2003 heat wave was severe, it can be compared to the heat waves (warm spells) taken into account to calculate Figure 3.12. They further state, that heat waves are generally associated with positive geopotential height anomalies on the 500 hPa level, which further supports the findings in Figure 3.12.

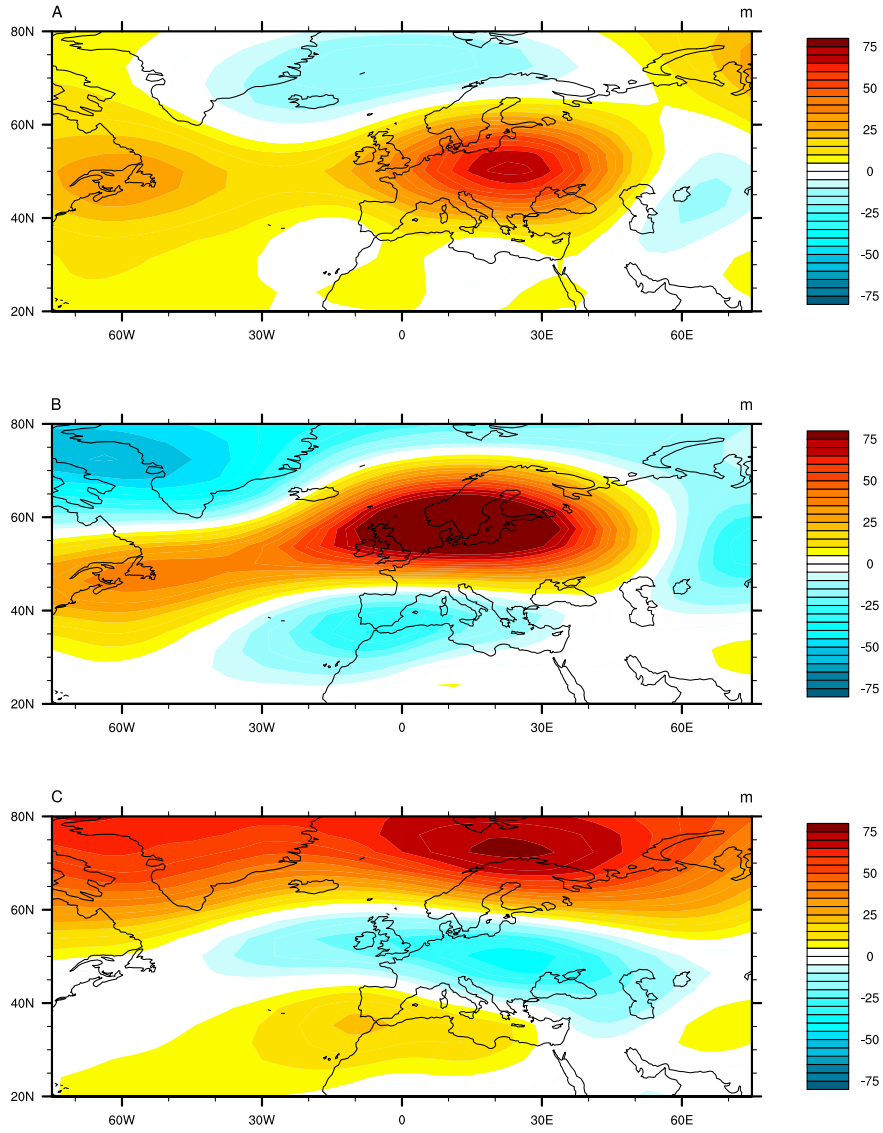

Figure 3.12: Atmospheric dynamics during warm spells. Geopotential height anomaly on 500 hPa for warm spells in A) the Mediterranean, B) Central Europe and C) Northern Europe.

3.1.4 Discussion

Model evaluation

Winter and summer surface temperature of the CCSM3 model is evaluated using the ERA-40 temperature (Figure 3.13 and 3.14) for the period 1961-1990. Seasons (DJF and JJA) are analyzed separately. Figure 3.13 and 3.14 compare the spatial distribution of mean surface temperature and standard deviation. In order to be able to compare both data sets on the same spatial grid, the ERA-40 data is interpolated from 2.5°× 2.5° to 3.75°× 3.75° in longitude and latitude.

The winter mean temperature over continental Europe during the period 1961-1990 of the CCSM3 climate model corresponds well to the mean temperature of the ERA-40 observational data set (Figure 3.13). Over Northern Europe the modeled temperatures are considerably too low. The differences of the model to the observational data ranges between 10 and 20°C. Though, the winter temperatures over Northern Atlantic are 5 to 10°C too large. The temperature distribution during the summer months is slightly different. Large parts of Northern and Central Europe, as well as of the Mediterranean are simulated to be too cold. The differences model to observational data range between -5°C and -15°C. The area over Spain and along the Adriatic coast are represented well by the model.

The largest standard deviation for the climate simulation and the reference data is found over Northern Europe and Northern Atlantic (Figure 3.14). Standard deviations over Northern Europe in the climate model are considerably larger though. In fact, if one considers the standard deviation differences for winter (Figure 3.14 C), the temperature standard deviation over Northern Europe is 2 to 5°C too large. Over the Mediterranean and Central Europe, the standard deviations are substantially smaller. The spatial distribution of the values of the model and the observational data resemble each other. The differences between the model and the observations lie close to zero or slightly below zero (north Spain and west France). During summer, the temperature standard deviation are overall smaller. Temperature standard deviations over Northern Europe between model and observation are in the same range, over the Mediterranean and Central Europe are enhanced by 1 to 2 degrees.

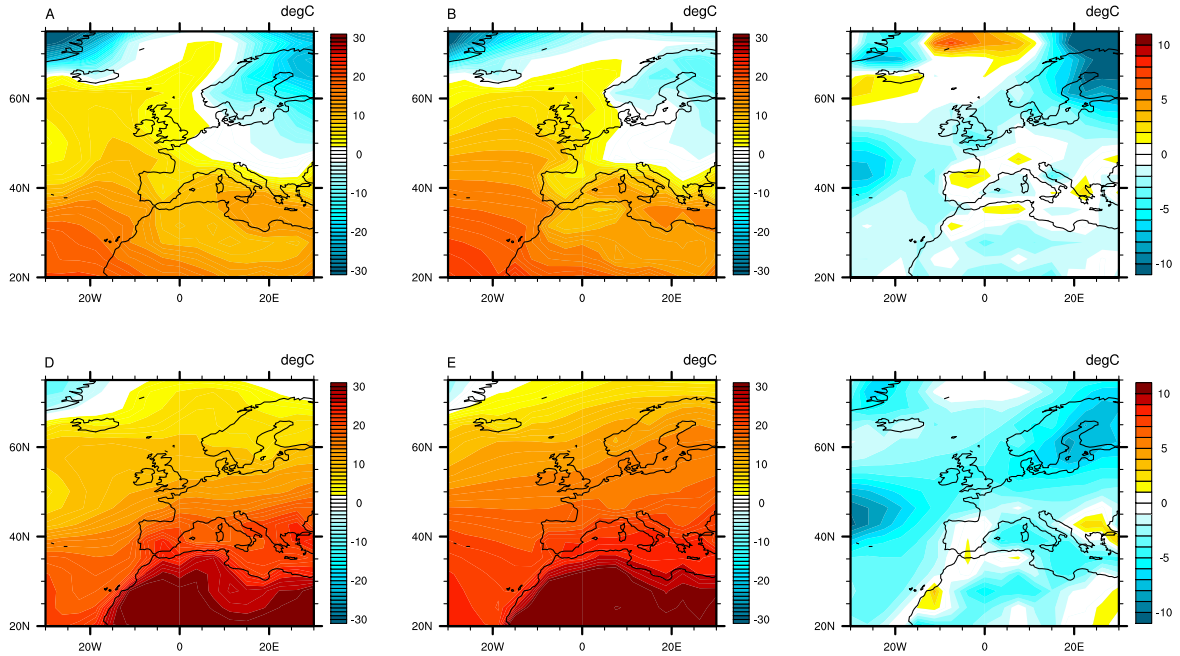

Figure 3.13: Model evaluation for mean temperature: A) DJF of the CCSM3 model, B) DJF of ERA-40 data, C) Differences of model and data; D) JJA for the CCSM3 model, E) JJA of the ERA-40 data, F) Differences of model and data.

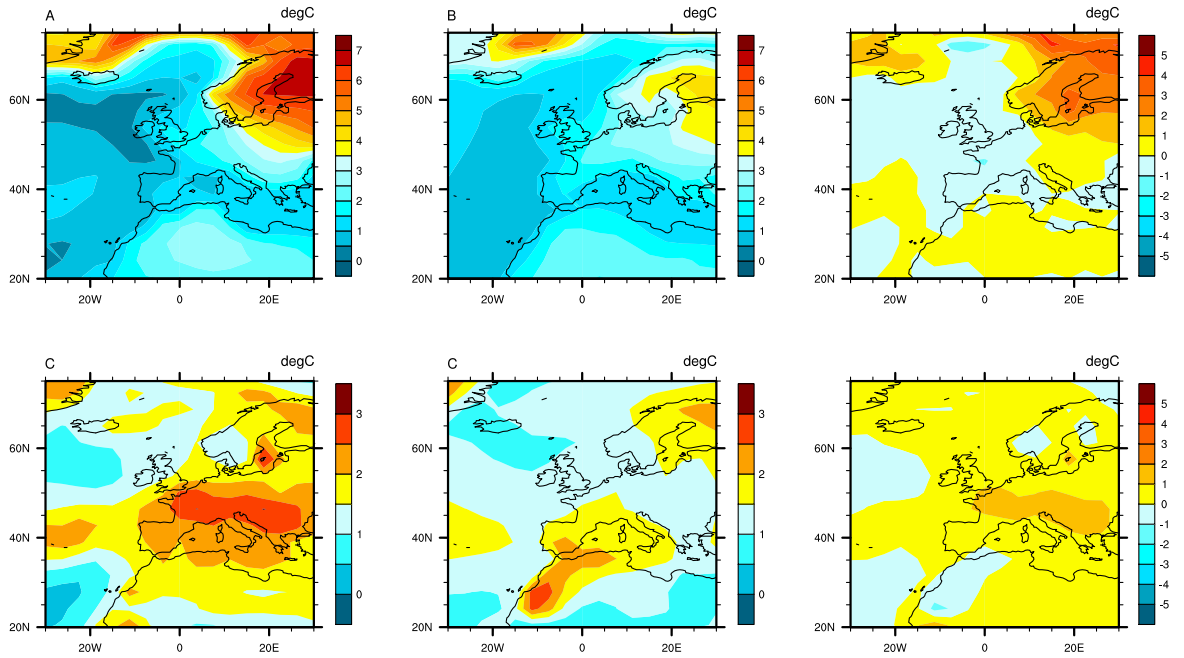

Figure 3.14: Model evaluation for standard deviation of temperature: A) DJF of the CCSM3 model, B) DJF of ERA-40 data, C) Differences of model and data; D) JJA for the CCSM3 model, E) JJA of the ERA-40 data, F) Differences of model and data.

Summarized, the simulated mean temperature is slightly smaller than the mean of the observed data during the reference period 1961-1990. During winter, Northern Europe shows higher standard deviations in the simulations than in the observations. In summer, enhanced values can be detected over Central Europe.

Changes in extreme climate

The current chapter investigates in the behavior of temperature extreme values in the CCSM3 model simulations from 1500 - 2100AD. Once, structural changes in the extreme value distribution of the maximum temperature (DJF and JJA), as well as of cold and warm spells are found. Cold spells are solely examined for winter months (DJF), warm spells only for summer months (JJA). In a second step, return levels for maximum temperatures and warm/cold spells on a return period of 10, 25, 50 and 100 years are calculated.

As the analysis of the past is mostly conducted on measurement and reconstructed data, the results of the extreme value analysis is therefore discussed on the basis of measurement data. *Xoplaki et al.* [2005] examined changes in temperature variability and extremes over the last 500 years, based on reconstructed and observed data over Europe. Even though they calculated extremes of spring and fall and not exactly of summer and winter (as it is done here), the overall trends can be compared. They found a clear low in return levels around 1660, which is interpreted as the Maunder Minimum. Further they show an increase in return levels around 1800, but a decrease around 1850. The level of 1850 is slightly enhanced compared

to the Maunder Minimum. After 1990 the return levels calculated by *Xoplaki et al.* [2005] increase. These findings support the results of the extreme value analysis of the CCSM3 model. The lowest return levels for the Mediterranean and Central Europe in winter and summer are found during the Maunder Minimum. For the 50 year return period, the Central Europe shows a return level in the Maunder Minimum of 9.95°C in winter and of 28.5°C in summer. As the pre-industrial period is chosen between 1851-1880 it corresponds well to the findings of *Xoplaki et al.* [2005]: the return levels are slightly enhanced (10.57°C in winter and 28.47°C in summer for Central Europe). The values are even higher for the reference period 1961-1990: 10.70°C in winter and 29.69°C in summer for Central Europe. Similar results are calculated for the Mediterranean and Northern Europe. For Northern Europe though, the return levels are smaller during the pre-industrial period than in the Maunder Minimum. Indeed, if compared to the tree-ring reconstruction of *Gunnarson and Linderholm* [2002], the mean climate over Scandinavia used to be warmer in the late 17th century, than it was in the late 19th century.

For the future, the analysis reveals an overall increase in warm extremes for all seasons. Already quite a lot of climate models are analyzed to estimate the changes in extremes in the future [*Räisänen*, 2000; *Beniston and Diaz*, 2004; *Schär et al.*, 2004; *Giorgi and Bi*, 2005; *Scherrer et al.*, 2005 and others] leading to a similar result: a positive shift in the distribution of daily minimum and maximum temperatures throughout the globe [*Alexander et al.*, 2006].

The ensemble mean of the future warm extremes during summer rises about 2-4°C in Central and Northern Europe and more than 4°C in the Mediterranean. In winter, the ensemble mean increases 2-4°C over all three grid points. These findings are supported by *Nikulin et al.* [2011]. They examined a regional climate model (0.44°horizontal resolution) on extremes in the current (1961-1990) and the future (2071-2100) climate. Using the same analysis technique as it is used here, they found similar results. They exhibit an intensification of warm extremes by 2-4°C over Northern Europe and 4-6°C in Southern Europe, which corresponds to the results in in Table 3.1. The findings of the summer extremes are further supported by the simulations of *Beniston and Diaz* [2004] who found a shift of extreme temperatures from 28-34°C (1961-1990) to 32-40°C (2071-2100), which corresponds to an increase of 4-6°C over Switzerland. These values are even higher than those found in this study. *Nikulin et al.* [2011] and others, such as *Kharin and Zwiers* [2005], used return levels to estimate the behavior of extreme events. Both show an increase in temperature extremes, which goes along with the growth of the return levels found here: 11-17% for summer temperature extremes and 16-21% for winter temperature extremes. The most pronounced changes in extreme temperatures in the future occur over Central Europe. This statement can also be supported by *Schär et al.* [2004], who found a similar pattern.

The visual analysis of the temperature distribution (Figure 3.3 of a grid point in the Mediterranean) revealed not only changes in mean, but also in standard deviation. In particular, the future scenario run (2071-2100) experiences a shift towards higher extremes, which is accompanied by flattening of the curve. This flattening denotes an enhanced variability. *Schär et al.* [2004] ran a regional climate model to detect the role of increasing temperature variability in European summer heatwaves. The main findings of *Schär et al.* [2004] reflect the findings of the present thesis. The distribution of the scenario simulation exhibits on the one hand a shift to warmer temperatures and on the other hand an increase in standard deviation.

Large increases in the frequency of extremes in the future are therefore not only a matter of higher mean temperatures, but also a consequence of a widening of the distribution. If the scale values σ of Table 3.1 for winter and summer are compared, it can be concluded that the changes in variability of the future, is only valid for Central and Northern European summer. This assumption is confirmed by *Räisänen* [2000], *Giorgi and Bi* [2005], *Scherrer et al.* [2005] and *Fischer and Schär* [2009]. They all calculated variability increases for the summer and even variability decreases for the winter. The calculation is though performed on mean temperature series and not extreme events, as it is done in the current thesis. *Fischer and Schär* [2009] suggest an increasing risk of summer temperature extremes with rising mean temperatures, as the inter-annual, seasonal and inter-seasonal variability increases.

If temperatures are anomalously high/low over a long period (in this case six days), a warm or cold spell is formed. Warm spells (also called heat waves) and cold spells have severe impacts on human [*Huynen et al.*, 2001; *Díaz et al.*, 2005; *Tan et al.*, 2007] and nature. Heat waves associated to warm nights and a high relative humidity, with no relief of the heat for a long time, badger especially elderly and weak people. Cold spells, on the other hand, affect human and nature through very low temperatures. Changes in frequency and severity of warm and cold spells are therefore analyzed.

The Maunder Minimum is widely known as a relatively cold and dry period. During the winter months of the Maunder Minimum, the flow was occasionally blocked, which led to southward outbreaks of cold, continental air [*Wanner et al.*, 1995]. As discussed by *Buehler et al.* [2011], cold spells are induced by such blocking situations. In the actual thesis, cold spells are compared on the basis of return levels. During the Maunder Minimum, the maximum duration of a cold spell for a return period of 50 year, is calculated to be 16.5 days in the Mediterranean, 21.4 days in Central Europe and 14.6 days in Northern Europe. As the cold spells are calculated as consecutive days with temperatures below the 10^{th} percentile of the local temperature distribution, the results are directly comparable to the findings of *Buehler et al.* [2011]. Primarily, the return levels for Central Europe closely agree to *Buehler et al.* [2011]. It is interesting though, that only cold spells over the Mediterranean and Northern Europe find their maximum duration in the cold period of the Maunder Minimum. For Central Europe, cold spells are even longer in pre-industrial period. Despite the cool average temperatures during the Maunder Minimum, warm periods occur as well. The model calculates even longer warm spells during the Maunder Minimum than for the pre-industrial period for Central and Northern Europe. Not much is known about warm spells during the Maunder Minimum. It seems though, that the circulation pattern described by *Wanner et al.* [1995] - high pressure over Northern Europe, the British Isles and Northern Atlantic - is not only accountable for cold spells, but also for warm spells. If compared to the reference period of 1961-1990, the 50 year warm spell are shorter. This can be explained by the overall cooler mean climate during the pre-industrial period, combined with a lower blocking frequency [*Rimbu and Lohmann*, 2009].

After the striking heat wave of 2003, the topic on warm spells and its development in the future is frequently examined. In the CCSM3 model the duration of future heat waves are calculated to rise more than 300% of the duration in the reference period for the Mediterranean. Also for Northern and Central Europe warm spells are possibly 200% longer. *Fischer*

and Schär [2010] analyze the changes in heat wave characteristics for the future (2071-2100) compared to the control period (1961-1990). They found an increase in heat wave frequency, as well as intensity. As can be seen in Figure 3.7, these results account for the findings of this thesis as well. The pressure pattern responsible for severe heat waves resemble the pattern found by *Meehl and Tebaldi* [2004]. Note, however, that heat waves are not only triggered by blocking patterns [*Fischer and Schär*, 2010]. *Fischer and Schär* [2010] propose a combined effect of atmospheric circulation and soil moisture. Therefore heat wave occur preferably in late summer [*Fischer and Schär*, 2009].

3.2 Precipitation

3.2.1 Extreme Climate

Climate indices

A first impression of precipitation extreme values is received by considering the number of dry days, as well as the sum of extreme precipitation. Each period is analyzed separately for the winter (DJF) and summer (JJA) season. The behavior of droughts (the lower tail of the precipitation distribution) is estimated by the analysis of the mean dry days in 30 years. The upper end of the precipitation distribution (wetnesses) is evaluated using the sum of precipitation on heavy precipitation days. A heavy precipitation day is considered as a day with a precipitation amount higher than the 95^{th} percentile of the reference period. In contrast to the temperature climate indices, the two precipitation indices are calculated for both seasons, DJF as well as JJA.

The dry day distribution during summer and winter differs strongly (Figure 3.15 and Figure 3.16). A larger number of dry days is found for summer, as for winter. Furthermore, large parts to the Atlantic and continental Europe experience more wet days during winter than during summer. For both seasons though, the Northern British Isles, as well as Southern Scandinavia are rather wet areas. Not surprisingly, the driest area for both seasons can be found over Southern Mediterranean as well as Northern Africa.

Considering the differences to the reference period (Figure 3.15 and Figure 3.16, base period minus reference period), one can detect some constant regions of change, which are valid throughout all time slices, with different signs and severity. During the winter season, most pronounced changes occur over Southern Europe, Northern Europe and Northern Atlantic. Central Europe stays more or less stable. For past time slices, Southern Europe as well as the Northern Atlantic experience less dry days, where there are more dry days in future. On the other hand, there are more dry days over Northern Europe in the past. Furthermore the changes in the future are more severe than they are in the past.

During summer, the areas of distinct changes in comparison to the reference period, are slightly different to those during winter (Figure 3.16). Most obvious is the decrease of dry days in the past over Central Europe, where there is a severe increase in dry days in the future. Again, the severity of changes in the future is larger than in the past.

To estimate the behavior of the upper end of the precipitation distribution, the amount of precipitation on heavy precipitation days is chosen as a measure. Equal to the distribution of dry days, the summer season has a smaller amount of heavy precipitation as the winter season (Figure 3.17 and Figure 3.18). For both, summer and winter, the area of the largest amount of heavy precipitation can be found over the Atlantic, in the west of the British Isles and Ireland. During winter, the area of extreme precipitation is extended and reaches down to the coast of France and Spain. The distribution pattern within the winter season stays similar for different time slices. Considering the differences to the reference period for the past time slices, a decrease in heavy precipitation over Northern Europe and the British Isles is detectable. A slightly increased heavy precipitation amount is indicated over the Mediter-

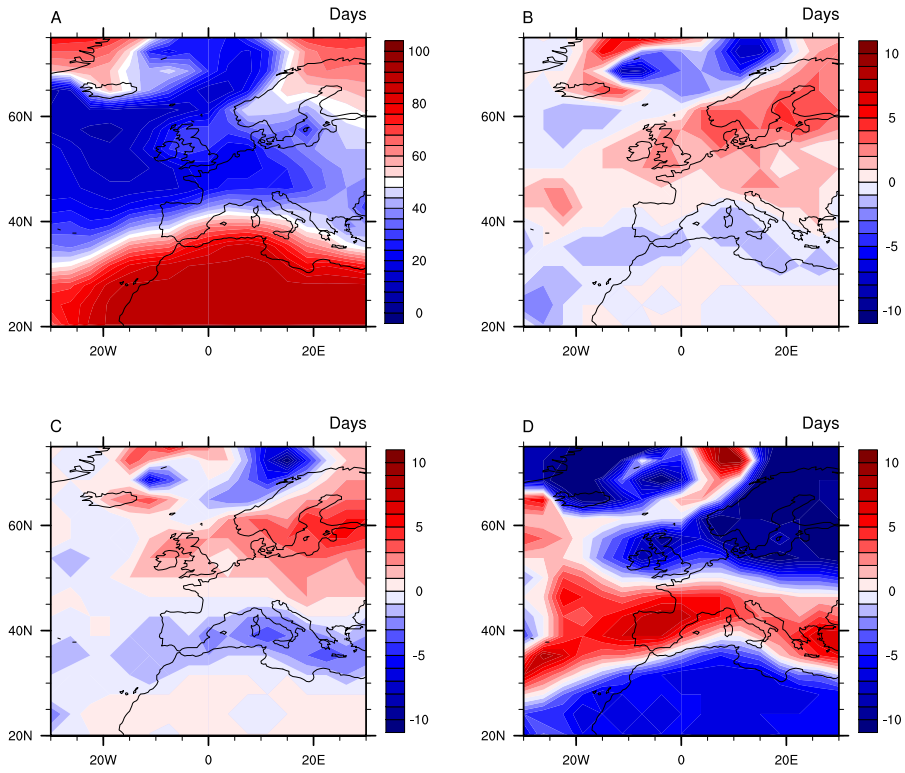

Figure 3.15: The mean number of dry days per winter for the reference period and the comparison of three time slices to the reference period: A) Distribution of dry days during the reference period (1961-1990), B) changes during the Maunder Minimum (1661 - 1690), C) changes in the pre-industrial period (1851 - 1880) and C) changes in the future (2071 - 2100).

ranean. For the future, the changes are present in similar regions with different signs. For a band over parts of Central Europe, the Mediterranean and the Atlantic, heavy precipitation amounts decrease drastically. Over Northern Europe and the British Isles a strong increase in heavy precipitation is detectable.

The regions of change in summer are comparable to those during winter (Figure 3.18). In summer though, the areas of change experience not even a half of the extreme precipitation as they do during winter. This result is nearly true for all regions, except for Southern Scandinavia, as well as northeastern Europe. Over these areas the model calculates a slight enhanced amount of extreme precipitation. The calculated differences to the reference period (Figure 3.18 B to D) resemble the result for the winter, the differences are considerably lower, though.

Generalized extreme value distribution

Similar to the GEV analysis of temperature, precipitation was analyzed on extreme values as well. The analysis follows the same structure. The monthly precipitation maximum counts as block maximum. Blocks of 30 years are analyzed. The GEV analysis is conducted for three

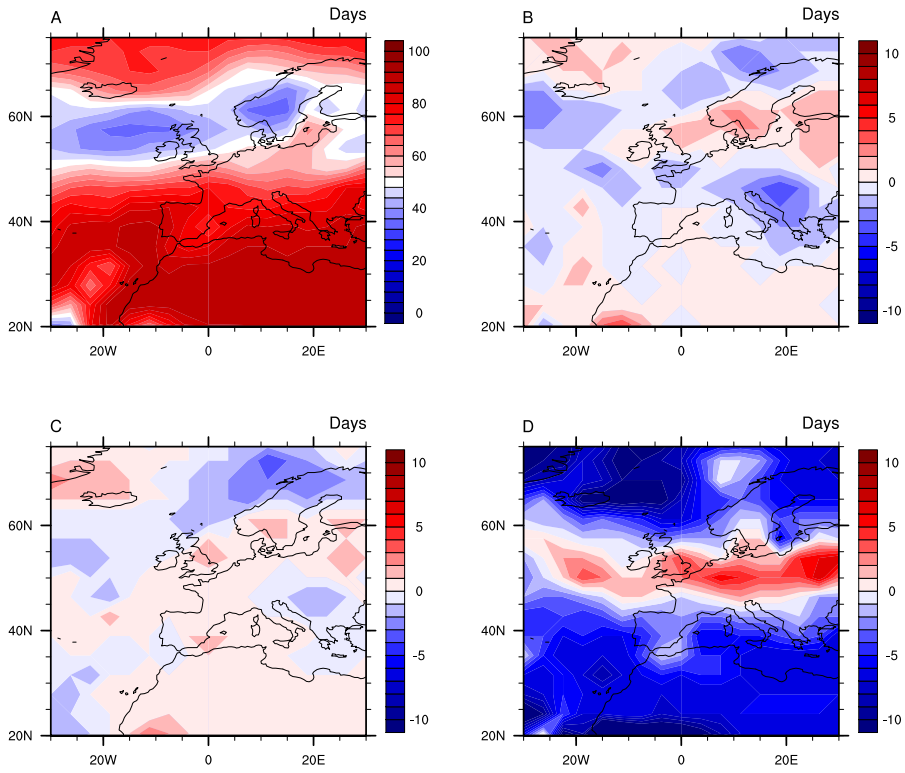

Figure 3.16: The mean number of dry days per summer for the reference period and the comparison of three time slices to the reference period: A) Distribution of dry days during the reference period (1961-1990), B) changes during the Maunder Minimum (1661 - 1690), C) changes in the pre-industrial period (1851 - 1880) and C) changes in the future (2071 - 2100).

regions: Mediterranean, Central and Northern Europe. Figure 3.19 shows for example the precipitation distribution for Northern Europe.

The distribution of precipitation shows a more or less uniform pattern for Northern Europe over time during summer and winter (Figure 3.19). While the Maunder Minimum and the pre-industrial period show rather low precipitation extremes (in blue and green), the future experiences a shift towards higher precipitation extremes (in red). Furthermore, summer is the season with the most wet extremes in Northern Europe. In the Mediterranean, however, summer counts as the driest season (not shown). In contrast to Northern Europe, future extreme precipitation in the Mediterranean are shifted to a lower level, in particular during summer. In the Mediterranean summer, the Maunder Minimum results as a rather wet period. Considering Central Europe, there is also a pronounced shift towards drier extremes during the summer month detectable (not shown). This is valid for the Maunder Minimum, pre-industrial and future period. The most heavy wet extremes in Central Europe can be found for the present. The Maunder Minimum has a similar pattern as the pre-industrial and future period, except in summer. In summer the Maunder Minimum exhibits a shift to wet extremes in comparison to 1850-1880AD and 2070-2100AD.

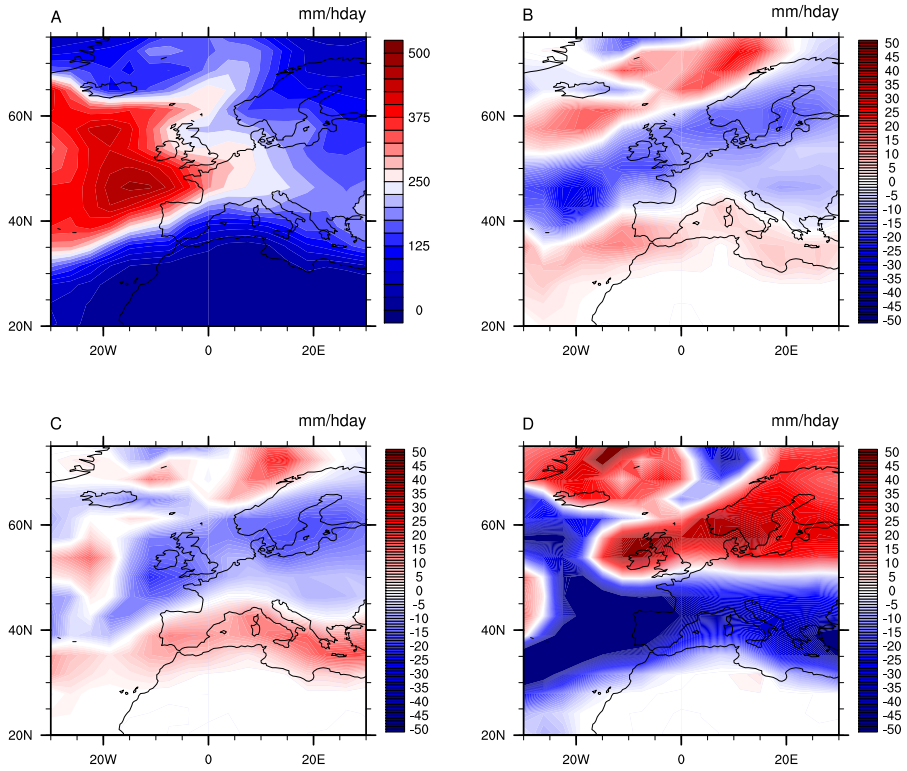

Figure 3.17: The amount of precipitation during heavy precipitation days in December, January and February of the reference period and the comparison of three time slices to the reference period: A) Heavy precipitation distribution during the reference period (1961 - 1990), B) changes during the Maunder Minimum (1661 - 1690), C) changes in the pre-industrial period (1851 - 1880) and D) changes in the future (2071 - 2100).

For both seasons and all regions the GEV parameters of the 30-year time period are calculated. As precipitation extremes of the lower end of the distribution are often equal to zero, a extreme value distribution for precipitation minima are not very useful. Precipitation minima are therefore analyzed later as droughts. The results for the analysis of precipitation maxima are listed in Table 3.6 and Table 3.7.

For the Mediterranean, the location parameter in winter has its highest value in the reference period: 5.92 mm/hday. The lowest value is found in the future, decreasing by 0.47 mm/hday. This corresponds to a loss of 8% of the extreme precipitation amount within a hundred years. Also the Maunder Minimum and the pre-industrial period are calculated to be drier. The Maunder Minimum lies 0.16 mm/hday (-2.7%) below the reference period, the pre-industrial period about 0.24 mm/hday (-4%). Within all periods, the scale parameter σ lies between 2 and 3 mm/hday. Compared to the other grid points (Central and Northern Europe), these deviations are rather high and slightly enhanced for the future (by 0.28 mm/hday compared to the reference period). For Central Europe, the past periods show a decrease like the Mediterranean. In the Maunder Minimum, precipitation extremes lie about 0.29 mm/hday (-5.6%) beyond the reference value, for pre-industrial the extremes decrease by 0.35 mm/hday (-6.7%). Projections of the future reveal a shift towards wetter extremes

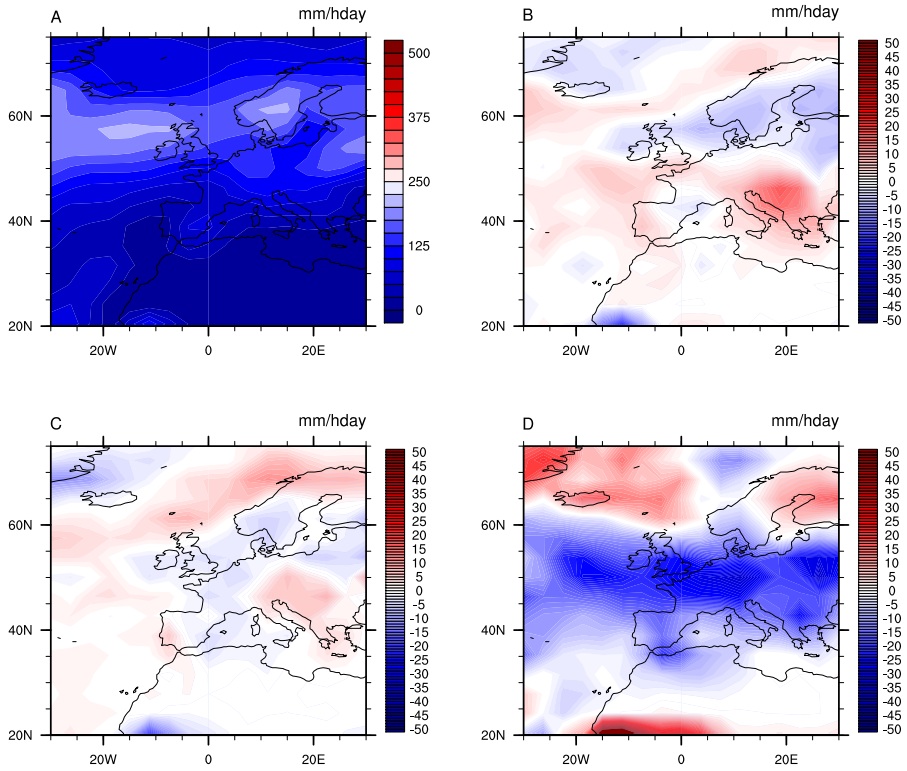

Figure 3.18: The amount of precipitation during heavy precipitation days in June, July and August for the reference period and the comparison of three time slices to the reference period: A) Heavy precipitation distribution during the reference period (1961 - 1990), B) changes during the Maunder Minimum (1661 - 1690), C) changes in the pre-industrial period (1851 - 1880) and D) changes in the future (2071 - 2100).

in the winter of Central Europe. The extreme precipitation rises by 0.82 mm/hday (+16%). Northern Europe behaves like Central Europe. The driest era is the pre-industrial period. The location parameter μ is calculated to be 2.62 mm/hday. Compared to the reference period, this corresponds to a decrease of 10.6%. The mean of the precipitation extreme values during the Maunder Minimum is about 9.2% lower (2.66 mm/hday). The largest extreme location is again calculated for Northern Europe by 4.02 mm/hday (+37.2%).

The results of the winter extreme value analysis (Table 3.6) are comparable to the results for the summer season. For Central and Northern Europe, the values of the location parameter for the past periods are lower than the reference period (by 2.2% to 5.7%). Increases are calculated for the future, though. The precipitation extreme value location for Northern Europe is about 13.9% higher than the reference period. For Central Europe the model calculates an increase in precipitation extremes by 2.7%. The Mediterranean behaves slightly different in summer than in winter. The wettest extremes are not calculated for the reference period, as they are in winter, but for the Maunder Minimum. The extreme precipitation location parameter for the Mediterranean is calculated to be 4.48 mm/hday, which is 7.4% higher than the reference period. The extreme precipitation locations for pre-industrial (4.12 mm/hday, -1.2%) and future (3.21 mm/hday, -23%) are lower than the location parameter

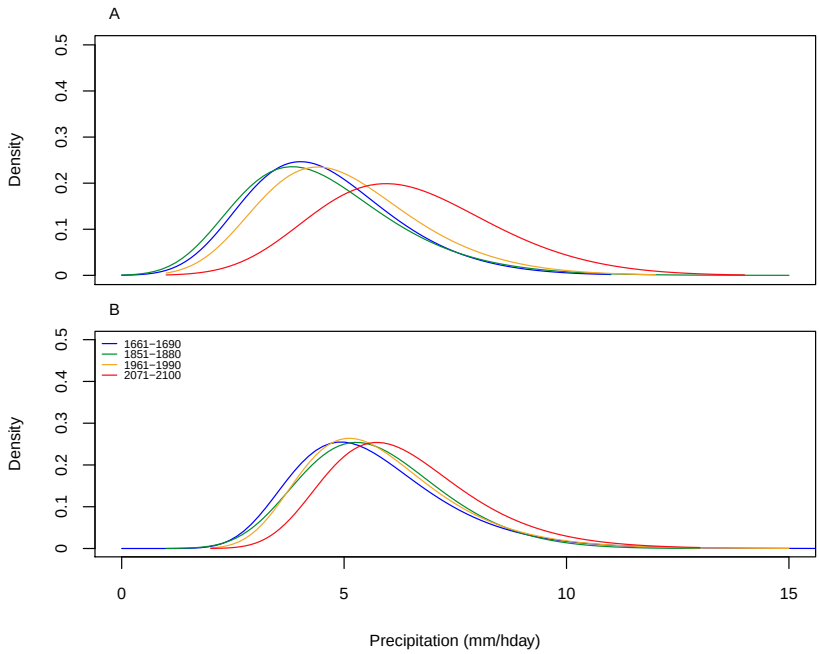

Figure 3.19: Probability density functions of extreme precipitation of Northern Europe. A) winter (DJF) and B) summer (JJA).

for the reference period (4.17 mm/hday). This is observed in winter as well.

Similar to the calculations for temperature, the precipitation GEV parameters belong uniformly to the Weibull family. The scale parameter (σ) emphasizes the result of the analysis of the probability density functions: the precipitation distribution of Central Europe is considerably wide, denoting a fat-tail behavior. Of the examined regions, Central Europe results in the lowest values of σ. The largest variation is calculated for the Mediterranean, throughout all periods of time. Simultaneously, the shape parameter ξ is considerably low. This leads to the conclusion that the upper tail of the heavy precipitation distribution is largest for the Mediterranean. For Northern Europe, σ is large compared to Central Europe, but lower as the values for the Mediterranean. The values for ξ in the extreme precipitation distribution for Northern Europe are though smaller than those for the Mediterranean and Central Europe. The tails for Northern Europe can therefore be interpreted as heavy, but as the shape parameter is low, the upper and the lower tail are likewise large.

The standard errors for the precipitation GEV parameters are given in Table 3.8. Compared to Table 3.2, the standard errors for precipitation are smaller than for temperature.

Table 3.6: Extreme value distribution parameters for winter precipitation. One parameter per 30-year time slice and area: Mediterranean, Central Europe and Northern Europe.

		μ	σ	ξ
1660	Mediterranean	5.76	2.24	-0.12
	Central Europe	4.91	1.59	-0.11
	Northern Europe	2.66	1.17	-0.06
1850	Mediterranean	5.68	2.19	-0.13
	Central Europe	4.85	1.55	-0.07
	Northern Europe	2.62	1.18	-0.09
1960	Mediterranean	5.92	2.15	-0.09
	Central Europe	5.20	1.67	-0.14
	Northern Europe	2.93	1.30	-0.12
2070	Mediterranean	5.45	2.43	-0.08
	Central Europe	6.02	1.71	-0.13
	Northern Europe	4.02	1.59	-0.15

Return levels

Figure 3.20 presents, as an example, the return levels for precipitation extreme values in winter and summer for Northern Europe. It resembles the interpretation of the GEV parameters earlier. All periods have a similar distribution in precipitation extremes, slightly enhanced are the return levels for the future (denoted in red). The Maunder Minimum and the pre-industrial period are similarly dry. In winter the Maunder Minimum is clearly the driest period of time (in blue). In summer, though, the precipitation extremes of the pre-industrial period are even lower than those of the Maunder Minimum. The future experiences a shift towards higher return levels for both seasons.

The distribution of the 50-year return levels across Europe is shown in Figure 3.21 for winter and Figure 3.22 for summer. The spatial pattern is similar to the extreme precipitation distribution shown earlier (compare Figure 3.17 and Figure 3.18) which indicates the correctness of the statistical model. Considering the differences of the past periods (Maunder Minimum and pre-industrial period) to the reference period, only small changes are detectable. Northern Europe results in a slight decrease of the 50-year return levels during winter. The return levels for Central Europe are slightly larger during the past periods, which denotes an increase in extreme precipitation. For the Mediterranean the picture of change is less distinct as for Northern Europe. In some areas the model calculates lower extreme precipitation return levels, in other regions the return levels are higher. The winterly changes of the return levels are larger for the future than for the past periods. On the 50 year return period, an increase of the return levels are calculated all across Europe. Decreases are mainly visible over Africa.

Compared to the changes in winter, the changes in return levels for summer is less distinct. Figure 3.22 B to D gives a spotty picture. No large scale changes can be detected. Some

Table 3.7: Extreme value distribution parameters for summer precipitation. One parameter per 30-year time slice and area: Mediterranean, Central Europe and Northern Europe.

		μ	σ	ξ
1660	Mediterranean	4.48	2.62	-0.33
	Central Europe	3.64	1.38	-0.04
	Northern Europe	4.15	1.29	-0.01
1850	Mediterranean	4.12	2.74	-0.30
	Central Europe	3.59	1.45	-0.05
	Northern Europe	4.27	1.43	-0.07
1960	Mediterranean	4.17	2.83	-0.33
	Central Europe	3.72	1.43	-0.13
	Northern Europe	4.40	1.55	-0.01
2070	Mediterranean	3.21	3.03	-0.28
	Central Europe	3.82	1.44	-0.15
	Northern Europe	5.01	1.67	-0.08

Table 3.8: Standard errors of the extreme value analysis for precipitation

	μ	σ	ξ
Winter	[0.07, 0.13]	[0.05, 0.09]	[0.03, 0.04]
Summer	[0.08, 0.18]	[0.05, 0.13]	[0.02, 0.04]

areas, such as Northern Europe, show slightly lower return levels during the Maunder Minimum and the pre-industrial period. Central Europe and the Mediterranean result in rather higher return levels for the pre-industrial period. The spotty picture can also be found in the future, even if the changes are larger. Larger precipitation extreme values can be found over Northern Europe and parts of Central Europe (such as France and the British Isles). In the Mediterranean, some areas show clearly lower return levels, such as Greece and Portugal.

Over time, precipitation return levels increase. The only exception experiences a greater region around Greece and Spain/Morocco (see Figure 3.21 and Figure 3.22). During summer a distinct decline of extreme precipitation is visible. This picture can also be gained by the interpretation of the explicit return levels for the Mediterranean (Table 3.9 and Table 3.10).

Distinct return levels for the Mediterranean, Central Europe and Northern Europe are given in Table 3.9 for winter and in Table 3.10 for summer. Considering the 50 year return levels for winter in the Mediterranean, a decrease during the past periods can be detected. Compared to the reference period (1961-1990), the 50 year return levels decreases by 0.43 mm/hday (-2.9%) for the Maunder Minimum and by 0.78 mm/hday (-5.3%) for the pre-industrial period. For the future, precipitation extremes become even more intense. The 50 year return level rises

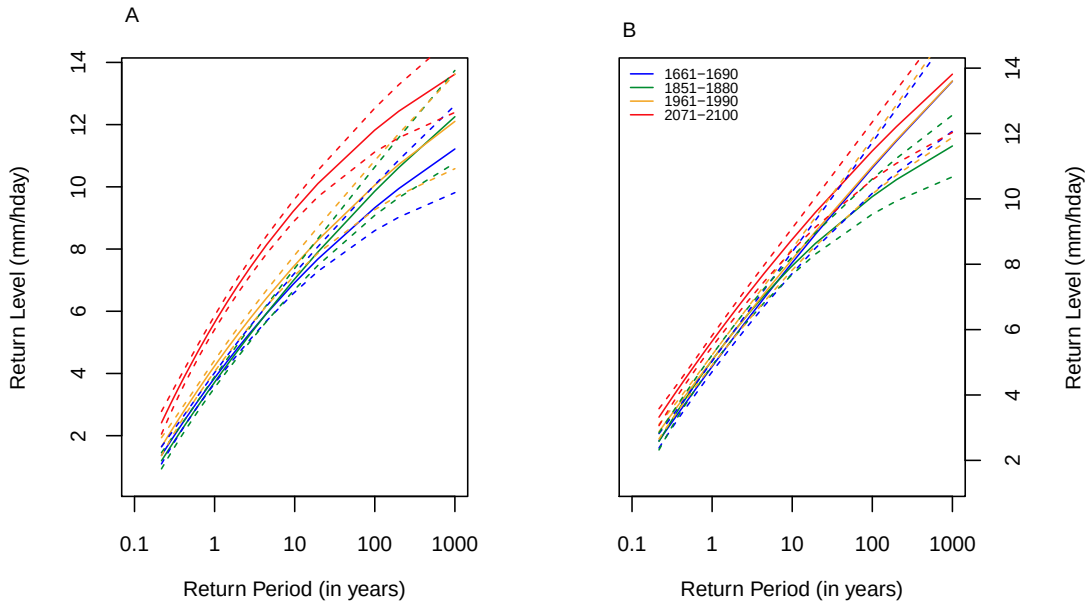

Figure 3.20: Return levels of precipitation extremes of Northern Europe for different return periods. A) DJF, B) JJA.

by 0.82 mm/hday, which corresponds to a rise of 5.6%. A similar development can be found for the summer periods. However, while the Maunder Minimum precipitation extremes are again on a lower level (-0.28 mm/hday, -2.5%), precipitation extremes for the pre-industrial period are slightly enhanced (+0.11 mm/hday, +1%). A rise in precipitation extremes is also detectable for the future in the Mediterranean (+0.32 mm/hday, +2.9%). Central Europe behaves slightly different. In winter, the Maunder Minimum shows the lowest precipitation extremes. The 50 year return level decreases by 0.14 mm/hday, which is equal to a decrease of 1.3%. In contrast to the Mediterranean (and Northern Europe as well), extreme precipitation is slightly enhanced during the pre-industrial period in Central Europe. An increase is also calculated for the future in winter. The 50 year return level increases by 1.21 mm/hday (10.9%) in the winter to the end or 21st century. The picture is different for the summer periods in Central Europe. The model calculated enhanced return levels during the Maunder Minimum and pre-industrial (+11.0% and +11.4%), but a lower value for the future (-1.2%). In Northern Europe, both past periods are considerably drier in winter and summer than the reference period. The largest decrease can be found in the pre-industrial period. Extreme precipitation return levels decrease by 0.53 mm/hday (-6.7%) in winter and by 1.78 mm/hday (-15%) in summer. A large decrease is also evident for the Maunder Minimum: -2.8% in winter and -12% in summer. While the 50 year return level increases by remarkably 21% (1.66 mm/hday) in winter in the future, the return level decreases slightly by 0.3% in summer.

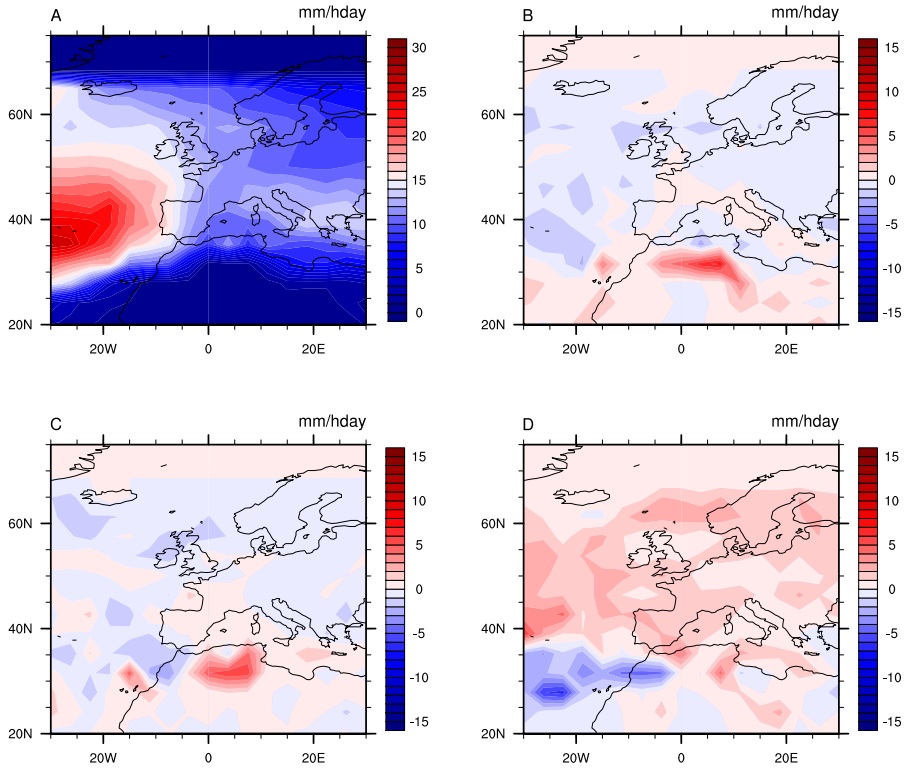

Figure 3.21: A) European return level map for a 50-year return period of winter precipitation during the reference period (1961-1990), B) comparison of the Maunder Minimum (1661-1690), C) the pre-industrial period and D) the future to the reference period.

3.2.2 Droughts

An analysis of droughts is conducted on the basis of the Standardized Precipitation Index (SPI). Again, it is focused on the representative areas (Mediterranean, Central Europe and Northern Europe), as well as on characteristic periods of time (Maunder Minimum, pre-industrial, present (also reference period) and future). In this section, only the resulting graphs for the Mediterranean are shown. All though the SPI is also able to represent wetnesses, the main emphasis lies on the analysis of droughts.

The calculation of the SPI includes only precipitation. Most of the time a dry period influences the drought character for longer than just a month. Therefore, the amount of precipitation of consecutive months on different time scales are taken into account. Due to the long data set (600 years), only long term pattern of droughts are considered. Four time scales are chosen: 12-months, 24-months, 48-months and 72-months. On longer time scales, only severe droughts appear. Figure 3.23 represents the SPI time series from 1500 AD to 2100 AD. For A) to D) the time scale increases. All time series resemble the hypothesis of a drier future in the Mediterranean. For Central Europe and Northern Europe, the SPI tends to positive values in the future, thus suggesting less dry conditions.

Negative SPI values (droughts) are analyzed applying the GEV analysis. In a first step, all

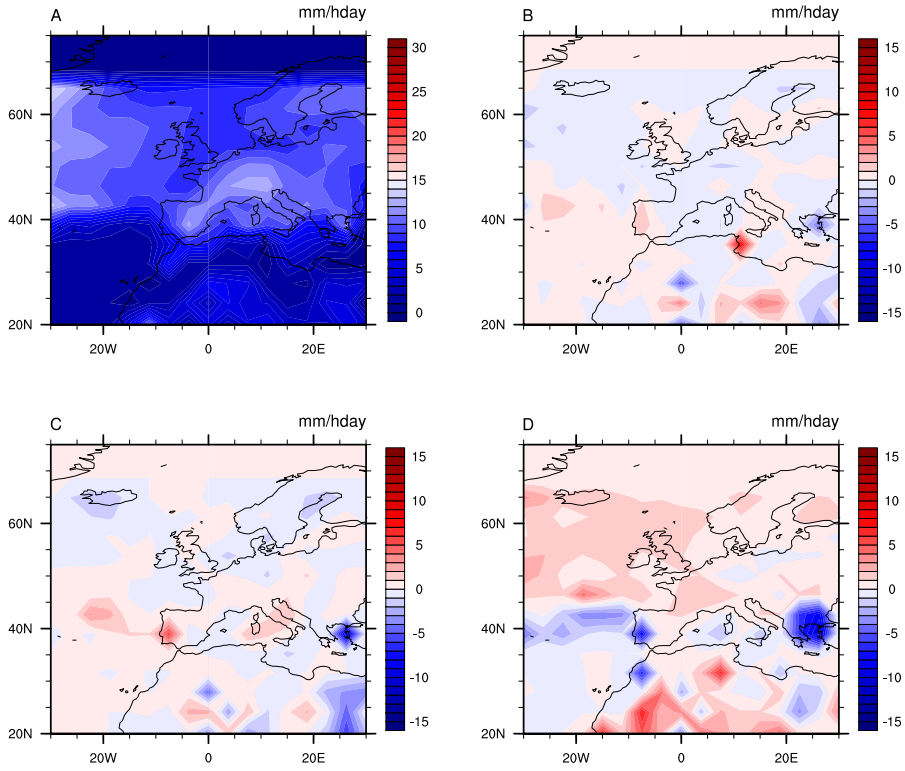

Figure 3.22: A) European return level map for a 50-year return period of summer precipitation during the reference period (1961-1990), B) comparison of the Maunder Minimum (1661-1690), C) the pre-industrial period and D) the future to the reference period.

time scales are dissected. The GEV parameters are calculated from 1500AD to 2100AD in 30 year time steps (Figure 3.24). Regarding the location parameter, the different SPI scales follow a similar pattern over time. Deviations from zero (either towards wet or dry conditions) occur around the same time, only the amplitude differs. This denotes, that the moment of an occurring drought does not change with increasing time scale, only the severity of the dry event changes with an increasing number of time steps considered. The parameters scale σ and shape ξ, though, react more sensitive on changes in time scale. If the 72-months SPI is followed, a anti-correlation of the scale and shape parameter can be detected. In order to estimate this pattern more precisely, the calculation is redone for each period of time (Maunder Minimum, pre-industrial, present and future) on the level of a 12-months SPI and a moving 30 year window (compare Figure 3.25).

The 12-months SPI is chosen for a deeper investigation, as an influence of 12 months to the drought condition of a specific point of time is the most realistic. There are only few droughts in the mid-latitudes that last more than a year. Figure 3.25 is the result of the detailed parameter analysis.While the shape parameter follows more or less the location parameter, the scale parameter is anti-correlated. Thus, if the SPI describes a wetness ($SPI > 1$), the shape parameter lies between zero and 0.5 ($0 < \sigma < 0.5$), with a declining location parameter (a change from wet to dry conditions), the scale parameter rises. A rising scale parameter

Table 3.9: Winter precipitation: return levels for characteristic areas and time periods on four return periods in mm/hday.

		10 years	25 years	50 years	100 years
1660	Mediterranean	12.01	13.30	14.21	14.99
	Central Europe	9.38	10.31	10.96	11.52
	Northern Europe	6.21	7.04	7.67	8.22
1850	Mediterranean	11.70	12.97	13.86	14.62
	Central Europe	9.53	10.55	11.40	12.08
	Northern Europe	6.07	6.82	7.36	7.84
1960	Mediterranean	12.16	13.68	14.64	15.46
	Central Europe	9.64	10.53	11.10	11.67
	Northern Europe	6.60	7.34	7.89	8.38
2070	Mediterranean	12.72	14.34	15.46	16.20
	Central Europe	10.71	11.65	12.31	12.87
	Northern Europe	8.21	9.05	9.55	10.05

denotes a rise in the variability. For wet conditions, the shape parameter is clearly larger than zero ($\xi > 0$), the distribution therefore belongs to the Fréchet family. If the location parameter declines, the shape parameter falls below zero. Drier conditions evoke a change in shape. During a drier period, the distribution belongs to the Weibull family. This means, that changes in wetness conditions also affects the tail of the distribution. Such a behavior is in particular evident for earlier periods such as the Maunder Minimum and the pre-industrial period. Later in time, the anti-correlation weakens.

As a last indicator, the development of the 50-year return level for dry extremes on different time scales of the SPI (12- to 72-months) and for all regions is considered (Figure 3.26). The return levels on the 50-year return period, support the assumptions made above. While dry extremes tend to increase in the future in the Mediterranean, they tend to decline in Central and Northern Europe. During the Maunder Minimum, there is a clear increase of droughts visible in the Mediterranean. In Central Europe droughts were frequent in a period before the Maunder Minimum, but less frequent during the cold period of the Maunder Minimum. The same is true for Northern Europe, but weaker. Both regions show again an increase in droughts towards the end of the Maunder Minimum. Furthermore, Central and Northern Europe experience lower drought frequencies during mid and later 21st century.

3.2.3 Underlying Dynamics

Figure 3.27 and Figure 3.28 depict the geopotential height anomaly on 500 hPa winter and summer, respectively. Figures 3.27 and 3.28 are the result of analysis of the five most severe droughts for each simulation. For each drought the geopotential height anomaly is calculated. Therefore the geopotential height pattern of the according 30 year time period is subtracted

Table 3.10: Summer precipitation: return levels for characteristic areas and time periods on four return periods in mm/hday.

		10 years	25 years	50 years	100 years
1660	Mediterranean	9.80	10.56	10.90	11.24
	Central Europe	8.04	9.19	9.93	10.87
	Northern Europe	8.48	9.60	10.43	11.27
1850	Mediterranean	9.96	10.81	11.29	11.66
	Central Europe	8.04	9.15	9.96	10.67
	Northern Europe	8.47	9.42	10.08	10.52
1960	Mediterranean	10.00	10.73	11.18	11.46
	Central Europe	7.63	8.42	8.94	9.14
	Northern Europe	9.51	10.90	11.86	12.82
2070	Mediterranean	9.93	10.87	11.50	11.91
	Central Europe	7.66	8.39	8.83	9.34
	Northern Europe	9.94	11.02	11.82	12.53

from the geopotential height pattern of the drought. Finally, the resulting geopotential height anomaly fields per drought are averaged.

Winter droughts are induced by stable high pressure that dry continental air to the Mediterranean, Central or Northern Europe (Figure 3.27). For the Mediterranean the high pressure is spread over the entire western Europe. Dry air is transported from Northern Africa and Asia to the Mediterranean region. Besides the high pressure over the Atlantic and Iceland, droughts over Central Europe are influenced by low pressure over east Europe and Russia. Cold and dry air is therefore advected from the east European continent to Central Europe. For Northern European droughts, high pressure covers the entire Barents Sea. Low pressure can be found over the Mediterranean. In such a situation, droughts are caused by cold and dry air advection from Russia.

For Mediterranean summer droughts, the geopotential height anomaly pattern resembles the pattern of winter droughts (Figure 3.28). High pressure spans over the entire west European continent. The positive geopotential height anomaly extends further like a belt to Northern America. The air causing droughts in the Mediterranean originates therefore again from north Africa, the Arabic area or Asia. In contrast to Central European droughts in winter, summer droughts are influenced by high pressure covering Central Europe and parts of the Scandinavian countries. Similar to the Mediterranean, dry air is transported to Central Europe originating from Asia or Eastern Europe. Besides the high pressure over Greenland, droughts over Northern Europe are further influenced by low pressure over Central Europe. Dry continental air is transported from Russia to Scandinavia.

The findings of positive geopotential height anomalies are supported by *Yiou and Nogaj* [2004]. They investigated extreme climatic events over Northern Atlantic and found similar pressure

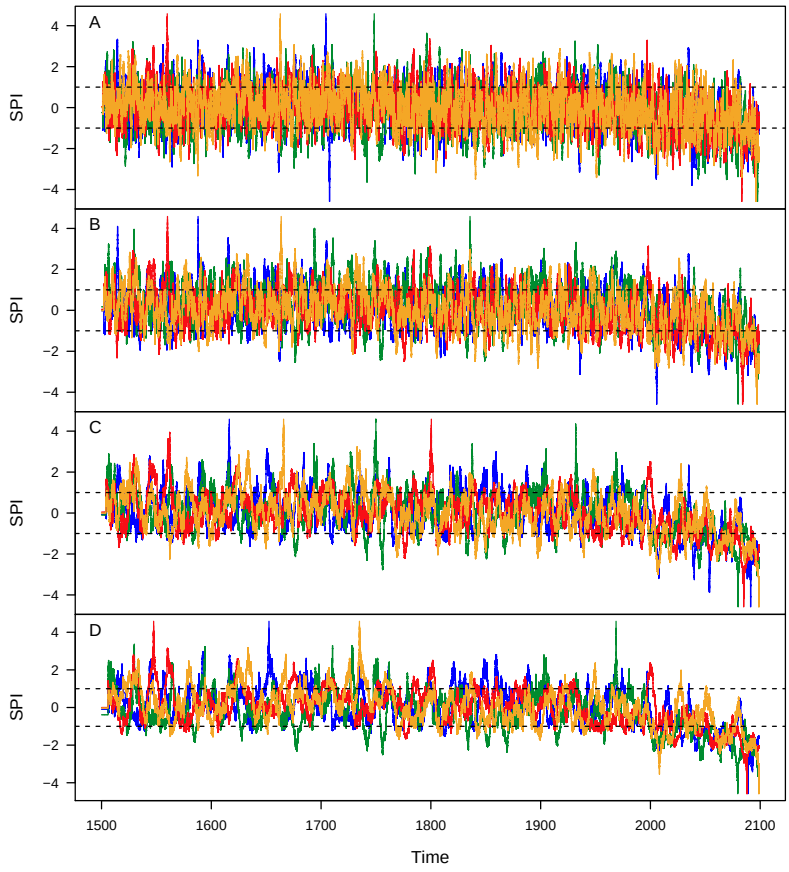

Figure 3.23: SPI time series of the Mediterranean on different time scales: A) 12-months, B) 24-months, C) 48-months and D) 72-months. The colors denote the transient runs of the climate model.

centers as were calculated for Central European droughts. *García-Herrera et al.* [2007] who examined severe droughts of 2004 and 2005 over the Iberian Peninsula describe associated geopotential height anomalies as found for Mediterranean summer droughts in Figure 3.28, i.e., a positive anomaly over Western and Southern Europe and a negative anomaly towards north Atlantic. The current findings also reflect the findings of *Buehler et al.* [2011].

3.2.4 Discussion

Model evaluation

The precipitation distribution of the CCSM3 climate model is evaluated by the comparison of mean and standard deviation to the ERA-40 data set. Input values are precipitation amounts in millimeter per half-day. The agreement of the model calculation (first column) and ERA-40 data (second column) is overall better in summer (Figure 3.29 D to F) than in winter

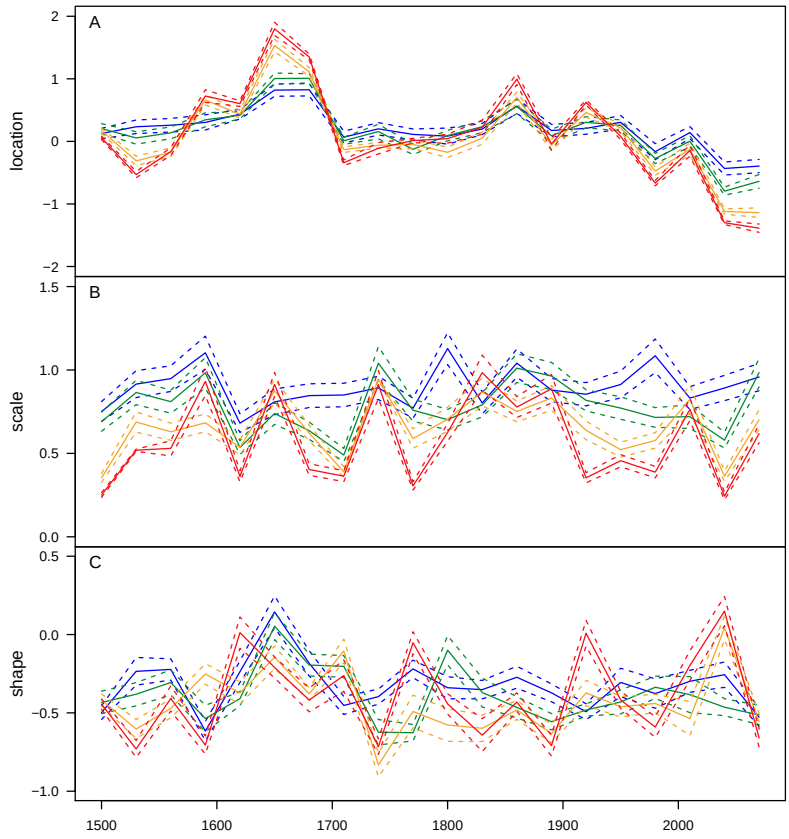

Figure 3.24: GEV parameters for different time scales of the SPI: A) location parameter, B) scale parameter and C) shape parameter. The colors signify the different time scales: 12-months (blue), 24-months (green), 48-months (orange) and 72-months (red).

(Figure 3.29 A to C). In summer, the modeled precipitation amount are slightly smaller than the measured values, especially over Central Europe and the Mediterranean area. During winter, the more intense precipitation months, deviations from the model to the observation are larger. The precipitation amount of the west coast of the Scandinavian Peninsula is underestimated in the model simulations. Over central Europe on the other hand, the model precipitation shows a positive bias during 1961-1990 period.

The standard deviation of the precipitation distribution over Europe is generally smaller in the model than in the observations.This is especially the case where the model results and observational data deviate in mean as well. The most prominent example is the west coast of Norway during winter. Both, the precipitation mean, as well as the standard deviation is too small. Summarizing, the model represents mean precipitation amounts over continental Europe reasonably well when taking into account the rather low resolution of the model.

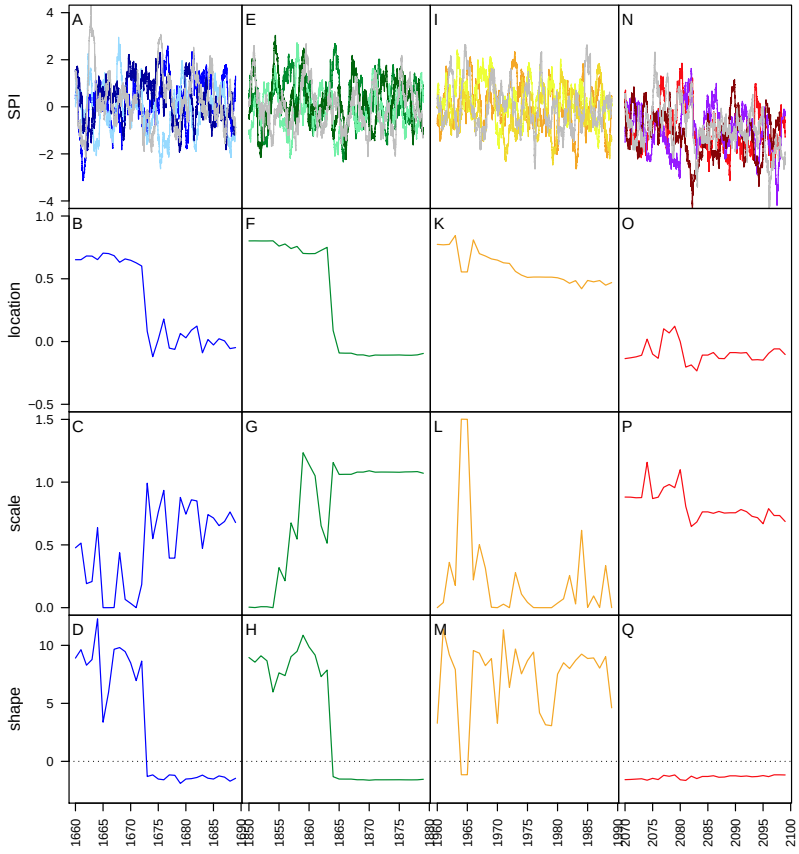

Figure 3.25: GEV parameters for dry SPI and each period of time. The GEV parameters are calculated on a 30-year moving window. The Maunder Minimum is analyzed in the first column (A - D), the pre-industrial period is shown in column two (E - H), followed by the present in column three (I - M) and the future in column four (N - Q). The first line gives the SPI of the particular time period for different transient runs of the climate model. Line two to four depict the GEV parameters location, scale and shape. The last 14 time steps in the future (2086-2100) are not exactly calculated for a 30-year window, as model results after 2100 are missing. For the last step, only 15 backward years are used. Thus, the results of the last 14 years are not fully consistent.

Changes in extreme climate

Past precipitation extremes are not fairly easy to compare. Precipitation reconstructions can only be conducted on mean precipitation [*Jones and Mann*, 2004, *Pauling et al.*, 2006 and *Raible et al.*, 2006] and only few work is available on extremes utilizing climate model simulations of the past [*Pauling and Paeth*, 2007]. Most analyses on extreme values is either performed on present measurements [*Groisman et al.*, 2005] or future climate projections [*Kharin and Zwiers*, 2005; *Frei et al.*, 2006; *Nikulin et al.*, 2011 and others].

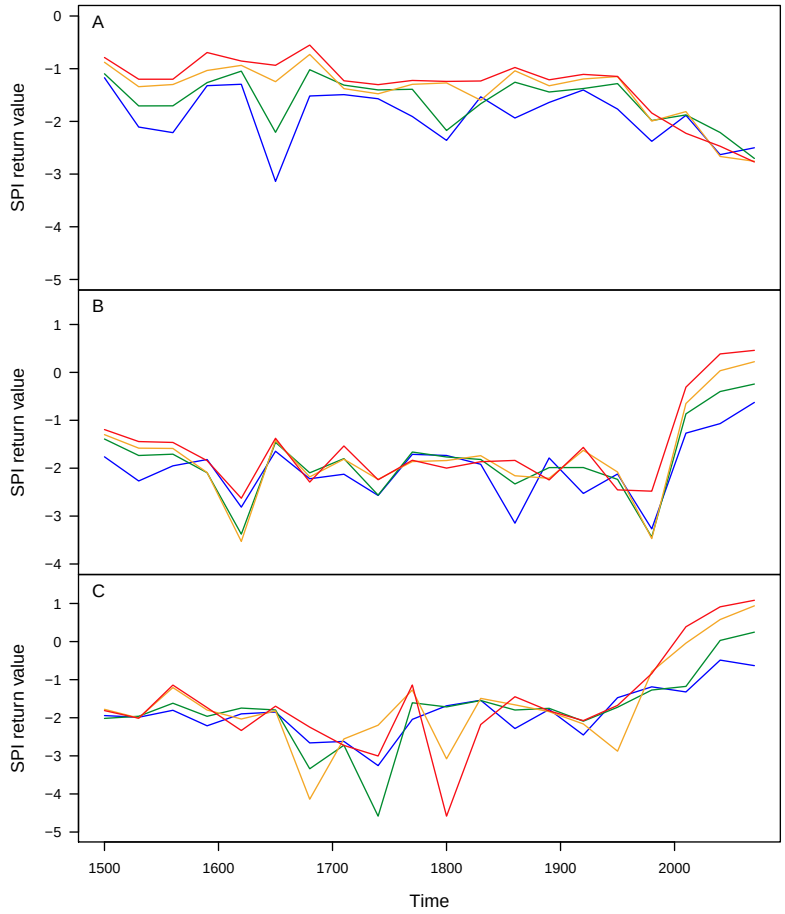

Figure 3.26: Return levels of the 50year return period of dry extremes of the SPI on different time scales: 12-months in blue, 24-months in green, 48-months in orange and 72-months in red. A) is the result for the Mediterranean area, B) for Central Europe and C) for Northern Europe.

Pauling et al. [2006] reconstructed the precipitation pattern of the last 500 years for Europe. For winter (DJF), they found a stable precipitation pattern from 1500 to 1700 and a sharp rise during the late Maunder Minimum (1705-1720). During the 19th century they detected a slow decrease in mean precipitation with a subsequent positive trend in the 20th century. They found a gradual increase in summer precipitation (JJA) from 1500 to 1660. The following 100 years were dominated by high decadal precipitation variability. Especially late 17th century experienced extremely dry summers (1666 and 1669). Thereafter (from 1800 to 1983) they detected variability decreases with no overall trends.

In another study *Pauling and Paeth* [2007] estimated return levels for precipitation extremes from 1700 to 2000 in different regions across Europe. For the Mediterranean (Southern Spain), they found consistent return levels for different return periods (5 year, 10 year, 20 year and

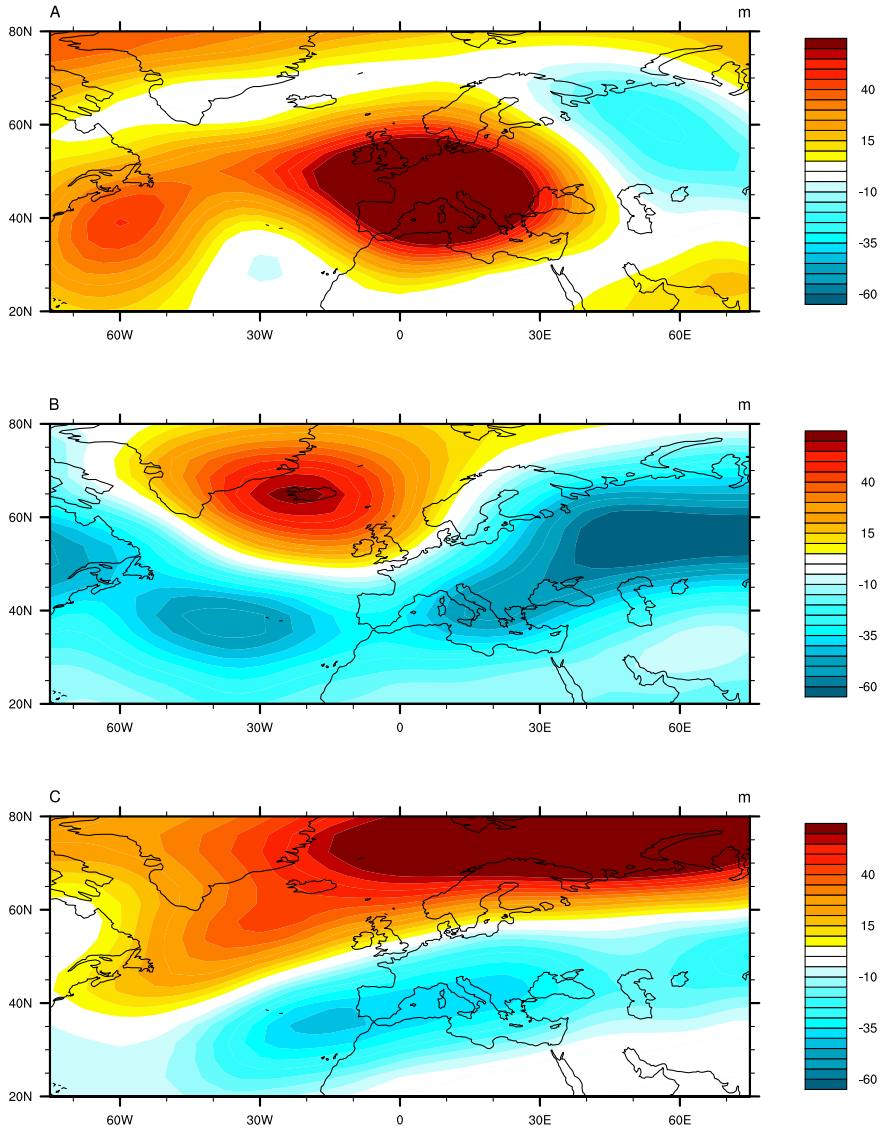

Figure 3.27: Atmospheric dynamics during droughts in winter. Geopotential height anomaly on 500 hPa for droughts in A) the Mediterranean, B) Central Europe and C) Northern Europe in winter.

50 year periods) during a pre-industrial period (1851-1880). For the 50 year return period, they calculated return levels between 250 mm/season and 300 mm/season for wet winters. Compared to the results achieved by the analysis of the CCSM3 model for the Mediterranean during the pre-industrial period (14 mm/hday for winter), the values calculated by *Pauling and Paeth* [2007] are significantly lower. This statement is true for Central Europe and Northern Europe as well. Comparable to the Mediterranean, *Pauling and Paeth* [2007] estimated more or less consistent return levels from 1851 to 1880, in a range of 130-140 mm/season for Northern Europe and 300-350 mm/season for Central Europe. The 50 year return levels calculated in the model range from 7 mm/hday to 11 mm/hday for Central and Northern Europe in both seasons (DJF and JJA). A similar picture gives the comparison of the return

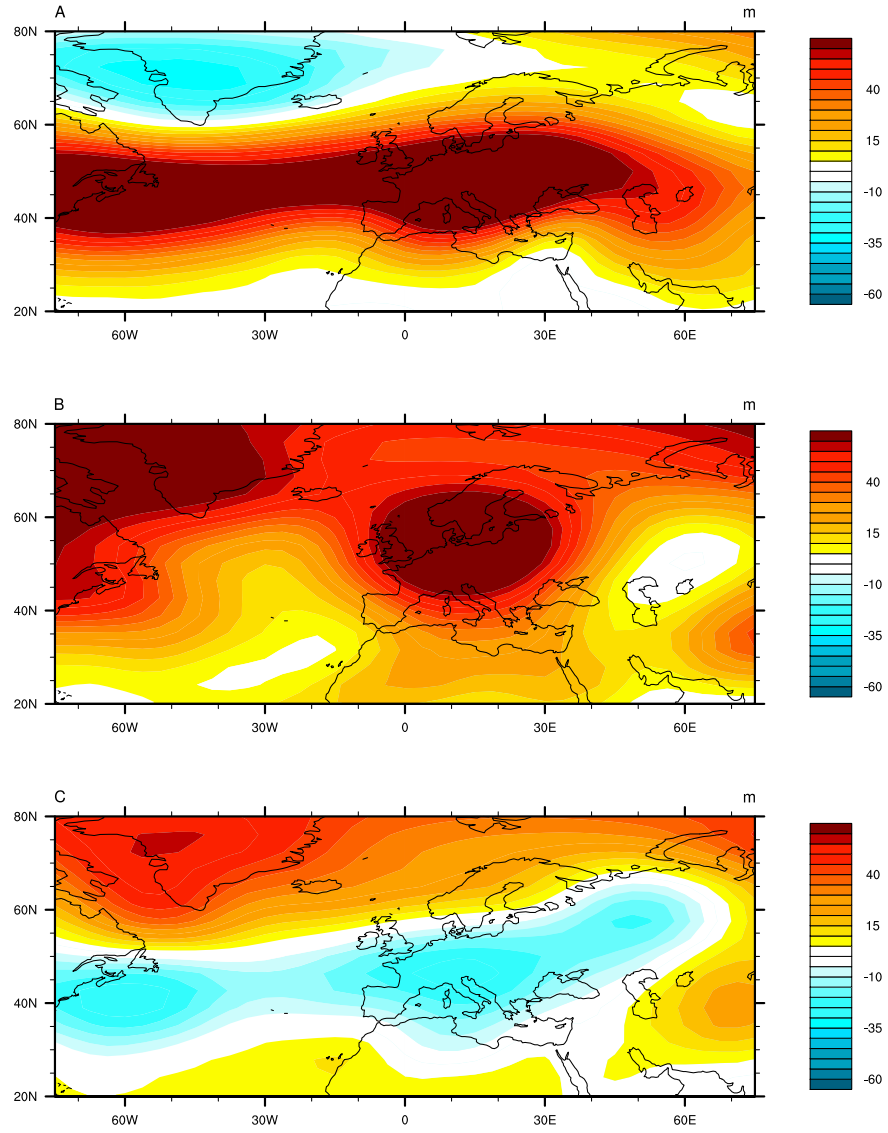

Figure 3.28: Atmospheric dynamics during droughts in summer. Geopotential height anomaly on 500 hPa for droughts in A) the Mediterranean, B) Central Europe and C) Northern Europe in summer.

levels of the reference period (1961-1990) in the model. Seasonal extreme precipitation return levels are not directly comparable to half-daily precipitation extremes though, as extreme precipitation events do not last more than several days.

Frei et al. [2006] calculated 5 year return levels for 1-day precipitation extremes in autumn. These return levels can neither be compared directly, as the return period is lower (5 years instead of 50 years), the season differs (autumn instead of DJF or JJA) and the resolutions of the models are significantly higher. Still, on a 5 year return period *Frei et al.* [2006] calculated return levels between 30 mm and 140 mm over Switzerland. Very high return levels are only calculated for Alpine regions, though. Compared to the return levels calculated for Central

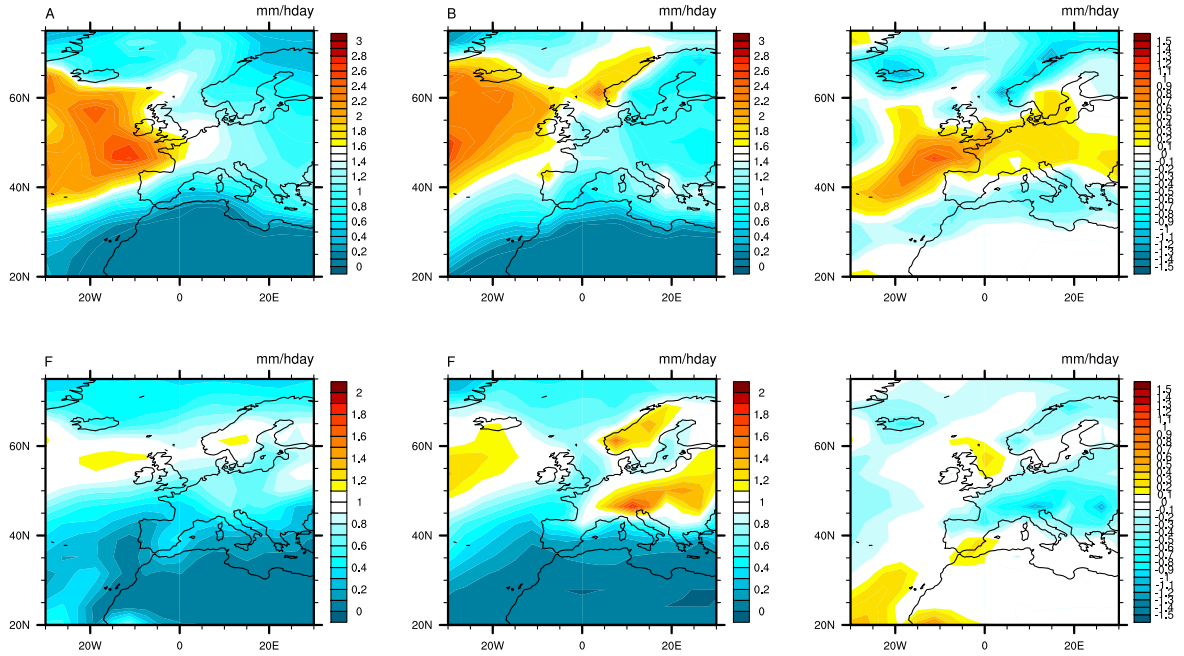

Figure 3.29: Model evaluation for mean precipitation: A) DJF of the CCSM3 model, B) DJF of ERA-40 data, C) Differences of model and data; D) JJA for the CCSM3 model, E) JJA of the ERA-40 data, F) Differences of model and data.

Europe (9 mm/hday to 11 mm/hday) in the same period of time (1961-1990) in the CCSM3 model, the values calculated by *Frei et al.* [2006] are significantly higher. An alike result is found comparing the findings of *Nikulin et al.* [2011]. A calculation error can nearly be excluded, as the maximum precipitation in the CCSM3 model (from 1500 to 2100) lies at 20.8 mm/hday in winter in the Mediterranean, at 15.5 mm/hday in winter in Central Europe and at 15.1 mm/hday in summer in Northern Europe. The reason for the distinctive lower return levels is rather the low resolution of the climate model used for the calculation. Figure 3.31 depicts the return levels calculated of *Frei et al.* [2006] for different climate models on different resolutions. Most obvious is the decrease of the return levels for lower grid resolutions. The lowest return levels are calculated for the HADAM3H climate model, an atmosphere-only global climate model of the Hadley Centre at the U.K. Met Office. However, with a horizontal resolution of about 150 km in the mid-latitudes, the HADAM3H is still finer resolved as the CCSM3 model (about 270 km horizontal resolution at 50° north). Additionally considering the differences in the unit used (*Frei et al.* [2006] calculated in mm/day), the low return levels calculated in the CCSM3 model are explainable.

As discussed earlier, the return levels calculated in the framework of the present thesis cannot be contrasted directly to other findings. Though, the relative changes in time are comparable. *Luterbacher et al.* [2004] denoted the Maunder Minimum as a period with cold and dry winters. The decrease of winter precipitation extremes are therefore explainable. Compared to the reference period, the 50 year return levels of the winters in the Mediterranean, Central Europe and Northern Europe are between 1.3% (Central Europe) and 2.9% (Mediterranean)

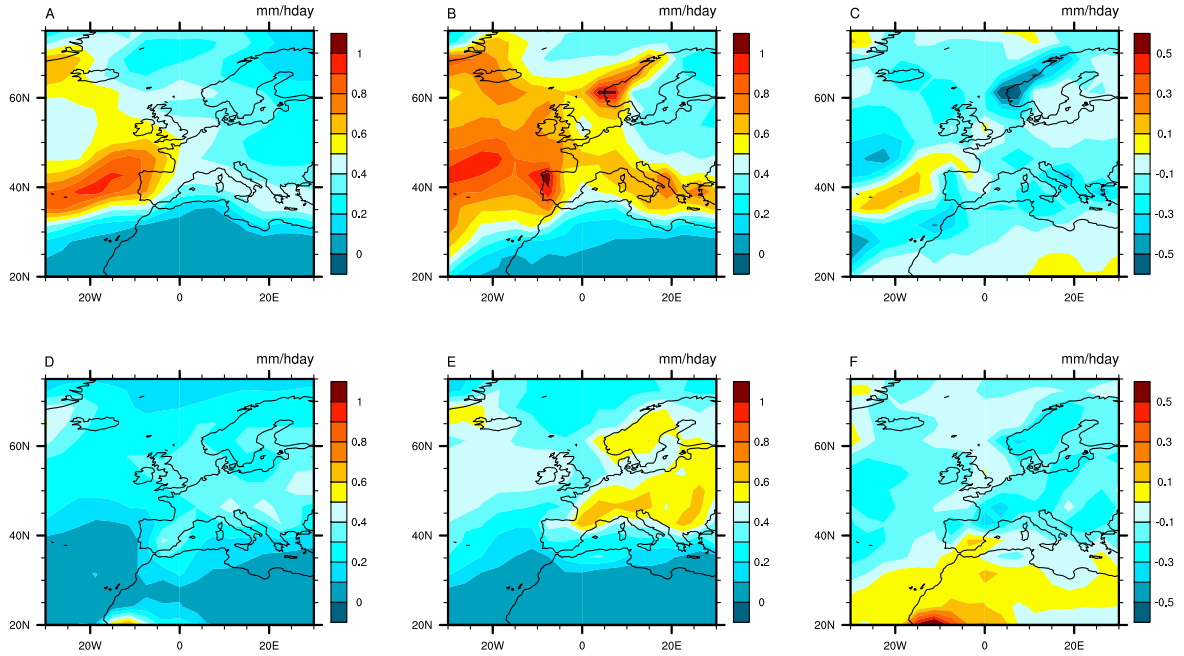

Figure 3.30: Model evaluation for standard deviation of precipitation: A) DJF of the CCSM3 model, B) DJF of ERA-40 data, C) Differences of model and data; D) JJA for the CCSM3 model, E) JJA of the ERA-40 data, F) Differences of model and data.

lower. In the pre-industrial period, winter precipitation extremes are calculated to be 5.3% lower compared to the reference period in the Mediterranean. This result is supported by the finding of *Pauling and Paeth* [2007] who found significantly lower return levels in 1851-1880 (around 500 mm/season) than at the end of the 20th century (around 600 mm/season) in the Mediterranean. Similar holds true for Northern Europe. Precipitation extremes in the CCSM3 model are estimated to be 6.7% lower in the pre-industrial winter. This can also be seen in the results of *Pauling and Paeth* [2007]: around 140 mm/season in 1851-1880 and around 190 mm/season towards 2000. In Central Europe *Pauling and Paeth* [2007] estimated a slight decreasing return level by 1851-1880 (around 350 mm/season, compared to 400 mm/season in the reference period). In the CCSM3 model though, the winter precipitation extreme return level are estimated to be larger than the level of the reference period: an increase of 2.7% is calculated. For summer precipitation, the Northern European return levels of the pre-industrial and reference period is compared to the findings of *Groisman et al.* [2005]. They clearly state a positive trend of extreme precipitation from early measurements to the present. The calculations on the CCSM3 model results reveal an increase by 15% in summer from the pre-industrial to the reference period, which seem reasonable. Further *Xoplaki et al.* [2004] and [*Klein Tank and Können*, 2003] state a negative trend of Mediterranean precipitation since the maximum in the 1960s, the insignificant lower precipitation extremes of the reference period (-1%), compared to the pre-industrial period, seem therefore explainable as well. But even if *Pauling et al.* [2006] state a decrease in mean precipitation since 1800, no similar reference is found for the remarkably high return levels in the summer pre-industrial period in Central Europe (+11.4% to the reference period).

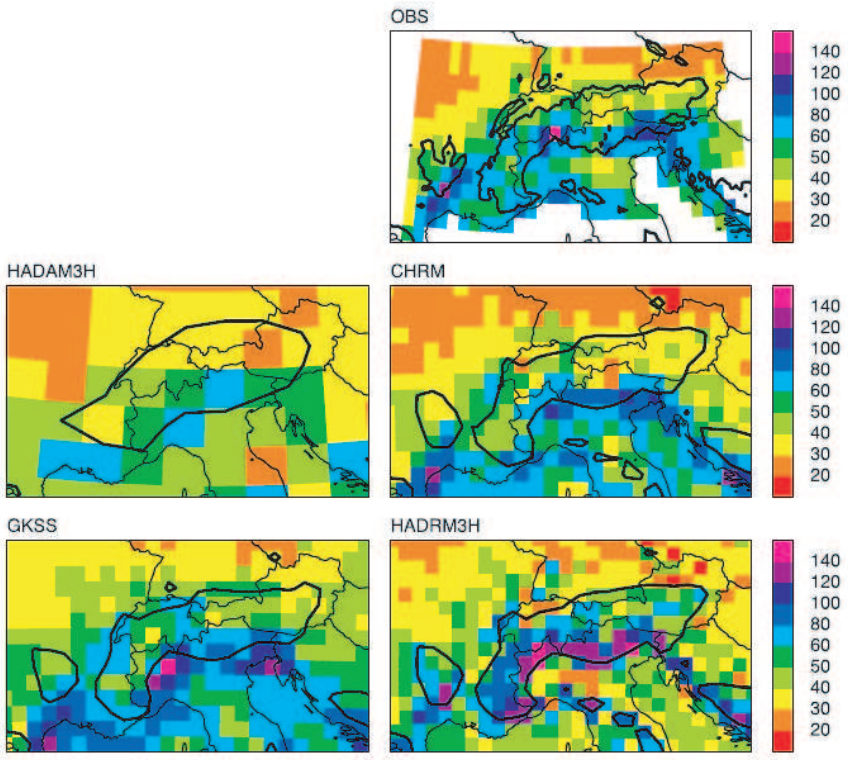

Figure 3.31: Comparison of precipitation return levels (in mm/day) for different climate models on a 5 year return period after *Frei et al.* [2006].

Among others, *Kharin and Zwiers* [2005], *Frei et al.* [2006] and *Nikulin et al.* [2011] estimated changes in extreme precipitation for future projections. Results of the CCSM3 model reveal an increase in precipitation extremes for the future (+5.6% in winter and +2.9% in summer). In comparison to the very general statement of *Kharin and Zwiers* [2005] that a warmer climate model becomes wetter, the results for the Mediterranean seem reasonable. *Frei et al.* [2006] state in contrast that the return levels in the Mediterranean experience small changes with a tendency toward decreases. For the Iberian Peninsula *Nikulin et al.* [2011] found a decrease in return levels by 10-40%, but no significant decreases (more than 10%) in other regions. The future projection of the CCSM3 model seems therefore to be wetter for the Mediterranean than in other simulations. Central and Northern Europe experience only significant changes in winter precipitation. The 50 year return level increases by 11% in Central Europe and by 21% in Northern Europe in winter. In summer, the changes are slightly negative but close to zero (-1.2% for Central Europe and -0.2% for Northern Europe). These findings are supported by the calculations of *Frei et al.* [2006] and *Nikulin et al.* [2011]. While *Frei et al.* [2006] state a general increase in return levels north of 45°N, *Nikulin et al.* [2011] showed an increase of 10-30% in winter extreme precipitation events for Scandinavia and other parts of Europe.

Drought reconstruction for the Mediterranean back to the Maunder Minimum are performed

by *Nicault et al.* [2008] analyzing tree-ring data. They observed three well marked drought periods, two of them within the Maunder Minimum: 1540-1574, 1620-1640 and 1645-1665. This is also evident on Figure 3.26. The 50 year return level of the SPI decreases (on every time scale) by the later 17th century. Most severe droughts ($SPI < -3$) are calculated, if moisture conditions of 12 years are taken into account. In the model a second period of extremely dry conditions is calculated shortly after 1800 and towards the end of the 20th century. The dry period around 1800 can also be found in the reconstruction of *Nicault et al.* [2008], but earlier. They observe a marked dry period, particularly after 1770. Further they identified the wettest year in 1810, but also the driest years in the Alps in the early 19th century. In the CCSM3 model results, the period of higher dry return levels (denoting a rather wet period) agrees well with *Nicault et al.* [2008]. During the end of the 20th century, *Nicault et al.* [2008] found a strong increase in dry periods in Eastern Mediterranean. In the model, the 50 year return level falls beyond the severe drought limit of -3 by the later 20th century.

In future projections the 50 year return levels of droughts in the Mediterranean decrease. More severe droughts are calculated with the SRES A2 climate projection, which is also found by *Burke et al.* [2006]. The 50 year return levels for Central and Northern Europe tend to rise to $-1 < SPI < 1$, meaning that no significant droughts can be found in that particular period. If these findings are compared to the calculations of *Burke et al.* [2006], especially the results of a wetter future in Northern Europe can be supported. Additionally, the lower severity in Central European droughts are reflected by *Burke et al.* [2006].

Chapter 4

Summary and Conclusions

In this thesis surface temperature and precipitation in the Community Climate System Model Version 3 (CCSM3) are analyzed with respect to extreme values. The approach of Generalized Extreme Value distribution (GEV), summarized by *Coles* [2001], is used to detect extreme values in ensemble simulations from 1500AD to 2100AD. The focus lies on the analysis of the Maunder Minimum (1661-1690AD), a pre-industrial period (1851-1880AD), a reference period (1961-1990AD) and a future period (2071-2100AD). Furthermore, grid points in the Mediterranean, Central and Northern Europe are chosen for the GEV analysis. In a first step, extreme values in temperature and precipitation in the different periods of time were estimated. In a second step, temperature and precipitation extreme values on longer time scales, such as cold/warm spells and droughts, are examined. In a last short section, the underlying dynamics of the severe cold/warm spells and droughts are discussed.

The Generalized Extreme Value analysis bases on block maxima. In this case, monthly maxima are analyzed. As the most powerful tool of the GEV analysis, return values of extreme temperature and precipitation, as well as of cold/warm spells and droughts, are calculated. Changes in the periods of time are estimated in comparison to the reference period (1961-1990), where the result of the reference period is subtracted from the particular period of time (either Maunder Minimum, pre-industrial period or future).

Cold and warm spells are defined as a spell of at least six consecutive days where the maximum temperature exceeds the local 10^{th} percentile of the control period 1961-1990 and 90^{th} percentile, respectively. Cold and warm spells can be characterized by the number of occurrences per year and their maximum duration. The extreme value analysis of cold and warm spells is performed on the maximum duration of the spells.

The analysis of droughts is conducted on the Standardized Precipitation Index (SPI). The SPI is a probability index that gives a representation of extraordinary wetness or dryness [*Guttman*, 1999]. As the SPI is calculated only on the basis of precipitation, it is preferred to the more widely used Palmer Drought Severity Index (PDSI). Droughts are estimated on different time scales, depending on the number of months taken into account. Due to the long time series (1500-2100AD), only time scales reflecting medium- to long-term moisture conditions are considered, i.e. 12- to 72-months SPI.

As frequently found before [*Luterbacher et al.*, 2001; *Xoplaki et al.*, 2005], the Maunder Minimum is a period of cold temperatures and rather dry conditions. The analysis of temperature maxima in the CCSM3 model, reveals low return values during winter and summer in the Mediterranean and Central Europe. The 50 year return level during the winter in the Maunder Minimum is by 0.87°C (Mediterranean) and by 0.75°C (Central Europe) lower than the reference period. Similar values are calculated for summer extreme temperatures. The return level decreases in winter are even lower for Northern Europe (-4.53°C). Regarding cold and warm spells, this picture is supported. During the Maunder Minimum, the maximum duration of a cold spell on a return period of 50 year, is calculated to be 16.5 days in the Mediterranean, 21.4 days in Central Europe and 14.6 days in Northern Europe. Thus, for the considered periods of time, the Maunder Minimum shows the longest cold spells for the Mediterranean and Northern Europe. Warm spells calculated for the Maunder Minimum are shorter if compared to the reference period (1961-1990). Considering precipitation extreme values, the picture of a drier Maunder Minimum seems reasonable. The 50 year return values for the Mediterranean, Central and Northern Europe during the Maunder Minimum winter are below the return values of the reference period. This is also true for the summer of the Mediterranean and Northern Europe. Only the summer in Central Europe results in higher return values and can therefore be interpreted as a period with more precipitation extreme values.

The pre-industrial period shows higher temperature extreme values than the Maunder Minimum, but lower values than the reference period. In comparison to 1961-1990, the 50 year return values are lowered by 0.83°C for the Mediterranean, by 0.13°C for Central Europe and by 1.81°C for Northern Europe. Lower return values in the pre-industrial period are also calculated in summer, except for Central Europe, which exhibits slightly enhanced warm extreme temperatures. This is reflected in the maximum duration of cold and warm spells as well. While winter cold spell are longer during the pre-industrial period, summer warm spells occur on shorter time scales than during the reference period. The pre-industrial period is furthermore similarly dry as the Maunder Minimum. The changes in extreme precipitation values are small. In winter the precipitation extreme values are slightly lower compared to the Maunder Minimum, in summer they are little enhanced, though.

As it could be expected, temperature extreme values increase for the future in summer and winter. The ensemble mean of future warm extremes rises about 2-4°C. In the Mediterranean summer the rise is even stronger than 4°C. These results are well embedded to other findings [*Beniston and Diaz*, 2004; *Kharin and Zwiers*, 2005; *Nikulin et al.*, 2011]. Cold spells decline close to zero towards 2100 and warm spells exhibit a strong increase in duration. Besides the upward trend of temperature extreme values, precipitation extreme values are calculated to rise as well. Compared to the reference period, the 50 year return values are larger for the future in winter for the grid points in the Mediterranean, Central Europe and Northern Europe. Likewise, precipitation extreme values in summer rise for the Mediterranean and Central Europe, though decline for Northern Europe. Still, the Mediterranean values of extreme precipitation rise, droughts intensify.

To detect distributional changes in extreme values, GEV parameters are calculated. The results reveal not only changes in location, but also in scale. This means that a change in mean climate does not only result in higher extreme values, but also in frequency. For tem-

perature, increases in scale are calculated in particular for Central and Northern European summer. Variability decreases can be detected in winter. The results found in the present thesis are well embedded into earlier findings [*Schär et al.*, 2004; *Fischer and Schär*, 2009; *IPCC SREX*, 2011 and others]. The distribution of the precipitation extreme values, shows an enhanced scale in the future for winter and summer in the Mediterranean, Central and Northern Europe. The scale enhancement is larger for winter extreme precipitation than for summer extreme precipitation.

Cold and warm spells, as well as droughts are induced by dominant high pressure. Depending on the region of the spell occurrence, the location of the high pressure differs. In general, air is advected from continental Europe to either the Mediterranean, Central or Northern Europe. An air flow from the Atlantic ocean to continental Europe during a cold/warm spell or drought can not be found.

Chapter 5

Outlook

Within the climate system, not only changes in temperature or precipitation extreme values play an important role. Wind extreme values can have severe impacts on the human life as well. However, projected future changes among differing climate models differ strongly [*Nikulin et al.*, 2011]. While *Bengtsson et al.* [2006] and *Bengtsson et al.* [2009] clearly claim that there is no indication for more intense storms in future climate, *Sienz et al.* [2010] suggested an extreme cyclone intensification in a warmer future climate. Furthermore, there is not much work done on the analysis of simulated past wind extremes. An extent of the extreme value analysis to wind would therefore not only be interesting, it could also reveal important insights.

In the framework of the present thesis, the focus lies on the statistical analysis of extreme values. The underlying dynamics are not covered comprehensively. In a further study, it would be interesting to investigate into the changes of the dynamical pattern leading to extreme values. A similar study has alreadybeen performed by *Buehler et al.* [2011] who examined blocking situations, that lead to dry or cold spells. However, an even deeper insight could be gained by the examination of distinct extreme values and their dynamical patterns.

Regarding extreme precipitation, only droughts in Europe are examined. Though, changes in wetness in past and future simulations could lead to a further understanding of the past climate dynamics. In particular, this would be important over regions experiencing larger wet extremes in the future, such as Central or Northern Europe.

It is probable, that the analysis of extreme values over the entire time series (1500-2100AD) would lead to a more detailed insight of the extreme value behavior in the past and the future. The approach of a moving window could be chosen. A similar attempt was made for the SPI time series. By choosing a lower time step as it was selected for the SPI, the approach could be expanded to other variables and indicies.

List of Tables

List of Figures

References

Alexander, L. V., X. Zhang, T. C. Peterson, B. Caesar, J.and Gleason, A. M. G. Klein Tank, M. Haylock, D. Collins, T. B., F. Rahimyadeh, A. Tagipur, K. Rupa Kumar, J. Revadekar, G. Griffiths, L. Vincent, D. B. Stephenson, J. Burn, E. Aguilar, M. Brunet, M. Taylor, M. New, P. Zhai, M. Rusticucci, and J. L. Vazquez-Aquirre, Global observed changes i daily climate extremes of temperature and precipitation, *Journal of Geophysical Research, 111*, 1–22, 2006.

Ammann, C. M., G. A. Meehl, W. M. Washington, and C. S. Zender, A monthly and latitudinally varying volcanic forcing dataset in simulations of 20th century climate, *Geophysical Research Letters, 30*(12), 1657–, 2003, June.

Beer, J., S. Tobias, and N. Weiss, An active sun throughout the maunder minimum, *Solar Physics, 181*, 237–249, 1998.

Bengtsson, L., K. I. Hodges, and N. Keenlyside, Will extratropical storms Intensify in a warmer climate?, *Journal of Climate, 22*(9), 2276–2301, 2009, May.

Bengtsson, L., K. I. Hodges, and E. Roeckner, Storm tracks and climate change, *Journal of Climate, 19*(15), 3518–3543, 2006, August.

Bengtsson, L., V. A. Semenov, and O. M. Johannessen, The early twentieth-century warming in the Arctic - a possible mechanism, *Journal of Climate, 17*, 4045–4057, 2004.

Beniston, M., and H. F. Diaz, The 2003 heat wave as an example of summers in a greenhouse climate? Observations and climate model simulations for Basel, Switzerland, *Global and Planetary Change, 44*(1-4), 73–81, 2004, December.

Blunier, T., J. Chappellaz, J. Schwander, B. Stauffer, and D. Raynaud, Variations in atmospheric methane concentration during the Holocene epoch, *Nature, 374*, 46–49, 1995.

Briegleb, B. P., C. M. Bitz, E. C. Hunke, W. H. Lipscomb, M. M. Holland, J. L. Schramm, and R. E. Moritz, Scientific description of the sea ice component in the Community Climate System Model, version 3, *NCAR Tech. Note, NCAR/TN-463+STR, Tech. Rep.*, 2004.

Brunet, M., S. O., P. Jones, J. Sigró, E. Aguilar, A. Moberg, D. Lister, A. Walther, D. Lopez, and C. Almarza, The development of a new dataset of spanish daily adjusted temperature series (SDATS) (1850-2003), *International Journal of Climatology, 26*, 1777–1802, 2006.

Brunkard, J., G. Namulanda, and R. Ratard, Hurricane Katrina deaths, Louisiana, 2005, *American Medical Association,*, 2008.

Buehler, T., C. Raible, and T. F. Stocker, The relationship of winter season North Atlantic blocking frequencies to extreme cold or dry spells in the ERA-40, *Tellus, 63A*, 212–222, 2011.

Burke, E. J., S. J. Brown, and N. Christidis, Modeling the recent evolution of global drought and projections for the twenty-first century with the Hadley Centre Climate Model, *Journal of Hydrometeorology, 7*, 1113–1125, 2006.

Burton, M. L., and M. J. Hicks, Hurricane Katrina: preliminary estimates of commercial and public sector damages, *Center for Business and Economic Research, Marshall University, Tech. Rep.*, September 2005.

Caesar, J., and A. Lisa, Large-scale changes in observed daily maximum and minimum temperatures: Creation and analysis of a new gridded data set, *Journal of Geophysical Research, 111*, 1–10, 2006.

Coles, S., *An introducion to statistical modeling of extreme values*, Springer, 2001.

Collins, W. D., C. M. Bitz, M. L. Blackmon, G. B. Bonan, C. S. Bretherton, J. A. Carton, P. Chang, S. C. Doney, J. J. Hack, T. B. Henderson, J. T. Kiehl, W. G. Large, D. S. McKenna, B. D. Santer, and R. D. Smith, The Community Climate System Model version 3 (CCSM3), *Journal of Climate, 19*(11), 2122–2143, 2006, June.

Collins, W. D., P. J. Rasch, B. A. Boville, J. J. Hack, J. R. McCaa, D. L. Williamson, B. P. Briegleb, C. M. Bitz, S. J. Lin, and M. H. Zhang, The formulation and atmospheric simulation of the Community Atmosphere Model version 3 (CAM3), *Journal of Climate, 19*(11), 2144–2161, 2006, June.

Corell, R. W., Challenges of climate change: An Arctic perspective, *Royal Swedish Academy of Sciences, 35*, 148–152, 2006.

Crowley, T. J., Are there any satisfactory geologic analogs for a future greenhouse warming?, *Journal of Climate, 3*, 1282–1292, 1990.

Crowley, T. J., Causes of climate change over the past 1000 years, *Science, 289*(5477), 270–277, 2000, July.

Del Sole, T., M. K. Tippett, and J. Shukla, A significant component of unforced multidecadal variability in the recent acceleration of global warming, *Journal of Climate, 24*, 909–926, 2010.

Díaz, J., R. García-Herrera, L. C., C. Linares, A. Tobías, and L. Prieto, Mortality impact of extreme winter temperatures, *International Journal of Biometeorology, 49*, 179–183, 2005.

Easterling, D. R., J. L. Evans, P. Y. Groisman, T. R. Karl, K. E. Kunkel, and A. P., Observed variability and trends in extreme climate events: A brief review, *Bulletin of the American Meteorological Society, 81*, 417–425, 2000.

Easterling, D. R., G. A. Meehl, C. Parmesan, S. A. Changnon, T. R. Karl, and L. O. Mearns, Climate extremes: Observations, modeling, and impacts, *Science, 289*(5487), 2068–2074, 2000.

Eddy, J. A., The Maunder Minimum, *Science, 192*, 1189–1202, 1976.

Edwards, D. C., T. B. McKee, N. J. Doesken, and Kleist, Historical analysis of drought in the united states, in *Seventh Conference on Climate Variations*, 1997.

Etheridge, D. M., L. P. Steele, R. L. Langenfelds, R. J. Francey, J.-M. Barnola, and V. I. Morgan, Natural and anthropogenic changes in atmospheric CO2 over the last 1000 years from air in Antarctic ice and firn, *Journal of Geophysical Research, 101*(D2), 4115–4128, 1996.

Fischer, E. M., and C. Schär, Future changes in daily summer temperature variability: Driving processes and role for temperature extremes, *Climate Dynamics, 33*(7-8), 917–935, 2009.

Fischer, E. M., and C. Schär, Consistent geographical patterns of changes in high-impact European heatwaves, *Nature Geoscience, 3*(6), 398–403, 2010.

Flückiger, J., A. Dallenbach, T. Blunier, B. Stauffer, T. F. Stocker, D. Raynaud, and J. M. Barnola, Variations in atmospheric N2O concentration during abrupt climatic changes, *Science, 285*(5425), 227–230, 1999, July.

Flückiger, J., E. Monnin, B. Stauffer, J. Schwander, T. F. Stocker, J. Chappellaz, D. Raynaud, and J. M. Barnola, High-resolution Holocene N2O ice core record and its relationship with CH4 and CO2, *Global Biogeochemical Cycles, 16*(1), 1010, 2002, March.

Frei, C., R. Scholl, S. Fukutome, and S. J., Future change of precipitation extremes in Europe: intercomparison of scenarios from regional climate models, *Journal of Geophysical Research, Vol. 111*, 1–22, 2006.

Frich, P., L. V. Alexander, P. Della-Marta, B. Gleason, M. Haylock, A. M. G. Klein Tank, and T. Peterson, Observed coherent changes in climatic extremes during the second half of the twentieth century, *Climate Research, 19*, 193–212, 2002.

García-Herrera, R., J. Díaz, R. M. Trigo, J. Luterbacher, and E. M. Fischer, A review of the european summer heat wave of 2003, *Critical Reviews in Environmental Science and Technology, 40*(4), 267–306, 2010, March.

García-Herrera, R., D. Paredes, R. M. Trigo, I. F. Trigo, E. Hernández, D. Barriopedro, and M. A. Mendes, The outstanding 2005/05 drought in the Iberian Peninsula: Associated atmospheric circulation, *Journal of Hydrometeorology, 8*, 483–298, 2007.

Giddings, L., M. Soto, B. M. Rutherford, and M. A., Standardized Precipitation Index zones for Mexico, *Atmosfera,*, 33–56, 2005.

Giorgi, F., and X. Bi, Regional changes in surface climate interannual variability for the 21st century from ensembles of global model simulations, *Geophysical Research Letters, 32*, 1–5, 2005.

Groisman, P. Y., R. W. Knight, D. R. Easterling, T. R. Karl, G. C. Hegerl, and V. N. Razuvaev, Trends in intense precipitation in the climate record, *Journal of Climate, 18*(9), 1326–1350, 2005, May.

Gunnarson, B. E., and H. W. Linderholm, Low-frequency summer temperature variation in central Sweden since the tenth century inferred from tree rings, *The Holocene, 12*, 667–671, 2002.

Guttman, N. B., Comparing the Palmer Drought Index and the Standardized Precipitation Index, *Journal of the American Water Resources Association, 34*, 113–121, 1998.

Guttman, N. B., Accepting the Standardized Precipitation Index: a calculation algorithm, *Journal of the American Water Resources Association, 35*, 311–322, 1999.

Häkkinen, S., P. B. Rhines, and W. D. L., Atmospheric blocking and atlantic multidecadal ocean variability, *Science, 334*, 655–659, 2011.

Hay, W. W., R. M. DeConto, and W. C. N., Climate: Is the past the key to the future?, *International Journal of Earth Sciences, 86*, 471–491, 1997.

Hegerl, G. C., T. J. Crowley, R. P. Allan, W. T. Hyde, H. N. Pollack, H. Smerdon, and E. Zorita, Detection of human influence on a new, validated 1500 year temperature reconstruction, *Journal of Climate, 20*, 650–666, 2007.

Hofer, D., C. Raible, and T. Stocker, Variations of the Atlantic meridional overturning circulation in control and transient simulations of the last millennium, *Climate of the Past Discussions, 6*, 1267–1309, 2011.

Holland, M. M., and C. M. Bitz, Polar amplification of climate change in coupled models, *Climate Dynamics, 21*, 221–232, 2003.

Huynen, M. M., P. Martens, D. Schram, M. P. Weijenberg, and A. E. Kunst, The Impact of Heat Waves and Cold Spells on Mortality Rates in the Dutch Population, *Environmental Health Perspective, 109*, 463–470, 2001.

IPCC, Climate Change 2001: The Scientific Basis. Contribution of Working Group I to the Third Assessment Report of the Intergovernmental Panel on Climate Change, *[Houghton, J.T., Y. Ding, D.J. Griggs, M. Noguer, P.J. van der Linden, X. Dai, K. Maskell, and C.A. Johnson (eds.)]. Cambridge University Press, Cambridge, United Kingdom and New York, NY, USA, 881pp.*, *Tech. Rep.*, 2001.

IPCC, Climate Change 2007: The Physical Science Basis. Contribution of Working Group I to the Fourth Assessment Report of the Intergovernmental Panel on Climate Change, *[Solomon, S., D. Qin, M. Manning, Z. Chen, M. Marquis, K.B. Averyt, M. Tignor and H.L. Miller (eds.)]. Cambridge University Press, Cambridge, United Kingdom and New York, NY, USA, 996pp.*, *Tech. Rep.*, 2007.

IPCC SRES, Special Report on Emission Scenarios, *A Special Report of IPCC Working Group III. Cambridge University Press, Cambridge, United Kingdom and New York, NY, USA.*, *Tech. Rep.*, 2000.

IPCC SREX, Special Report on Managing the Risks of Extreme Events and Disasters to Advance Climate Change Adaptation, *IPCC 2011: Summary for Policymakers [Field, C. B., Barros, V., Stocker, T.F., Qin, D., Dokken, D., Ebi, K.L., Mastrandrea, M. D., Mach, K. J., Plattner, G.-K., Allen, S., Tignor, M. and P. M. Midgley (eds.)]. Cambridge University Press, Cambridge, United Kingdom and New York, NY, USA*, *Tech. Rep.*, 2011.

James, T., Extreme value theory. Course manual for MATH 453, *Lancaster University, United Kingdom, Tech. Rep.*, 2011.

Jones, P. D., and M. E. Mann, Climate over past millennia, *Reviews of Geophysics, 42*, 1–42, 2004.

Jones, P. D., and A. Moberg, Hemispheric and large-scale surface air temperature variations: An extensive revision and an update to 2001, *Journal of Climate, 16*(2), 206–223, 2003, January.

Katz, R. W., Statistics of extremes in climate change, *Climatic Change, 100*, 71–76, 2010.

Kharin, V. V., and F. W. Zwiers, Estimating extremes in transient climate change simulations, *Journal of Climate, 18*(8), 1156–1173, 2005.

Kiehl, J. T., C. A. Shields, J. J. Hack, and W. D. Collins, The climate sensitivity of the Community Climate System Model version 3 (CCSM3), *Journal of Climate, 19*(11), 2584–2596, 2006.

Klein Tank, A. M. G., and G. P. Können, Trends in indices of daily temperature and precipitation extremes in Europe, 1946-99, *American Meteorological Society, 16*, 3665–3680, 2003.

Le Quere, C., M. R. Raupach, J. G. Canadell, and G. Marland et al., Trends in the sources and sinks of carbon dioxide, *Nature Geoscience, 2*(12), 831–836, 2009, December.

Lean, J., J. Beer, and R. Bradley, Reconstruction of solar irradiance since 1610 - implications for climate-change, *Geophysical Research Letters, 22*(23), 3195–3198, 1995, December.

Luterbacher, J., D. Dietrich, E. Xoplaki, M. Grosjean, and H. Wanner, European seasonal and annual temperature variability, trends, and extremes since 1500, *Science, 303*, 1499–1503, 2004.

Luterbacher, J., R. Rickli, E. Xoplaki, C. Tinguely, C. Beck, C. Pfister, and H. Wanner, The late Maunder Minimum (1675-1715) - A key period for studying decadal scale climatic change in Europe, *Climatic Change, 49*, 441–462, 2001.

Lüthi, D., M. Le Floch, B. Bereiter, T. Blunier, J.-M. Barnola, U. Siegenthaler, D. Raynaud, J. Jouzel, H. Fischer, K. Kawamura, and T. F. Stocker, High-resolution carbon dioxide concentration record 650,000-800,000 years before present, *Nature, 453*(7193), 379–382, 2008, May.

McKee, T., J. D. Nolan, and J. Kleist, The relationship of drought frequency and duration to time scales, *Eighth Conference on Applied Climatology,*, 1993.

McKee, T. B., N. J. Doesken, and J. Kleist, Drought monitoring with multiple time scales, *Climatology,*, 233–236, 1995.

Meehl, G. A., and C. Tebaldi, More intense, more frequent, and longer lasting heat waves in the 21st century, *Science, 305*(5686), 994–997, 2004, August.

Nicault, A., S. Alleaume, S. Brewer, M. Carrer, P. Nola, and J. Guiot, Mediterranean drought fluctuation during the last 500 years based on tree-ring data, *Climate Dynamics, 31*(2-3), 227–245, 2008, August.

Nikulin, G., E. Kjellström, U. Hansson, G. Strandberg, and A. Ullerstig, Evaluation and future projections of temperature, precipitation and wind extremes over Europe in an ensemble of regional climate simulations, *Tellus A, 63*(1), 41–55, 2011.

Pauling, A., J. Luterbacher, C. Casty, and H. Wanner, Five hundred years of gridded high-resolution precipitation reconstructions over Europe and the connection to large-scale circulation, *Climate Dynamics, 26*(4), 387–405, 2006.

Pauling, A., and H. Paeth, On the variability of return periods of European winter precipitation extremes over the last three centuries, *Climate of the Past, 3*, 65–76, 2007.

Pelly, J. L., and B. J. Hoskins, A new perspective on blocking, *Journal of the Atmospheric Sciences, 60*, 743–755, 2003.

Peterson, T. C., Climate change indices, *World Meteorological Organization Bulletin, 54, No. 2*, 83–86, April 2005.

Raible, C. C., C. Casty, J. Luterbacher, A. Pauling, J. Esper, D. C. Frank, U. Büntgen, A. C. Roesch, P. Tschuck, M. Wild, P. L. Vidale, C. Schär, and H. Wanner, Climate variability - observations, reconstructions, and model simulations for the Atlantic-European and Alpine region from 1500-2100 AD, *Climatic Change, 79*, 9–29, 2006.

Räisänen, J., CO2-induced climate change in CMIP2 experiments: Quantification of agreement and role of internal variability, *Journal of Climate, 14*, 2088–2104, 2000.

Rex, D. F., Blocking action in the middle troposphere and its effect upon regional climate, *Tellus, 2*, 275–301, 1950.

Rimbu, N., and G. Lohmann, Winter and summer blocking variability in the North Atlantic region - evidence from long-term observational and proxy data from southwestern Greenland, *Climate Past Discussion, 5*, 2411–2437, 2009.

Sausen, R., W. König, and F. Sielmann, Analysis of blocking events from observations and ECHAM model simulations, *Tellus, 47A*, 41–438, 1995.

Schär, C., P. L. Vidale, D. Lüthi, C. Frei, C. Häberli, M. A. Liniger, and C. Appenzeller, The role of increasing temperature variability in European summer heatwaves, *Nature, 427*(6972), 332–336, 2004, January.

Scherrer, S. C., C. Appenzeller, M. A. Liniger, and C. Schär, European temperature distribution changes in observations and climate change scenarios, *Geophysical Research Letters, 32*(19), 2005, October.

Sienz, F., A. Schneidereit, R. Blender, K. Fraedrich, and F. Lunkeit, Extreme value statistics for North Atlantic cyclones, *Tellus Series A-Dynamic Meteorology And Oceanography, 62*(4), 347–360, 2010.

Sillmann, J., and M. Croci-Maspoli, Present and future atmospheric blocking and its impact on European mean and extreme climate, *Geophysical Research Letters, 36*, 1–6, 2009.

Smith, R. S., and P. R. Gent, Reference manual for the Parallel Ocean Program (POP), ocean component of the Community Climate System Model (CCSM2.0 and 3.0), *Los Alamos National Labratory Tech. Rep. LA-UR-02-2484, Tech. Rep.*, 2004.

Stouffer, R. J., M. S., and V. K. Ya., Model assessment of the role of natural variability in recent global warming, *Nature, 367*, 634–636, 1994.

Tan, J., Y. Zheng, G. Song, L. Kalkstein, K. A., and T. X., Heat wave impacts on mortality in Shanghai, 1998 and 2003, *International Journal of Biometeorology, 51*, 193–200, 2007.

Uppala, S. M., P. W. Kallberg, U. Andrae, V. D. C. Bechtold, M. Fiorino, A. Hernandez, X. Li, K. Onogi, S. Saarinen, and N. Sokka, ERA-40: ECMWF 45-year reanalysis of the global atmosphere and surface conditions 1957-2002, *ECMWF Newsletter, 101*, Summer/Autumn 2004.

Uppala, S. M., P. W. Kllberg, A. J. Simmons, U. Andrae, V. D. C. Bechtold, M. Fiorino, J. K. Gibson, J. Haseler, A. Hernandez, G. A. Kelly, X. Li, K. Onogi, S. Saarinen, N. Sokka, R. P. Allan, E. Andersson, K. Arpe, M. A. Balmaseda, A. C. M. Beljaars, L. V. D. Berg, J. Bidlot, N. Bormann, S. Caires, F. Chevallier, A. Dethof, M. Dragosavac, M. Fisher, M. Fuentes, S. Hagemann, E. Hlm, B. J. Hoskins, L. Isaksen, P. A. E. M. Janssen, R. Jenne, A. P. Mcnally, J.-F. Mahfouf, J.-J. Morcrette, N. A. Rayner, R. W. Saunders, P. Simon, A. Sterl, K. E. Trenberth, A. Untch, D. Vasiljevic, P. Viterbo, and J. Woollen, The ERA-40 re-analysis, *Quarterly Journal of the Meteorological Society, 131*(612), 2961–3012, 2005.

Vaughan, D. G., G. J. Marshall, W. M. Connolley, C. Parkinson, M. R., D. A. Hodgson, J. C. King, C. J. Pudsey, and T. J., Recent rapid regional climate warming on the Antarctic Peninsula, *Climate Change, 60*, 243–274, 2003.

Wanner, H., C. Pfister, R. Brázdil, P. Frich, K. Frydendahl, T. Jónsson, J. Kington, H. H. Lamb, s. Rosenorn, and E. Wishman, Wintertime European circulation patterns during the Late Maunder Minimum cooling period (1675-1704), *Theoretical and Applied Climatology, 51*, 167–175, 1995.

Xoplaki, E., J. F. Gonzalez-Rouco, J. Luterbacher, and H. Wanner, Wet season Mediterranean precipitation variability: influence of large-scale dynamics and trends, *Climate Dynamics, 23*, 63–78, 2004.

Xoplaki, E., J. Luterbacher, H. Paeth, D. Dietrich, N. Steiner, M. Grosjean, and H. Wanner, European spring and autumn temperature variability and change of extremes over the last half millennium, *Geophysical Research Letters, 32*, 1–4, 2005.

Yiou, P., and M. Nogaj, Extreme climatic events and weather regimes over the North Atlantic: When and where?, *Geophysical Research Letters, 31*, 1–4, 2004.

Yoshimori, M., C. C. Raible, T. F. Stocker, and M. Renold, Simulated decadal oscillations of the Atlantic meridional overturning circulation in a cold climate state, *Climate Dynamics, 34*(1), 101–121, 2010.

Zorita, E., T. F. Stocker, and von Storch H., How unusual is the recent series of warm years?, *Geophysical Research Letters, 35*, 1–6, 2008.

Acknowledgements

I want to thank my supervisors PD Dr. Christoph Raible and Prof. Dr. Thomas Stocker. For supporting me, giving me a lot of freedom and at the same time putting me under pressure whenever it was necessary.

My office collegues Flavio, Nick, Sophie and Tom I'm thankful for answering thousands of silly questions, laughing with and about me. There were many (incredibly) bad jokes, which kept the seriousness (sometimes) far, far away.

A special thanks to Kay Bieri for solving all my computer related problems without rolling eyes.

Sandra, you are and were the best flatmate ever. Spending many nights togheter, bringing George to his limits and shearing this moment with you. You're great!

Another girl deserves to be mentioned: Sophie, thank you for any assists here in the KUP office and spending uncountable hours in the vertical with me. I could learn a lot and had always fun. Once I will bring you back where you belong - Switzerland!

Finally and most importantly, I thank my family. With the finish of my education, an era takes its end. Thank you for supporting me my whole life in every concern. You were always there for me, had an open door and a helping hand.